PERFORMANCE OF NICKEL-COPPER/ALUMINA CATALYTIC SYSTEMS IN DRY REFORMING OF METHANE: IMPACT OF COPPER LOADING AND SYNTHESIS TECHNIQUE

A Thesis

by

OMAR EL HASSAN

Submitted to the Graduate and Professional School of
Texas A&M University
in partial fulfillment of the requirements for the degree of

MASTER OF SCIENCE

Chair of Committee, Nimir Elbashir
Committee Member, Konstantinos Kakosimos
Committee Member, Ibrahim Galal Hassan
Head of Department, Patrick Linke

August 2021

Major Subject: Chemical Engineering

ABSTRACT

Dry reforming of methane (DRM) is a promising process that can convert carbon dioxide and methane, two of the most abundant greenhouse gases, into synthesis gas or syngas (a mixture of hydrogen and carbon monoxide). This vital chemical precursor can then be transformed into several value-added products, including ultra-clean fuels. One of the main obstacles facing DRM is the rapid deactivation of economically desirable nickel-based catalysts due to carbon formation. Several studies have investigated the different combinations of supports and promotors, which could improve the performance of nickel catalysts. However, a limited number of studies have investigated the impact of varying preparation techniques on synthesized bimetallic catalysts. The current work aimed at studying the Ni-Cu/Al_2O_3 catalytic system in DRM, focusing on exploring the effect of copper loading on the catalyst characteristics and performance and the impact of the catalyst synthesis technique. Three main preparation techniques were investigated, incipient wetness impregnation (IWI), co-precipitation (CP), and the sol-gel (SG) method. A comprehensive set of characterization techniques (ICP, BET, H_2-TPR, Chemisorption, XRD, XPS, SEM, TEM, EDS, TGA, TPO, DSC) was used to investigate crucial catalyst characteristics such as species reducibility, particle size distribution, crystallite diffraction patterns, and elemental composition. The study is divided into two sections. In the first section, titled optimization of copper loading, catalysts were synthesized by IWI only. It was found that medium copper loading (Ni: Cu=8:1) significantly improved catalyst performance compared to the monometallic variant and bimetallic catalysts with high and low copper loading. The formation of a Ni-Cu alloy reduced the amount of coke formed and increased catalyst stability. High copper loading (Ni:Cu=3:1) had an opposite effect as it reduced catalyst activity. In the second section of the study, monometallic and bimetallic catalysts (Ni:Cu=8:1) were synthesized using the SG and CP techniques. In the second

section, titled impact of synthesis technique, it was found that bimetallic catalysts prepared by SG and CP were outperformed by their monometallic counterparts when tested for DRM. EDS analysis revealed that although the amount of copper introduced into the system aimed at creating a ‘medium’ loading, the synthesized catalyst had localized ‘high’ loading of copper encapsulating the active nickel sites in a core-shell shape. TGA of spent CP catalysts showed that the monometallic CP catalyst had a higher amount of carbon formed, indicating that the only logical reason for the underperformance of the bimetallic catalysts was copper segregation on the catalyst surface.

ACKNOWLEDGEMENTS

First and foremost, I would like to thank my committee chair Dr.Nimir Elbashir for his fantastic support and guidance throughout every stage of this work. Your insightful feedback pushed me to sharpen my thinking and brought my work to a higher level. It has been an absolute pleasure being a member of your research team.

I would also like to thank Dr. Chatla and Mr.Anuj for their help in completing this work. Your guidance on every detail of the project, be it general or specific, was vital in completing this work.

In addition, I thank my manager at the QEERI Core Labs, Dr. Said Mansour, for allowing me to complete my degree while maintaining a full-time position. I also thank Dr.Said for allowing me to use the core lab facilities to conduct a lot of the work used in this thesis. On that note, I want to thank all the core lab staff who have helped and guided me throughout this work.

Finally, I want to thank my family and friends for their support and motivation during this journey.

CONTRIBUTORS AND FUNDING

Contributors

This work has been supervised by a committee chaired by Dr.Nimir Elbashir. Members Dr.Konstantinos Kakosimos and Dr.Ibrahim Galal Hassan. Section I of the results is part of a publication in Applied Catalysis A [1]. The type-up of this section was a joint effort by Dr. Anjaneyulu Chatla and Omar El Hassan.

Reactor testing, BET, Chemisorption, and H_2-TPR data were acquired with the help of Dr. Anjaneyulu Chatla in TAMUQ. Dr. Chatla provided the necessary training to operate the equipment and conduct the required tests. The data relating to these techniques in Section I of the results were obtained with his help and supervision. In Section 2 of the results, the data for these techniques were obtained independently by Omar El Hassan. However, his supervision was monumental to maintain the quality of the work. TPO data in Section I of the results were provided by Dr. Chatla.

SEM images included in the results section were obtained with the help of Mr. Mujaheed Pasha of the QEERI Core Labs, who operated the equipment. Analysis of the data was conducted independently by Omar El Hassan.TEM-EDS images included in the results section were obtained with the help of Mr. Janarthanan Ponraj of the QEERI Core Labs, who operated the equipment. Analysis of the data was conducted independently. XRD data included in Section II of the results were obtained with the help of Dr. Akshath Raghu Shetty of the QEERI Core Labs, who assisted in operating the equipment. Analysis of the data was conducted independently by Omar El Hassan.

XPS data included in Section II of the results were obtained with the help of Dr. Yongfeng Tong of the QEERI Core Labs. Dr. Tong also aided in performing the deconvolution of the XPS Spectra. Analysis of the data was conducted independently by Omar El Hassan.TGA-DSC data

were obtained by Omar El Hassan in the QEERI Core Labs facilities. All catalyst samples were synthesized by Omar El Hassan under the supervision of Dr. Anjaneyulu Chatla. All remaining work in this thesis has been conducted by Omar El Hassan.

Funding

This work is a part of the research activities of the NPRP award [NPRP-EP-X-100-2-024] from the Qatar National Research Fund (a member of The Qatar Foundation). The statements made herein are solely the responsibility of the authors.

TABLE OF CONTENTS

LIST OF FIGURES

LIST OF TABLES

1. INTRODUCTION

Dry reforming of methane (DRM) has established itself as one of the most challenging chemical industry puzzles. On the one hand, it has an enormous potential to convert two of the most abundant greenhouse gases, carbon dioxide and methane, into valuable chemical products via conversion to synthesis gas (a mixture of hydrogen and carbon monoxide). On the other, it is undeniable that commercializing this process by itself is not currently feasible [2]. The thermodynamics of DRM dictates that a significant amount of energy is required to operate the reaction at elevated temperatures and attain the desired conversion. Running the reaction at low temperatures renders the used catalyst susceptible to deactivation via carbon deposition resulting from side reactions [3].

The clear majority of research in this field has revolved around studying different catalytic systems that exhibit the desired performance at a reasonable price. Non-noble metal systems are at the forefront of these studies. They provide a comparable alternative to noble metal systems, which are too expensive to purchase at the scale required for commercialization [4].

The most popular non-noble metal systems utilize Nickel (Ni) as an active phase. A quick literature search on DRM yields hundreds of articles presenting the performance of different combinations of supports and promoters in the nickel system [5–7]. While these studies provide valuable insights on several nickel systems, very few foci on the impact of preparation technique on the obtained catalyst. Specifically, there is an evident deficiency in the number of studies investigating bimetallic nickel-copper systems with different preparation techniques.

Considering the challenges mentioned above facing the DRM technology, the current study investigates a nickel-based bimetallic catalytic system, Ni-Cu/Al_2O_3 system, to identify the role of the catalyst synthesis on its performance and stability. The study had two main objectives; the first is to identify the influence of the copper loading on the catalysts' structure and performance. The second is to investigate the impact of the synthesis technique on the same.

The first section of this study focuses on the role of copper loading on the bi-metallic catalyst performance in DRM based on a catalyst prepared by the IWI technique. The goal in this section was to optimize the copper loading. Nickel catalysts were doped with copper in three different loading ratios: low, medium, and high. Other synthesis techniques have been tested in the second section, including the sol-gel and the co-precipitation techniques. A comprehensive and detailed set of characterization techniques have been utilized to look at the catalyst surface structure before and after the reaction and evaluate the activity of the different catalysts for DRM.

2. LITERATURE REVIEW

2.1. Methane Reforming

According to the U.S. Energy Information Administration, as of January 1, 2019, there is an estimated 7,177 trillion cubic feet (TCF) of total world-proved reserves of gross natural gas [8]. This highly abundant resource is valuable in various applications, including heating, electrical generation, and the production of plastics and other commercially significant organic compounds. The largest natural gas component is methane comprising anywhere between 49-84% depending on the well [9].

Natural gas is converted into other chemicals via various routes. Indirectly, natural gas is used to produce essential chemicals by converting its principal component, methane, into synthesis gas (syngas). Different processes require the ratio of H_2/CO to be within a specific range. Methanol, ethanol production, and Fischer-Tropsch (FT) Synthesis are some of the most common processes requiring syngas. The FT process converts syngas into syncrude and condensates that can be refined to gasoline, naphtha, diesel, kerosene, as well as heavy hydrocarbon wax [9].

Several reforming methods are used to convert methane into syngas. The most notable commercial reformers are the steam reforming of methane (SRM), the partial oxidation of methane (POX), and the autothermal reforming of methane (ATR). Dry reforming of methane (DRM) is another potential reforming technique that utilizes CO_2 as a soft oxidant widely studied; however, not yet commercialized in large scales similar to the others.

2.1.1. Steam Reforming of Methane

SRM (Eq. 1) is by far the most industrially utilized process amongst the known reforming techniques. In 2008, the U.S. Environmental Protection Agency reported that approximately 95% of all hydrogen produced in the U.S. comes from SRM [10]. Fundamentally, this reaction involves reacting high-temperature steam with methane under the presence of a catalyst to produce syngas. SRM is accompanied by the Water Gas Shift (WGS) reaction (Eq. 2) and its reverse. This reaction is undesirable since it consumes CO lowering the selectivity towards this desired product. It is important to note that the side reactions which produce coke in DRM are also present in this reaction.

$$CH_4 + H_2O \leftrightarrow CO + 3H_2 \qquad \Delta H^0_{298K} = 206 \text{ kJ.mol}^{-1} \quad \textbf{(1)}$$

$$CO + H_2O \leftrightarrow CO_2 + H_2 \qquad \Delta H^0_{298K} = -41 \text{ kJ.mol}^{-1} \quad \textbf{(2)}$$

The reactor pressure used in this process is typically within the range of 3-25 bar [11]. In addition, this process requires an elevated steam ratio to carbon at extreme reactor temperature (800-1000 °C). These conditions are critical to oxidize the formed coke and protect the catalyst from deactivating [12].

Although noble metal catalytic systems have shown a remarkable performance in SRM, industrial-scale applications typically utilize nickel-based catalysts due to their lower cost.

2.1.2. Partial Oxidation of Methane

Although not as widespread as SRM, POX is a process that has caught the attention of several industries within the last several decades. This reaction involves feeding a non-stoichiometric amount of oxygen alongside methane into a reactor to produce syngas (Eq.3).

$$CH_4 + \frac{1}{2}O_2 \leftrightarrow CO + 2H_2 \qquad \Delta H^0_{298K} = -36\ kJ.mol^{-1} \qquad \textbf{(3)}$$

Besides the primary POX reaction, numerous side reactions can occur (Eq.4-6). Furthermore, since side reactions generate CO_2 and H_2O, DRM and SRM can occur.

$$CH_4 + 2O_2 \leftrightarrow CO_2 + 2H_2O \qquad \Delta H^0_{298K} = -802\ kJ.mol^{-1} \qquad \textbf{(4)}$$

$$CH_4 + H_2O \leftrightarrow CO + 3H_2 \qquad \Delta H^0_{298K} = 206\ kJ.mol^{-1} \qquad \textbf{(5)}$$

$$CH_4 + 2H_2O \leftrightarrow 2CO_2 + 4H_2 \qquad \Delta H^0_{298K} = 165\ kJ.mol^{-1} \qquad \textbf{(6)}$$

When compared to SRM, which is highly endothermic, POM is exothermic. As a result, the operational cost of heating a POX reactor is lower, thereby improving the process's economics. Furthermore, the exothermicity of POX enables the potential of combining it with other endothermic reforming processes. Moreover, POX holds a significant advantage when examining its H_2/CO ratio, approximately 2. This ratio is attractive for multiple industrial processes such as the Fischer-Tropsch [13].

On the other hand, POX does present some disadvantages; namely, it requires a pure oxygen supply. To fulfill this requirement, an air separation unit is needed, thereby significantly increasing the process cost. Furthermore, a pure oxygen supply presents a safety risk, consequently increasing the complexity of the process as several safety measures must be placed. An example of such a plant is Shell's Pearl GTL plant which has the world's largest O_2 generation capacity. In addition, this process is susceptible to Sulphur content in the feed. As a result, feed desulphurization is critical to avoid catalyst poisoning [14].

2.1.3. Dry Reforming of Methane

DRM (Eq.7) is by no means a new process. The first investigation dated back to 1888 [15] and was later studied by Frank Fischer and Hans Tropsch in 1928 [16]. The high interest in DRM lies in its capability to utilize two of the most abundant greenhouse gases, methane, and carbon dioxide, to produce an equimolar mixture of carbon dioxide and hydrogen, otherwise known as synthesis gas.

$$CH_4 + CO_2 \leftrightarrow 2CO + 2H_2 \qquad \Delta H^0_{298K} = 247 \text{ kJ.mol}^{-1} \qquad \textbf{(7)}$$

DRM is accompanied by several side reactions depending on the operating conditions. RWGS (Eq.2) occurs below 817 °C. The occurrence of this reaction leads to a higher CO_2 conversion compared to CH_4. The produced synthesis gas, as a result, is CO rich and has an H_2/CO ratio of one or below.

In addition to RWGS, DRM often suffers from side reactions that produce carbon. Methane cracking (Eq.8) occurs above 557 ° C, while the Boudouard reaction (Eq.9) occurs below 701°C.

$$CH_4 \leftrightarrow C + 2H_2 \qquad \Delta H^0_{298K} = 75 \text{ kJ.mol}^{-1} \qquad \textbf{(8)}$$

$$2CO \leftrightarrow C + CO_2 \qquad \Delta H^0_{298K} = -172 \text{ kJ.mol}^{-1} \qquad \textbf{(9)}$$

Operating the reaction above 817 °C limits carbon formation to cracking only and simultaneously limits RWGS. This reaction temperature leads to better overall performance and an H_2/CO ratio closer to unity. However, doing so significantly increases the required energy consumption and lowers the economic attractiveness of the process.

2.1.4. Impact of operating conditions

Methane reforming processes are heavily affected by operational conditions —namely, the reaction temperature, feed composition, and operating pressure. Noureldin et al. [17] have studied

the impact of temperature and feed composition on the equilibrium composition of the three main methane reforming techniques (SRM, POM, DRM). The results reported in this study are briefly discussed below.

2.1.4.1. Temperature

These studies were all simulated at an operating temperature of 1 bar in a temperature range of 226.85-1226.85°C. The feed compositions were CH_4:H_2O= 1:1 for SRM, CH_4:O_2=1:0.5 for POM, and CH_4:CO_2=1:1 for DRM.

For SRM, it was reported that CH_4 conversion is favored as the temperature increased to 1026.85°C. Similarly, H_2 and CO production are also favored. After this temperature, no significant difference was observed in both yield and conversion. Furthermore, increasing temperature decreases CO2 and solid carbon production while increasing the H_2:CO ratio to the expected stoichiometric ratio of 3:1, increasing up to 4.

In the case of POX, a similar trend to SRM was observed. Increasing operating temperature increases the conversion of CH_4, and the production rate of H_2, and CO, where performance plateaus around 1026.85°C. Simultaneously, the production of CO_2 and H_2O was lower, and solid carbon generation is impeded. The H_2:CO ratio approaches the theoretical limit of 2:1.

As for DRM studies, a similar behavior to SRM and POM was presented. Production of CO and H_2 increases with temperature. Solid carbon formation is reduced with higher temperatures. However, the results showed that the required temperature for the inhibition of carbon formation in DRM was approximately 200°C higher when compared with the SRM requirement. Finally, the H_2:CO ratio approached 1:1, the lowest amongst all methane reforming techniques.

2.1.4.2. Feed Composition

SRM studies were conducted at 1 bar in a temperature range of 226.85-1226.85°C. It was reported that CH_4 conversion and hydrogen production increased with increasing steam content in the feed. Furthermore, higher steam content inhibited the formation of solid carbon. However, it reduced steam conversion, lowered CO production, and increased CO_2 generation. This trend's root cause was attributed to the favored water-gas shift reaction, which competes with the SRM reaction. It was also reported that a lower temperature requirement for complete methane conversion was noticed as steam content in the feed was increased. Noureldin et al. [17] established a clear trade-off between the benefits of higher steam content in the feed and the required energy input.

POX calculations were performed under a pressure of 1 bar under the same temperature range of SRM. As the oxygen content in the feed increases, CH_4 conversion increases while H_2 and CO production decreases. This was attributed to an increased occurrence of complete combustion, which produces CO_2 and H_2O. Contrary to SRM, POX is exothermic, which means higher oxygen content in the feed releases heat. This imposes a significant safety risk due to potential hot spot formation and runaway reactions. Higher oxygen content inhibits the production of solid carbon and enables operation at lower temperatures.

Concerning DRM, similar trends are observed for an operating pressure of 1 bar and an identical temperature range. Increasing CO_2 in the feed increases CH_4 conversion, as seen for both SRM and POM. However, increasing CO_2 feed decreases H_2 production while CO production increases. This trend was attributed to the dominance of the RWGS reaction. Finally, increasing CO_2 in the feed significantly increases the required energy input since the reaction is endothermic.

2.2. Role of Catalysts

Before delving into the specific catalytic systems studied for DRM, a brief discussion of catalyst structure and role shall be presented.

2.2.1. Heterogeneous Catalyst Structure

A catalyst is a material that increases the reaction rate by mediating the pathway without being consumed. It is important to note that all catalysts involved in this discussion fall under what is known as heterogeneous catalytic systems. These catalysts are different in a phase from the reactants or products—catalysts in the same phase as the reactants are homogenous catalysts.

Heterogeneous catalysts consist of three main building blocks, the active site, the support, and the promotor. The active site is where the reaction primarily takes place. These sites promote the reaction rate and help in controlling product selectivity. When reacting molecules adsorb on the active site, temporary chemical bonds are formed. This process significantly reduces the activation energy of the reaction, consequently increasing the reaction rate. The strength of the interaction between the reactant and the active site is critical. If the interaction's strength is too high, the site is blocked, and the catalyst deactivates through poisoning.

On the other hand, if the interaction is weak, the active site cannot facilitate intermolecular bonds' breakage, and the activation energy is not reduced. The choice of the active site is critical to control the selectivity of the reaction. Specific side reactions are suppressed depending on which reaction route is promoted, and particular product selectivity increases [18].

The support is the structure on which the active material is dispersed. The support is mainly used to enhance the textural properties of the catalyst. It has been established that the greater the number of exposed active sites, the higher the performance. This puts into perspective the

importance of choosing a support with a high surface area to increase the number of available active sites. Furthermore, thermal stability, chemical stability, and mechanical strength are additional properties of interest when selecting a support. The support is typically the primary component of a catalyst. It can either act as an inert material or even contribute to the catalytic activity. When the support interacts strongly with the active material metal (SMSI), an evident influence on the reaction is observed. Specific supports contain acid-base sites, which contribute to the chemistry of the process. Also, the porous structure of the support can significantly impact the selectivity of the reaction, as is the case in zeolites. The pore size can dictate the diffusion of the reactants and steer the reaction towards specific products.

Promoters are primarily metals added to improve catalytic performance. In most cases, these substances have little to no impact on the reaction by themselves. However, when added to catalysts, they can drastically alter the course of the reaction. Texturally, these metals can separate active sites from each other to reduce sintering. Furthermore, structural and electronic promoters can change the catalyst's crystal and electronic structure to improve catalytic performance.

2.2.2. Catalysts for DRM

A large number of scientific studies show that noble metal-based catalysts are active and stable in DRM. Wang et al. [19] studied the impact of the support on Rh-based catalysts in DRM. They have reported that reducible oxides such as SiO_2 and Y_2O_3 perform poorly when used as supports, resulting in declining conversions and yields. The authors detail that MgO and Al_2O_3 presented high activities and more stable performances. Tsyganok et al. [20] have developed an efficient and simple method for synthesizing precious metal catalysts utilizing an Mg-Al mixed oxide as a support. They have reported that these catalysts present high and stable conversions of CH_4 and CO_2 in DRM at 800 °C. A summary of the findings of the literature mentioned above

and other studies is shown in Table 1. However, these systems are not desired as the low abundance of these metals causes their price to be higher than the limit at which DRM is economically feasible. On the other hand, non-noble metal-based systems have shown comparable performances at a cheaper and more desirable price point due to their much higher abundance. Unfortunately, these systems are hindered by their rapid deactivation due to carbon formation on the catalyst active site, otherwise known as coking.

This predicament has propelled most of the research on DRM to improve the performance of these catalytic systems. Nickel-based systems are by far the most heavily investigated in this regard due to their promising initial activity. Table 2 includes the results of DRM literature studies that used monometallic Ni systems.

Table 1:DRM performance of noble metal systems in the literature

Active Metal	Support	Preparation Technique	Temperature (°C)	CH_4 Conversion (%)	CO_2 Conversion (%)	H_2/CO	Time on Stream	Reference
Rh	γ-Al_2O_3/MgO	Imp	800	82	87	-	50 h	[19]
Ir	$MgAlO_x$	-	800	95	97	-	6 h	[20]
Ru	$MgAlO_x$	-	800	95	97	-	50 h	[20]
Pt	γ-Al_2O_3	-	700	65.5	76.1	0.68	-	[21]

Table 2:DRM performance of monometallic nickel systems in the literature

Active Metal	Support	Preparation Technique	Temperature (°C)	CH_4 Conversion (%)	CO_2 Conversion (%)	H_2/CO	Time on Stream	Reference
Ni	γ-Al_2O_3	Imp	800	85	87	0.88	66 h	[22]
Ni	γ-Al_2O_3	Sol-gel	800	90	94	0.81	48 h	[23]
Ni	CeO_2	Facile prec.	700	72.8	79.1	0.85	85 h	[24]
Ni	γ-Al_2O_3	I Imp	670	72	80	0.83	100 min	[25]

2.2.3. Ni-Cu Literature Survey

A few studies were available in the literature investigating the impact of copper introduction into the Ni/Al_2O_3 system. Rahemi et al. investigated the impact of plasma treatment on $Ni\text{-}Cu/Al_2O_3$ catalysts [26]. The authors have reported that although plasma treatment enabled syngas production at a lower temperature, catalysts prepared by impregnation with no plasma treatment presented better stability attributed to the smaller NiO particles formed.

Wu et al. synthesized $Ni\text{-}Cu/SiO_2$ and Ni/SiO_2 catalysts using Phyllosilicate and impregnation methods [27]. Their work showed that catalysts synthesized using the phyllosilicate technique exhibited a noticeable improvement in conversion and stability compared with impregnation variants. Bimetallic catalysts presented a slightly higher conversion compared to monometallic counterparts. The superior performance of phyllosilicate catalysts was credited to the high surface area, good dispersion of alloy nanoparticles, and strong metal-support interactions.

Sutthiumporn et al. reported the performance of $La_{0.8}Sr_{0.2}Ni_{0.8}M_{0.2}O_3$ perovskite catalysts in DRM [28]. Catalysts were designed with various M groups, including Bi, Co, Cr, Cu, and Fe. All catalysts were prepared using the sol-gel method. Amongst all catalysts, the Cu doped variant showed the highest initial activity. However, at around 10 h time on stream, the Fe doped catalyst matches the CH_4 conversion of the Cu variant and surpasses it after that point. This behavior was explained by the noticeable carbon formation on the Cu catalysts, as shown by TGA. The Fe variant has shown a clear superiority in terms of coke resistance.

2.3. Catalyst Synthesis Techniques

A critical decision in catalyst synthesis is choosing an appropriate preparation technique. Texturally, each preparation technique can result in different properties such as surface area and

dispersion of active sites. Also, specific preparation techniques are characterized by their unique chemistry reflected in the synthesized catalyst.

In this section, the three main preparation techniques implemented in this study will be discussed. Furthermore, a brief discussion of other preparation techniques will be presented.

2.3.1. Impregnation

Impregnation is the simplest and most widespread method in preparing a heterogeneous catalyst. In impregnation, a solution containing the active species precursor is used to wet a solid support which usually has a high surface area. The relationship between the impregnation liquid volume and the support's pore volume decides which type of impregnation occurs. In typical wet impregnation (WI), the liquid volume is larger than the supports pore volume. If the liquid volume is equal to or less than that of the pore volume, the technique is classified as incipient wetness impregnation (IWI) of dry impregnation [29].

In IWI, the weight of active material to be added onto the support is easier to control. However, there are several notes to mention. Since the volume of active metal liquid is equal to or less than the support pore volume, the larger pores will take up more fluid. Depending on the support's pores' uniformity, this may result in a non-uniform distribution of the active material and subsequently to larger crystal sizes. Furthermore, careful drying of the catalyst must be performed. If not done correctly, active sites' concentration might be higher at the pore mouth or even at the catalyst's surface.

It is important to note that using WI to impregnate a support with a low concentration of active material is challenging. The low concentration of active material in the impregnation fluid may result in a complete deposition at the pore mouth rather than the bulk. This can be

advantageous in specific reactions which are pore diffusion-limited. However, for kinetically limited reactions, this can be a significant drawback [30].

2.3.2. Coprecipitation

The principle of this method is to induce the precipitation of a solid from a liquid solution. This process is carried out in three fundamental steps, which are supersaturation, nucleation, and growth.

Supersaturation can be achieved by several routes, as illustrated in Figure 1. The objective in this step is to approach supersaturation. A decrease in temperature would shift the system from A to B. Alternatively, increasing the concentration would take the system from A to C. The most common approach in some systems is to move the saturation curve to D by increasing the pH placing A in the supersaturated region. Once in the supersaturated region, the system becomes unstable, and precipitation occurs via minor perturbation [31].

At this stage, nucleation commences, where the smallest fundamental particles begin to form. During growth, the formed particles begin to agglomerate. If the system is highly supersaturated, the rate of growth is trumped by the rate of nucleation. This results in the formation of multiple small particles which are amorphous. This phenomenon highlights the necessity to carefully control the conditions under which the preparation is performed to obtain uniform particles [31].

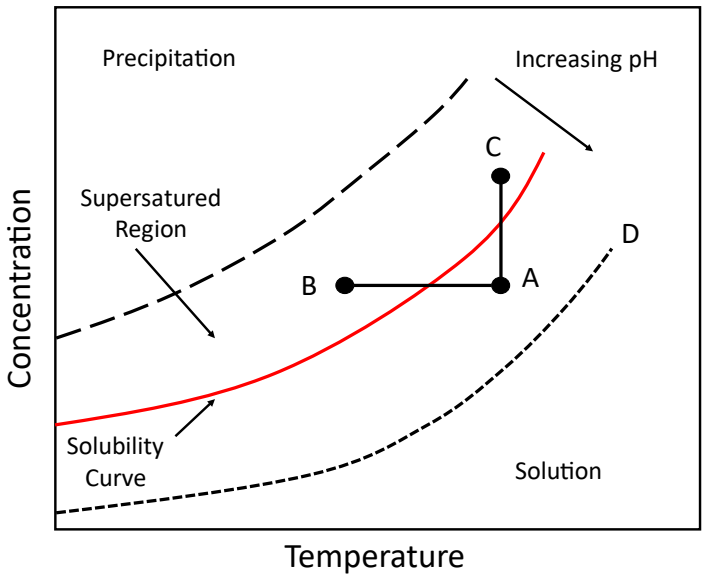

Figure 1: Dependence of Supersaturation on Temperature, Concentration, and pH (adapted from[31])

2.3.3. Sol-Gel

The sol-gel technique dates to 1970. Initially, it was adopted as a low-temperature method to synthesize ceramics and glasses. Around 1995, it began to catch the attention of individuals specializing in materials for electronics, mechanical parts, and chemistry [32]. This technique has the versatility to produce an array of materials, including monoliths, foams, and fibers. Furthermore, sol-gel does not require the implementation of expensive technologies or the use of powder intermediates.

A "sol" consists of colloidal particles which are stable inside a solution. These particles can have varying characteristics, from crystalline to amorphous. Texturally, they may be dense or porous. A "gel" is a solid network that is porous and three-dimensionally continuous. This network surrounds and supports a continuous liquid phase [33].

There are different variations to the sol-gel technique. Traditional sol-gel routes are well established and are often referenced as "Hydrolytic" sol-gel routes. More recent methods have implemented "Non-Hydrolytic" routes.

Traditional sol-gel can be summarized in the following steps [34]:

i. Sol synthesis via hydrolysis and partial condensation of alkoxides.
ii. Gel formation through polycondensation, leading to the creation of metal–oxo–metal or metal–hydroxy–metal bonds.
iii. Gel network Condensation (Aging). In general, this results in shrinkage and explosion of solvent.
iv. Gel drying. Supercritical drying causes aerogel formation while porous network collapse forms a dense 'xerogel.'
v. Removal of surface M–OH groups by calcination at high temperature.

The critical steps in sol-gel chemistry are presented in Eqs.10-12 [35]. The first critical reaction is the hydrolysis of the alkoxy group presented (Eq.10). The second critical rection is the condensation of the alkoxide MOR group (Eq.11). Finally, mixed condensation of OH and alkoxy groups occurs (Eq.12).

$$MOR+HOH\leftrightarrow MOH+ROH \quad \textbf{(10)}$$

$$MOH+MOH\leftrightarrow MOM+HOH \quad \textbf{(11)}$$

$$MOH+MOR\leftrightarrow MOM+ROH \quad \textbf{(12)}$$

Most alkoxides used in sol-gel are based on p-block elements such as Al or Si or transition metals such as Ti or Zr. In hydrolytic sol-gel, the nature of the R group in the alkoxide used can significantly affect the synthesized product. Other parameters include the ratio of water to alkoxide and the concentration of catalysts [34].

2.3.4. Other Catalyst Preparation Techniques

Several arising techniques were investigated in recent literature. Melt infiltration or solid-state impregnation is an example of these said techniques. In this method, the metal precursor salt is mixed with the desired support. This mixture is then heated up to the melting temperature of the

salt. Upon melting, the formed liquid diffuses into the pores of the support. A critical condition in this technique is the choice of precursor. The metal precursor's decomposition and melting temperatures must be adequately apart to ensure a good end product. This method has presented relative success when utilizing transition-metal nitrate hydrates. These substances have low melting temperatures where it occurs within their crystal water [36].

Colloidal synthesis is another emerging technique. This method's appeal resides in its ability to control nanoparticles' size, shape, and composition in the liquid phase. The formation of nanoparticles occurs through gradually invoking change in the system containing a homogenous metal precursor solution. This procedure commences nucleation followed by nanoparticle growth. The most pressing difficulties associated with this technique are the deposition of active material on support structures and ligand removal [36].

Potentially the most exciting among the emerging preparation technique is Atomic Layer Deposition (ALD). In this technique, molecules in the gas phase react in an irreversible and self-limiting manner with a surface. This results in the uniform formation of a monolayer. Typically, the precursor is present within the vapor phase reacting with the support surface. The surface is then purged and reacted with oxygen or hydrides of the non-metal elements. This step is performed to generate metals, metal oxides and regenerate surface sites. This procedure can be repeated multiple times to increase the deposited film's thickness in a layer-by-layer manner. Furthermore, an extension of this technique can be utilized to stabilize the formed nanoparticles [36].

3. METHODOLOGY

3.1. Catalyst Characterization

3.1.1. Powder X-ray Diffraction (PXRD)

For this study, a Rigaku Smart Lab X-ray diffractometer with Cu Ka radiation (λ = 1.5418Å) was used at instrument settings of 40 kV and 30 mA. The scan range was set from 3° to 90° with a step size of 0.020/second.

The Scherrer equation (Eq.13) was used to calculate the crystallite size of the active metal particles.

$$D = \frac{b2\pi}{FWHM(Q)} \qquad \textbf{(13)}$$

D is the dimension of the crystallites as if they were cubes, monodisperse in size. Q is the wavelength, b is a constant, which generally takes a value between 0.89 and 0.94 depending on the function used to fit the peak, and FWHM is the full-width half maximum of the peak presented in (Eq.14) [37].

$$FWHM(2\theta) = \frac{b\lambda}{D\cos\theta} \qquad \textbf{(14)}$$

λ is the wavelength, b and D are the same variables present in (Eq.13), and θ is Braggs angle.

3.1.2. H_2- Temperature Programmed Reduction (TPR)

H_2- Temperature programmed reduction (TPR) is a handy characterization tool to investigate metal oxide reduction behavior over fresh calcined catalysts. H_2-TPR was carried out in AutoChemII 2920 (Micrometrics) equipment connected with a TCD detector to monitor H_2-consumption. The samples were pretreated at 150 °C under He flow rate for 120 min and then

cooled down to ambient temperature. Then flow 10% H_2/Ar gas (50mL/min) by heating the samples from 50 °C to 900 °C with 10 °C/min ramp rate and the hold 30 min at 900 °C until no more H_2- consumption was observed.

3.1.3. Scanning Electron Microscopy (SEM)

A JEOL 7800F attached with an Oxford XMAX EDS was used for SEM analysis. An acceleration voltage of 10 kV was used to obtain the images using a backscattering electron detector, whereas 15 kV was used for EDS. The samples were not coated to observe the atomic number contract from the nanoparticles. As for bulk EDS analysis, samples were pressed onto an adhesive carbon tape, and a large area was chosen.

3.1.4. Transmission Electron Microscopy (TEM)

The TALOS F200X TEM coupled with SUPERX EDS was used for this study. The samples were dispersed in t isopropyl alcohol and sonicated for 10 minutes. 20 µl of the dispersed solution was dropped over a 300 Mesh Holey carbon Molybdenum grid and dried at room temperature. 200 kV acceleration voltage was used to obtain the images.

The software ImageJ was used to collect the particle sizes of the dispersed nickel active sites for statistical assessment.

3.1.5. X-ray Photoelectron Spectroscopy (XPS)

A state-of-the-art ESCALAB 250 XPS platform was used with a mono-chrominated x-ray source energy of 1486.6 eV. The incident beam was 45° to the surface normal of the sample. The total energy resolution was better than 0.5 eV. The samples were mounted on conducting carbon tape, and the surface spectra were performed with a step size of 1 eV. The core-level spectra were carried out with a step size of 0.1 eV. All the body energy was calibrated to the C-C at 284.8 eV in the C_{1S} spectra.

3.1.6. Thermogravimetric Analysis and Dynamic Scanning Calorimetry (TGA-DSC)

A TA Instruments SDT Q800 was used to study quantify and study the carbon content in the sample. Approximately 5 mg of each sample were introduced into an alumina crucible. The crucibles were then placed into the oven chamber, which was heated to 900 °C at a rate of 10°C /min. The chamber was subjected to a continuous purge of 50 ml/min (10% O_2, 90% N_2).

3.1.7. Inductively Coupled Plasma - Optical Emission Spectrometry (ICP-OES)

The actual metal loading of the catalysts was measured by Inductively Coupled Plasma–Optical Emission Spectroscopy (ICP-OES) on a PlasmaQuant 9000 device (Analytik Jena). 10 mg of each sample was weighed, and 2 mL of concentrated H_2SO_4 added. After heating to 250 °C and holding for 1 h, increased temperature to 300 °C and held for 30 min until completely dry. After cooling to room temperature, 2 ml each of concentrated HCl and HNO_3 was added, and the mixture heated to 150°C. After 10 - 20 min of heating, the sample is cooled, and deionized water was added to make up the required volume before performing ICP-OES.

3.1.8. BET-SA

The BET-SA measurements of fresh calcined catalyst were carried out at -196.15°C with liquid N_2 (Micromeritics Tri-Star II 3020). Before the analysis, samples of about 100 mg were degassed at 200°C for 12 h in a flow of helium gas. The surface area was calculated using the BET equation, whereas the total pore volume and average pore radius were obtained from the Barrett-Joyner-Halenda (BJH) method.

3.1.9. CO Chemisorption

CO chemisorption was conducted in the AutoChem II 2920 (Micromeritics) instrument attached with a TCD detector. The fresh calcined samples were loaded in a U-shaped quartz vertical reactor tube. The samples were reduced with 10% H_2/Ar at 650 °C for 2h, flushed with He

gas, and cooled down to 40 °C. At this temperature, 0.01778 $cm^{3,}$ each of a 5%CO/He mixture was injected into the sample via a calibrated loop until saturation of the peaks is observed. The metal dispersion was calculated based on the amount of CO adsorbed on the catalyst surface.

3.2. Catalyst Synthesis

3.2.1. Incipient Wetness Impregnation

Nickel nitrate hexahydrate ($Ni(NO_3)_2$•$6H_2O$, Sigma Aldrich) and Copper nitrate hemi (pentahydrate) ($Cu(NO_3)_2$ •$2.5H_2O$, ACROS) were used as Ni and Cu precursors respectively, and γ-Al_2O_3 (Sasol Puralox) powder as the support. All reagents were used without further purification. The required amount of Ni $(NO_3)_2$•$6H_2O$ precursor was dis- solved in deionized water, which is equal to the pore volume of support (γ-Al_2O_3) and then added to support by incipient wetness impregnation to obtain the desired Ni loading (10 wt% Ni). The impregnated support was then transferred into a porcelain crucible and kept in an oven for drying at 110 °C for 12 h in static air. The dried catalyst was calcined in stagnant air at 600 °C for 5 h in a muffle furnace with a temperature ramp of 1 °C/min.

For the bimetallic catalysts, the same procedure was followed. Bi-metallic Ni-Cu/Al_2O_3 catalysts were also prepared by the conventional co-incipient wetness impregnation method. The required amount of both $Ni(NO_3)_2$•$6H_2O$ and $Cu(NO_3)_2$•$2.5H_2O$ were used as metal-precursors to obtain a nominal metal (Ni + Cu) loading of 10 wt.%. The Ni: Cu atomic ratio was fixed to 3:1(higher Cu loading), 8:1(medium Cu loading), and 10:1 (Lower Cu loading), respectively. After mixing the precursor aqueous solutions with the γ-Al_2O_3, the mixtures were then dried at 110 °C for 12 h. The dried catalyst was then subjected to calcination in static air at 600 °C for 5 h in a muffle furnace with a temperature ramp of 1 °C/min. In this report, we have denoted the three bimetallic catalysts as Ni_3Cu_1/Al_2O_3-IWI (Ni/Cu atomic ratio = 3/1, ‘high’ Cu loading),

Ni_8Cu_1/Al_2O_3-IWI (Ni/Cu atomic ratio = 8/1, 'medium' Cu loading), and $Ni_{10}Cu_1/Al_2O_3$-IWI (Ni/Cu atomic ratio = 10/1, 'low' Cu loading).

3.2.2. Sol-Gel Synthesis

First, the appropriate amount of $Al(NO_3)_3 \cdot 9H_2O$ (Sigma-Aldrich) was mixed with ethanol and water. Then, NH_4OH solution (30wt%,15M) was added drip-wise to the mixture to form the sol. Following precipitation, the sol was agitated for 24 h at 85 °C inside an oven. After agitation, the sol was washed twice with DI water. Nickel nitrate hexahydrate ($Ni(NO_3)_2 \cdot 6H_2O$, Sigma Aldrich) was then added in the amount needed to achieve 10wt% loading. The doped sol was then stirred for 30 min and placed in an oven for 24h of aging at 85 C and then drying for 24 h at 110°C. The dried gel was calcined for 5 h at 600 °C, with a heating rate of 1 °C/min. The produced catalyst is referenced as Ni/Al_2O_3-SG in the remainder of the report.

The same procedure was followed for the bimetallic catalyst. The appropriate amount of $Al(NO_3)_3 \cdot 9H_2O$ (Sigma-Aldrich) was mixed with ethanol and water. Then, NH_4OH solution (30wt%,15M) was added dropwise to the mixture to form the sol. Following precipitation, the sol was agitated for 24 h at 85 °C inside an oven. Nickel nitrate hexahydrate ($Ni(NO_3)_2 \cdot 6H_2O$, Sigma Aldrich) and $Cu(NO_3)_2 \cdot 6H_2O$ were used as metal-precursors to obtain a nominal metal (Ni + Cu) loading of 10 wt.% and a Ni: Cu atomic ratio of 8:1 (medium loading). The dopped sol was then stirred for 30 min and placed in an oven for 24 h of aging at 85 °C and then drying for 24 h at 110°C. The dried gel was calcined for 5 h at 600 °C, with a heating rate of 1 °C/min. The produced catalyst is referenced as Ni_8Cu_1/Al_2O_3-SG in the remainder of the report.

3.2.3. Co-precipitation Synthesis

The monometallic catalyst was synthesized by first mixing the appropriate amount of ($Ni(NO_3)_2$•$6H_2O$, Sigma Aldrich), $Al(NO_3)_3$•$9H_2O$ (Sigma-Aldrich), and DI water to achieve a nominal metal loading of 10 wt.% Ni. The solution was stirred at 40°C and precipitated by adding NH_4OH solution (30wt%,15M) dropwise. The critical step of the precipitation was achieving a final pH of 8. The precipitates were filtered and washed with DI water and then dried at 110 °C overnight in an oven. The last step was calcination at 600 °C for 5 h with a heating rate of 1 °C/min. The synthesized catalyst is referenced as Ni/Al_2O_3-CP in the remainder of the report.

The bimetallic catalyst was synthesized in the same manner. The appropriate amount of ($Ni(NO_3)_2$•$6H_2O$, Sigma Aldrich), $Cu(NO_3)_2$•$6H_2O$, $Al(NO_3)_3$•$9H_2O$ (Sigma-Aldrich) and DI water were mixed to achieve a nominal metal loading of 10 wt.% and a Ni: Cu atomic ratio of 8:1 (medium loading). The solution was stirred at 40°C and precipitated by adding NH_4OH solution (30wt%,15M) dropwise to achieve a pH of 8. The precipitates were filtered and washed with DI water and then dried at 110 °C overnight in an oven. The final step was calcination at 600 °C for 5 h with a heating rate of 1 °C/min. The synthesized catalyst is referenced as Ni_8Cu_1/Al_2O_3-CP in the remainder of the report.

3.3. Activity Testing

CO_2 reforming of methane for IWI catalyst was examined in a Microactivity-Efficient benchtop reactor (Micromeritics) using a vertical quartz reactor (i.d. 9 mm) at atmospheric pressure. For catalytic activity and stability tests in the first section of the study, the reaction was carried out at 650 °C for 10 h over 5.5 mg of catalyst and 100 mg SiO_2 diluent. 10 % CH_4/10 % CO_2/80 % He (reactant gas) and hydrogen (reducing gas) were purchased and used as-is from National Industrial Gas Plants, Qatar. Before reaction, the catalyst was reduced in-situ with pure

H_2 (50 ml min^{-1}) at 650 °C for 1 h. Subsequently, the catalyst was cooled down to the targeted reaction temperature in Helium before the introduction of reactant gas. The reactant gas composition was (10 %CH_4:10 % CO_2: 80 %He), and the total flow rate was 30 ml min^{-1}. The effluent gas was analyzed online by a Cirrus 2 Mass spectrometer (MKS Instruments). For long-time on-stream testing, identical parameters were used at a longer reaction time of 70 h. In the second part of the study, the short time on stream testing was extended to 20 h, while the long time on stream was kept at 70 h while maintaining the exact protocol utilized for previous tests. It is important to note that the catalyst mass used for testing in this study section was increased to 20 mg for short TOS tests and 50 mg for long TOS tests. This was done to obtain a larger amount of used catalyst and enable further characterization to be performed. Finally, a vertical quartz reactor (i.d. 4 mm) was used in the second section DRM tests. All other conditions and parameters were identical to those implemented in the first section of the study.

4. RESULTS AND DISCUSSION

In this section, the catalyst characterization and the DRM performance results will be presented. The results are split into two main sub-sections. The first sub-section is titled the optimization of copper loading. This section aims to identify and optimize the impact of copper loading on IWI catalysts' performance. The second sub-section is titled investigation of synthesis technique impact. This section seeks to gain insight into how the synthesis technique affects catalyst performance. The results from characterizing and DRM testing monometallic and bimetallic catalysts synthesized by the SG and CP techniques will be presented to achieve this goal. Bimetallic catalysts presented in this section use the optimized copper loading found in sub-section one.

4.1. Section I: Optimization of Copper Loading

The catalysts investigated in this sub-section are all prepared by IWI. These catalysts are Ni/Al_2O_3-IWI, $Ni_{10}Cu_1/Al_2O_3$-IWI, Ni_8Cu_1/Al_2O_3-IWI, and Ni_3Cu_1/Al_2O_3-IWI. The findings from characterizing several fresh catalyst properties using advanced techniques will be presented. The implemented techniques are ICP, BET, H_2-TPR, XRD, Chemisorption, TEM, and EDS. Then, the results of short time on stream (TOS) DRM performance tests will be presented and analyzed for all synthesized catalysts. Next, the long TOS DRM performance results of the best performing bimetallic catalyst and the monometallic reference catalyst are discussed. Finally, the analysis of the used catalysts from these long TOS tests using XRD, TPO, TGA, DSC, SEM, TEM, and EDS are presented and discussed.

4.1.1. Textural Characterization of Fresh Catalysts

Table 3 presents the physicochemical properties of all fresh calcined catalysts. The bare support γ-Al_2O_3 has a BET-SA of 153 m^2/g and an average pore volume of 0.88 mL/g. In

comparison, the metal-loaded catalysts have lesser surface area and pore volume compared to bare γ-Al_2O_3. This could be due to the high metal content (10 wt.%), wherein Ni and Cu particles might block the pores of γ-Al_2O_3 during metal impregnation. The blockage results in a slight decrease in the pore volume of catalysts. Moreover, when all the three bimetallic catalysts $Ni_{10}Cu_1/Al_2O_3$-IWI, Ni_8Cu_1/Al_2O_3-IWI, and Ni_3Cu_1/Al_2O_3-IWI were compared, it was observed that the surface area and the pore volume had very similar values, which makes sense theoretically because the total metal loading was similar in all the catalysts.

Table 3: Physicochemical properties of Ni/Al_2O_3-IWI and bimetallic $Ni-Cu/Al_2O_3$-IWI catalysts

Catalyst	(Ni: Cu) Atomic ratio	Nominal metal loading (wt%)	[a] Ni metal loading (wt%)	BET-SA (m^2/g)	Pore volume (cm^3/g)	[b] NiO crystallite size (nm)	[c] Ni^0 particle size (nm)	[d] Metal dispersion (%)	[e] Ni0 particle size (nm)
γ-Al_2O_3	-	-	-	153	0.88	-	-	-	-
Ni/γ-Al_2O_3-IWI	-	10	9.58	132	0.77	10	11	8	9 (9.5)[f]
$Ni_{10}Cu_1$/γ-Al_2O_3-IWI	10:1	10	9.02	138	0.87	7.4	9	6	-
Ni_8Cu_1/γ-Al_2O_3-IWI	8:1	10	8.20	132	0.83	6.5	7	3	4 (7.2)[f]
Ni_3Cu_1/γ-Al_2O_3-IWI	3:1	10	7.34	133	0.80	8.4	10	2.5	-

[a]Estimated from ICP-OEC,
[b]Calculated for XRD fresh calcined samples by using Scherrer's equation
[c]Calculated for XRD fresh reduced samples by using Scherrer's equation
[d]From CO chemisorption, refer to text for explanation
[e]From TEM analysis of reduced catalysts
[f]From TEM analysis of spent catalysts

4.1.1. H_2-Temperature Programmed Reduction (TPR)

Figure 2 shows the H_2-TPR profile of fresh calcined monometallic Ni and Ni-Cu bi-metallic catalysts supported on γ-Al_2O_3. The monometallic Ni/γ-Al_2O_3-IWI (Figure 2(a)) exhibited broad multiple reduction peaks in the range from 500 °C to 800 °C. The low-temperature reduction peak at 570 °C corresponds to NiO weakly interacting with the support ('bulk NiO'), and the high-temperature range peaks to strongly interacting NiO and $NiAl_2O_4$ species. The presence of multiple reduction peaks may be attributed to the presence of different NiO_x species, produced due to

varying interactions with γ-Al_2O_3 [38]. The reduction profiles of the bimetallic Ni-Cu/Al_2O_3-IWI catalysts are shown in Figure 2(b-d), highlighting the differences in reduction behavior as opposed to their monometallic counterparts. Amongst all the bimetallic Ni-Cu catalysts, the higher Ni: Cu atomic catalyst, i.e., Ni_3Cu_1/Al_2O_3-IWI, (Figure 2(d)) exhibits three significant reduction peaks at relatively lower temperatures. The peak at 204 ℃ can be ascribed to the reduction of bulk CuO [39]; the peak located at 400 ℃ can be assigned to the reduction of NiO that is strongly interacting with CuO; the reduction peak above 730 ℃ can be assigned to the reduction of $NiAl_2O_4$ species [38]. It is interesting to note that the low-temperature peak at 240 ℃ in the high Cu-loaded catalyst (Figure 2(d)) disappears as Cu loading decreases (Figure 2(b) and (c)), implying the complete incorporation of Cu^{2+} into the NiO framework via NiCu alloy formation [40,41]. Furthermore, the high-temperature peaks (> 700℃) in the mono-metallic Ni catalysts appear to have decreased in intensity and shifted to lower temperatures, signifying Cu's effect on reducing nickel aluminate spinel formation. These observations are corroborated by other investigators who noted that the presence of Cu could accelerate Ni reducibility [42]. The obtained results indicate that the difference in the reduction behavior mainly depends on metal-support interaction and metal-metal interactions in alloys.

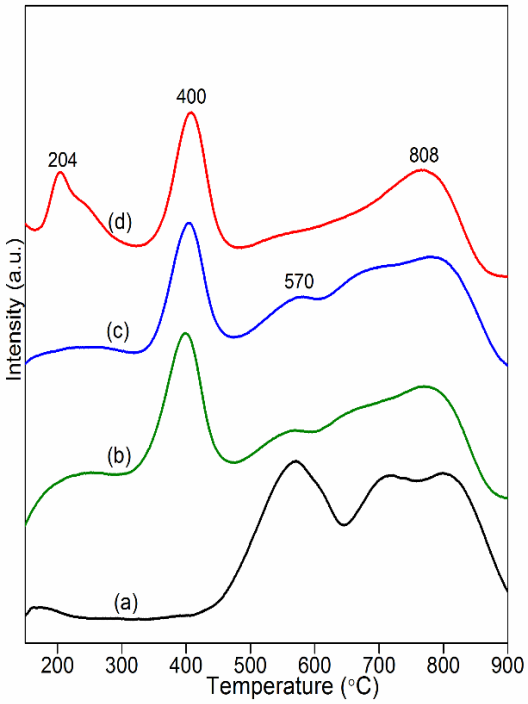

Figure 2: H_2-TPR analysis of fresh calcined (a) Ni/γ-Al_2O_3-IWI, (b) $Ni_{10}Cu_1$/γ-Al_2O_3-IWI, (c) Ni_8Cu_1/γ-Al_2O_3-IWI and (d) Ni_3Cu_1/γ-Al_2O_3-IWI samples.

4.1.2. XRD Analysis of Fresh Calcined and Reduced Catalyst Samples

XRD patterns of fresh calcined monometallic Ni and bimetallic Ni-Cu samples are provided in Figure 3. The XRD pattern of calcined monometallic Ni/γ-Al_2O_3-IWI has prominent diffraction peaks at 2θ = 37.2°, 45.5°, 60.2°, and 66.6° which can be attributed to a mixture of both $NiAl_2O_4$ and γ-Al_2O_3 phases. The reflections at 2θ = 43.3°, 66.9°, and 75.4° are assigned to the fcc NiO [43,44]. The average crystallite size, as calculated by the Scherrer equation, is 11 nm. The calcined bimetallic NiCu catalysts also show peaks in very similar 2θ positions. However, broader NiO diffraction peaks were also observed at 2θ = 43.3°, 64.3° and 75.3° corresponding to an average crystallite size of 6-8 nm, which is lower than that for the monometallic catalyst (Table 3**Error! Reference source not found.**). One possible explanation is that CuO may help stabilize the NiO via the formation of a NiO-CuO solid solution during calcination, thus preventing agglomeration and formation of larger crystallites. Both CuO and NiO have similar lattice

structures and can, therefore, readily form a homogenous NiO-CuO solid solution [45,46]. This solid solution subsequently transforms into a Ni-Cu alloy on H_2 reduction and plays a crucial role in enhancing the performance and the stability of the catalyst. No obvious crystalline phases due to CuO, Cu_2O, or other Cu-related phases are detected, probably due to the copper percentage being lower than the X-ray detection limits, or it might because the particles are in an amorphous state. It is worth noting that the diffraction peak intensities corresponding to NiO (2θ = 43.3°, 64.3°, and 75.3°) decrease while peak intensity at 45.5° increases on increasing Cu addition. This suggests a decrease in bulk NiO and a rise in the formation of NiO-CuO solid solution formation, which in turn stabilizes NiO and prevents the formation of larger crystallites during calcination.

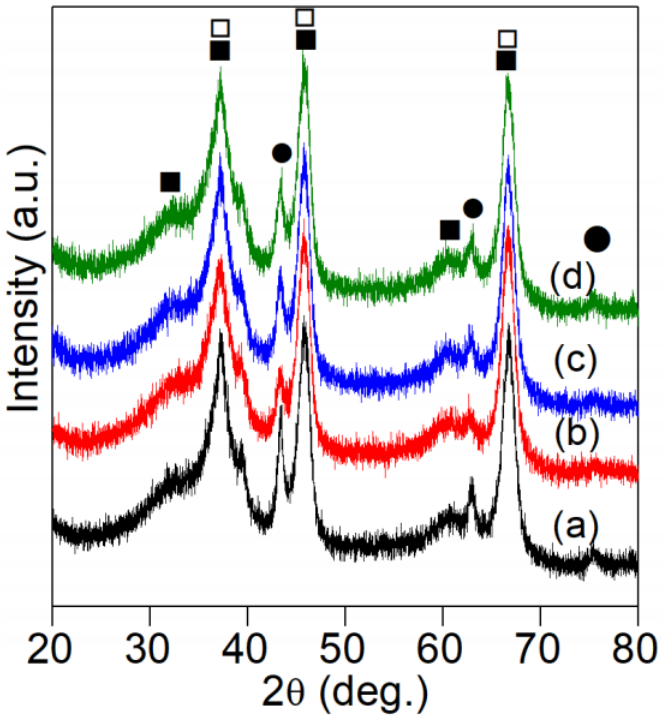

Figure 3: XRD patterns of fresh calcined catalysts. a) Ni/Al_2O_3-IWI, b) $Ni_{10}Cu_1/Al_2O_3$-IWI, c) Ni_8Cu_1/Al_2O_3-IWI, d) Ni_3Cu_1/Al_2O_3-IWI (■: γ-Al_2O_3, ●: NiO, □: $NiAl_2O_4$)

XRD patterns of reduced monometallic and bimetallic catalysts are shown in Figure 4. Reflections at 2θ = 44.4° and 51.7° are attributed to metallic Ni-Cu alloy along with metallic Ni, Al_2O_3, and $NiAl_2O_4$ phases [47]. The Cu-modified catalysts have a smaller crystallite size of 6-8 nm (calculated by the Scherrer equation). In comparison, that of the monometallic catalyst is slightly larger at 11 nm, indicating once again that Ni-Cu alloy formation during reduction stabilizes the crystallites and minimizes agglomeration. These results also validate the assignment of lower temperature H_2-TPR peaks of the Ni-Cu/Al_2O_3-IWI catalyst (Figure 2(b)-(d)) to strong Ni-Cu interactions.

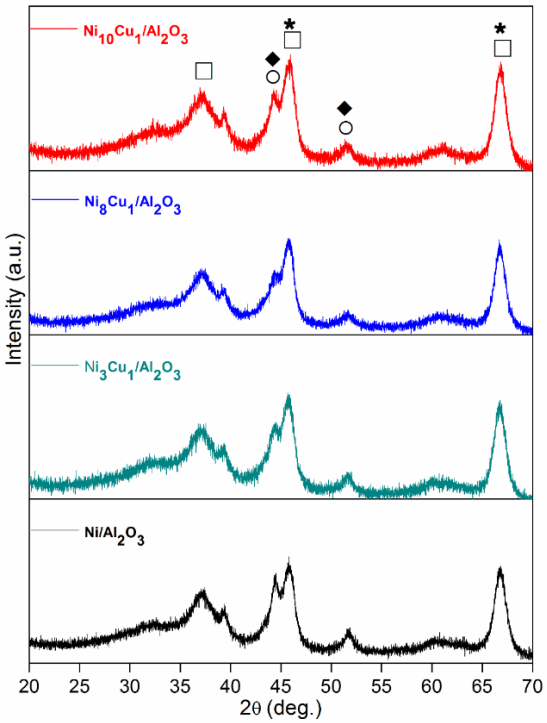

Figure 4: PXRD patterns of reduced catalysts samples. (*: γ-Al_2O_3, ○: Ni^0, ◆: Ni-Cu alloy, □: $NiAl_2O_4$)

4.1.3. Transmission Electron Microscopy (TEM)

TEM analysis for Ni/Al2O3-IWI and Ni8Cu1/Al2O3-IWI catalysts was performed to measure differences in particle sizes between the reduced monometallic Ni and bimetallic catalysts to confirm the formation of Ni-Cu alloy.

Figure 5 depicts representative TEM, HR-TEM, HAADF-STEM images, and elemental maps of the reduced monometallic Ni/Al_2O_3-IWI catalyst. Figure 5(a) shows two kinds of Ni particles, both segregated and well dispersed on the surface. The HR-TEM image of monometallic Ni/Al_2O_3-IWI (Figure 5(c)) illustrates lattice fringes with an inter-fringe distance of 0.20 and 0.183 nm, corresponding to the (111) and (200) planes of metallic Ni [48]. Ni particle dispersion was also observed by high-angle annular dark-field scanning transmission electron microscopy (HAADF-STEM) (Figure 5(d)). A bi-modal particle size distribution plot is observed in Figure 5(e), alluding to the presence of smaller, well-dispersed particles and larger metal agglomerates. The particles range from 2 to 16 nm in diameter with an average size of 9 nm.

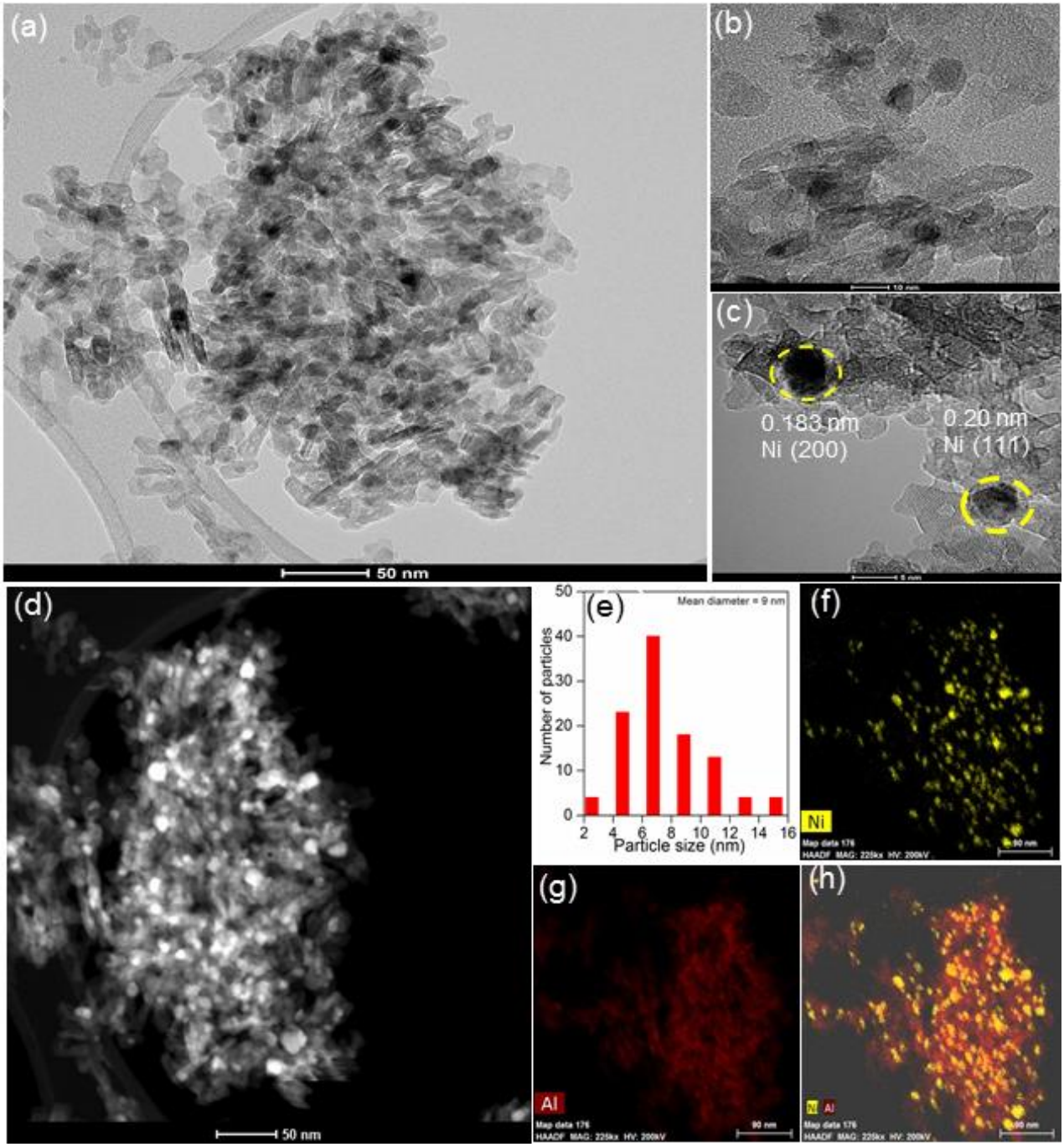

Figure 5: (a) TEM, (b-c) HRTEM, (d) High-angle annular dark-field scanning transmission electron microscopy (HAADF-STEM), (e) Ni metal particle size distribution, and (f-h) Elemental mapping of reduced Ni/Al_2O_3-IWI catalyst.

Figure 6 shows representative TEM and HAADF-STEM images for the reduced Ni_8Cu_1/Al_2O_3-IWI catalyst, chosen because of its higher DRM activity, as described in section 3.2.1. Figure 6(b-e) illustrates the HRTEM image of a representative Ni-Cu alloy nanoparticle with an inter-fringe distance of 0.219 and 0.164 nm, corresponding to (111) and (200) planes of Ni-Cu alloy [27,49]. From the frequency-size distribution (Figure 6g), it is apparent that the metal particles are in the range of 1 to 8 nm with a mean diameter of 4 nm, which is much lower than for the mono-metallic Ni catalyst. The elemental distribution of Cu and Ni, obtained by Energy-Dispersive X-Ray Spectroscopy (EDS) (Figure 6(h-j)), shows the overlapping spatial distributions of both Ni and Cu. This is evidence that Cu is wholly incorporated into the Ni lattice, resulting in distinct Ni-Cu alloy particles [49], agreeing with XRD results. This observation is significant as it directly affects the electronic properties of the active Ni-Cu center, which in turn enhances the catalytic performance.

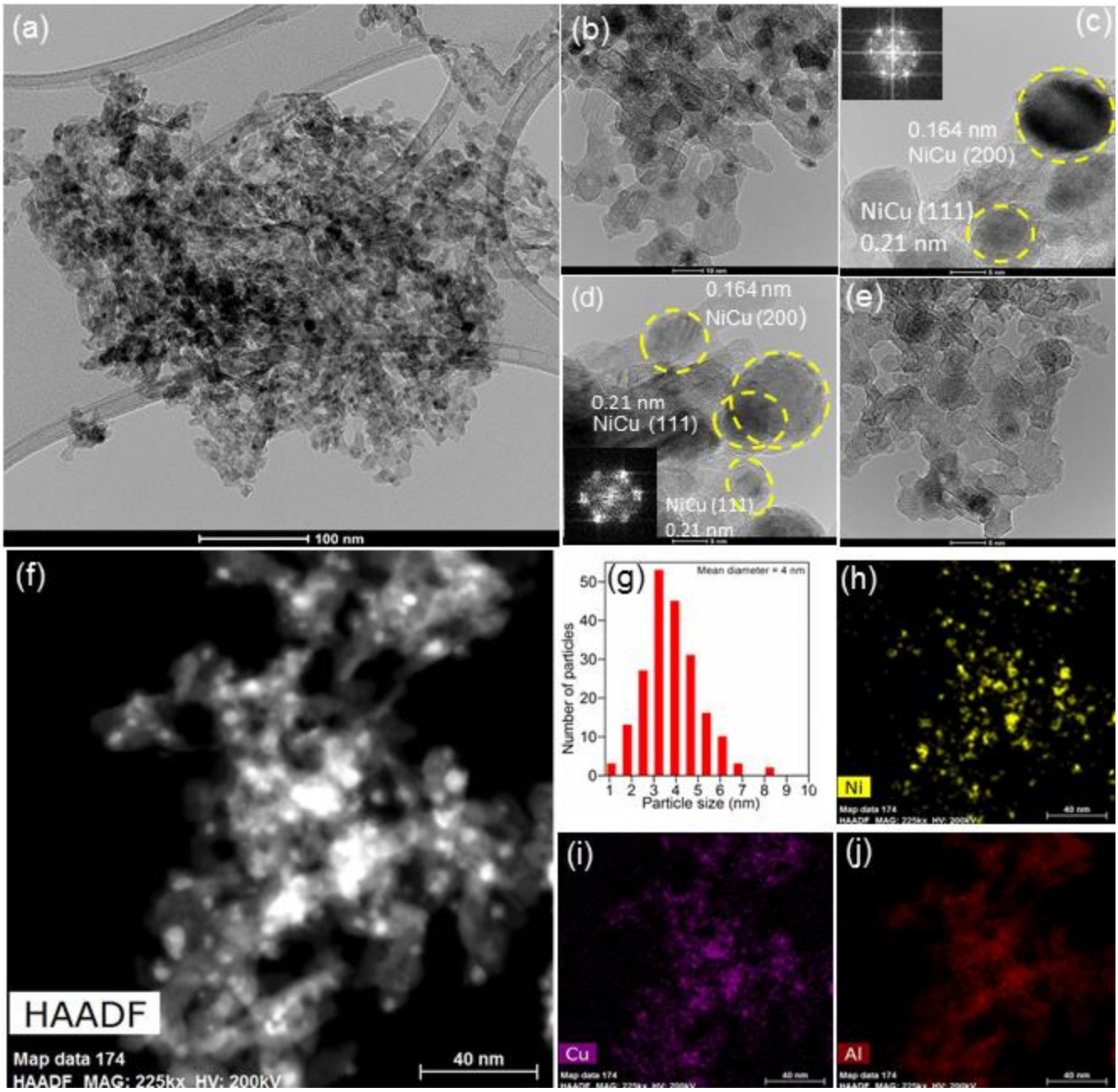

Figure 6: (a) TEM, (b-e) HRTEM, (f) High-angle annular dark-field scanning transmission electron microscopy (HAADF-STEM), (g) Ni metal particle size distribution, and (h-j) Elemental mapping of reduced Ni_8Cu_1/Al_2O_3-IWI catalyst.

4.1.4. CO Chemisorption

CO chemisorption was performed to measure the percentage of active sites exposed on the surface in terms of metal dispersion. The metal dispersion is calculated based on the moles of CO consumed to saturate the surface, in addition to summarizing the physicochemical properties of the calcined and reduced catalysts. Table 3 presents the CO chemisorption results of the reduced Ni and Ni-Cu bimetallic catalysts. Contrary to expectations, the monometallic Ni catalyst provided the highest metal dispersion (8%), while the bimetallic Ni-Cu catalysts showed lower metal dispersions of 2.5%, 3%, and 6%. Since Cu cannot chemisorb CO [39], the Cu-Ni alloy formed may suppress CO chemisorption [50]. The dispersion also decreases with increasing Cu content; an anomaly attributed to the segregation of Cu to the surface at higher loadings. These segregated Cu clusters further lower CO that can be adsorbed, resulting in abnormally lower estimates for metal dispersion.

4.1.5. Catalytic Performance Study for Dry Reforming of Methane

The performance of the prepared catalysts was tested for DRM reaction at 650 °C to investigate the effect of Ni/Cu atomic ratio on the activity and stability of bimetallic Ni-Cu/Al_2O_3-IWI catalysts. The intermediate reaction temperature allows for deactivation via coke formation and sintering, which permits investigation into the influence of Cu addition on mitigating them. The apparent reaction rates of CH_4 and CO_2 (mol/min/g_{Ni}) and H_2/CO ratio are presented in Figure 7(a)-(c).

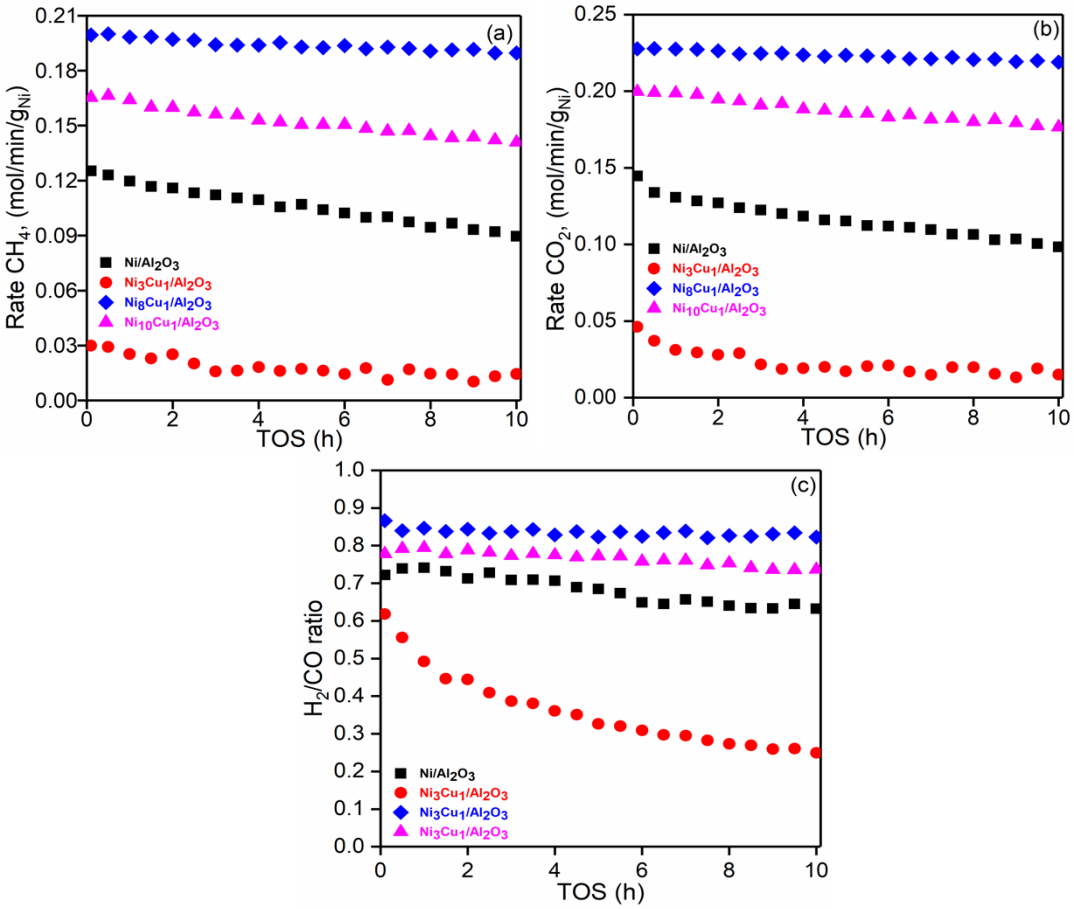

Figure 7: (a) CH_4, (b) CO_2 conversion rates, and (c) H_2/CO ratio versus TOS for CO_2 reforming of methane at 650 °C and 10h TOS. (The DRM activity data collected by a Cirrus 2 Mass spectrometer (MKS Instruments)

For the monometallic Ni/Al_2O_3 catalyst, a higher CH_4 conversion rate of 0.125 mol/min/g_{Ni} and a CO_2 conversion rate of 0.144 mol/min/g_{Ni} was observed, with an H_2/CO ratio of 0.78. As is typical for DRM, the CO_2 conversion rate exceeded that of $CH_4$with the H_2/CO ratio < 1. This is expected since the reverse water gas shift side reaction is also active at this temperature, consuming CO_2 and H_2 to produce CO and H_2O. After 10h time on stream, the reaction rates declined to 0.08 mol/min/g_{Ni} for CH_4 and 0.09 mol/min/g_{Ni} for CO_2. Additionally, the H_2/CO ratio dropped to 0.61, signifying a gradual decline in catalyst activity. As will be discussed in other sections, this is due to a combination of both coke deposition, which encapsulates the catalyst particle and sintering of the metal phase, leading to a reduction in active surface area. For Ni reforming catalysts, sintering is typically presumed to occur within the first few hours of reaction, after which the contribution

of coking to deactivation exceeds that of sintering. In the case of sintering, weak metal-support interactions and the formation of larger particles by atomic or crystallite migration can form segregated Ni clusters. In addition to the loss of active surface area, larger clusters are also susceptible to deactivate more severely by carbon formation since graphitic carbon formation is structure sensitive and occurs readily on crystallites above a critical size [51].

Compared to the mono-metallic Ni catalyst, the addition of Cu below a particular quantity enhances catalyst stability and decreases the deactivation rate for the 10h time on stream. On closer analysis of the three bimetallic catalysts, the one with 'medium' Ni/Cu atomic ratio, Ni_8Cu_1/Al_2O_3-IWI, displayed the highest activity and stability, maintaining almost constant CH_4 and CO_2 conversion rates of 0.20 and 0.23 mol/min/g_{Ni}, respectively. The catalyst with the lowest percentage of Cu, $Ni_{10}Cu_1/Al_2O_3$-IWI, maintained a lower CH_4 consumption rate of 0.16 mol/min/$g_{Ni,}$ later declining slightly to 0.14 mol/min/g_{Ni} over 10h Time-on-Stream (TOS). In addition to a lower deactivation rate, the bimetallic catalysts with 'low' and 'medium' Cu content exhibited better, and more importantly, stable H_2/CO ratios than the monometallic Ni catalyst. Another reason behind the sustained activity of this 'medium' Cu catalyst is the formation of a Ni-Cu alloy, as evidenced from its TPR profile (Figure 2) and TEM-EDS mapping (Figure 6), which limits the extent of coking compared to the monometallic Ni catalyst. It is worth noting that the HR-TEM results indicate a much smaller average particle size for the calcined bimetallic catalyst (Table 3), which helps improve both active phase dispersion and coke resistance. A continuation of this discussion is presented in section 4.

Interestingly, the catalyst with 'high' Cu content, Ni_3Cu_1/Al_2O_3 catalyst (Ni:Cu atomic ratio 3:1), showed meager conversion rates compared to the other Ni-Cu catalysts. A higher amount of copper suppresses DRM catalytic activity almost wholly, an observation corroborated

by previous investigations on Ni-Cu/Al_2O_3 and Ni-Cu/SiO_2 catalysts [52,53]. The excess Cu is likely migrating to the surface due to its lower surface energy compared to Ni, resulting in a Cu-enriched Ni-Cu alloy surface [54]. This surface enrichment may lead to a decrease in Ni sites on the surface that are active for DRM, thus limiting the catalytic activity. Low amounts of Cu dopant, on the other hand, fail to improve the stability of the catalyst. This is likely due to the sintering of the Ni as a result of an insufficient amount of Cu that is needed for crystallite stabilization via alloy formation. These results indicate a synergistic effect between the Ni and Cu, and therefore, Ni/Cu atomic ratio plays a critical component when formulating the catalyst.

4.1.6. Catalyst Stability Test

To compare longer TOS changes in the catalytic activity of the monometallic and 'medium Cu' bimetallic Ni_8Cu_1/Al_2O_3-IWI catalysts, DRM was performed for 70h at 650 °C. The rates of CH_4 and CO_2 consumption are presented in Figure 7(a) and (b), while Figure 7(c) compares the syngas ratio of H_2/CO. Significant deactivation is observed on monometallic Ni/Al_2O_3-IWI, with a linear decrease in the CH_4 and CO_2 conversion rates and H_2/CO ratio; as discussed previously, this may likely be due to coke deposition and sintering of the Ni metal particles. After 70h of DRM reaction, the CH_4 conversion rate decreased from an initial 0.12 to 0.012 mol/min/g_{Ni} while the CO_2 conversion rate decreased from 0.14 to 0.02 mol/min/g_{Ni}.

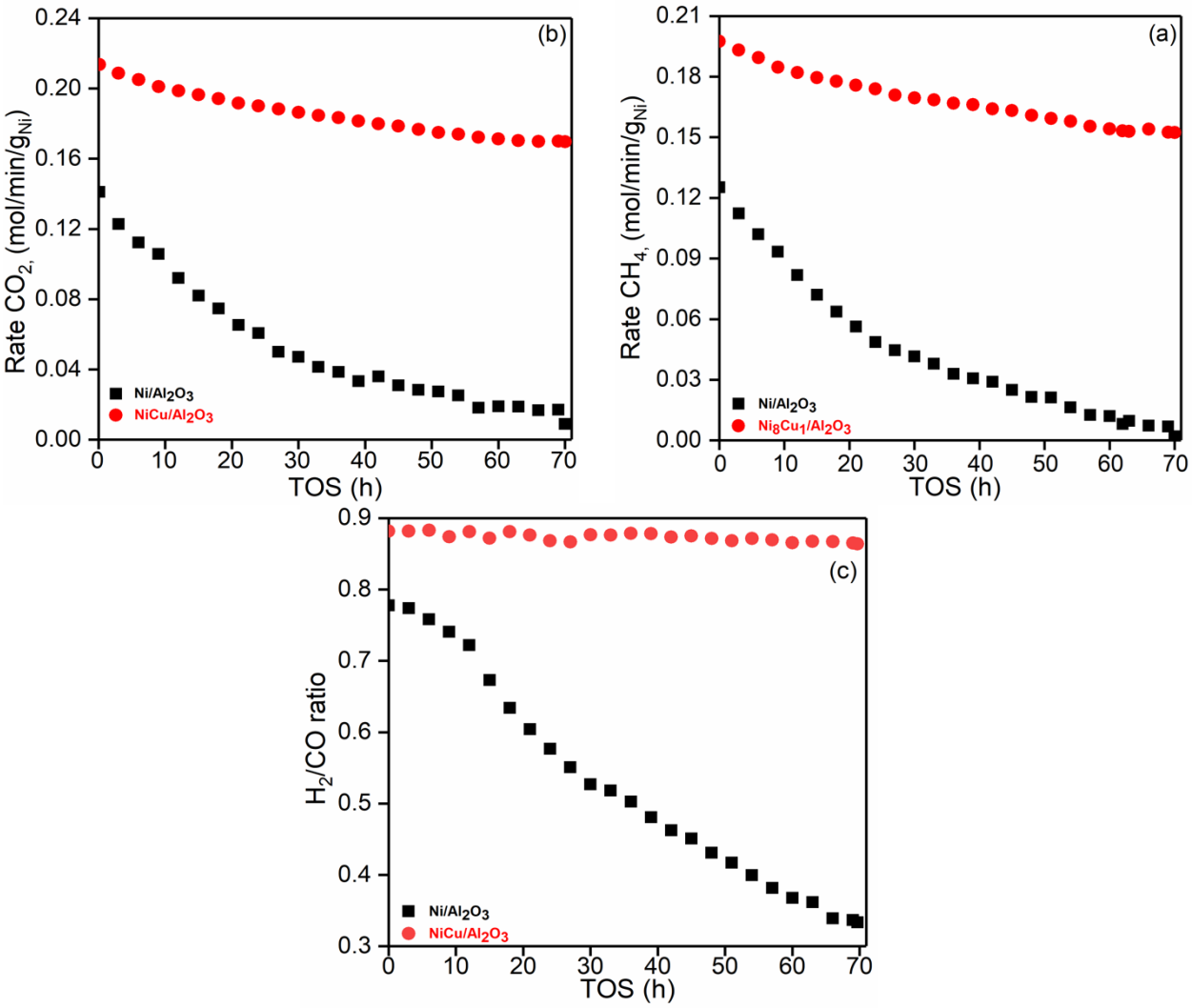

Figure 8: (a) CH_4, (b) CO_2 conversion rates, and (b) H_2/CO ratio versus TOS for CO_2 reforming of methane at 650 °C and 70h TOS. (The DRM activity data was collected by a Cirrus 2 Mass spectrometer (MKS Instruments)

In contrast, the bimetallic Ni_8Cu_1/Al_2O_3 catalyst showed improved activity during the 70h of TOS, with CH_4 and CO_2 conversion rates decreasing slightly from 0.20 to 0.16 mol/min/g_{Ni}, and 0.21 to 0.17 mol/min/g_{Ni}, respectively. Possible reasons for the excellent stability of this Ni_8Cu_1/Al_2O_3 catalyst have been discussed in the previous section. In general, it is attributable to the smaller particle size and the formation of a Ni-Cu alloy that retards both active metal sintering and carbon formation. Interestingly, the H_2/CO ratio is nearly constant over 70 hours DRM despite the decline in CH_4 and CO_2 conversion rates; this demonstrates the ability of the bimetallic catalyst

to suppress undesired side reactions like the Reverse-Water-Gas-Shift (RWGS) and the Boudard reaction. In addition, carbon deposition and removal through gasification is easier on this catalyst, producing this very stable H_2/CO ratio.

4.1.7. Effect of Ni-Cu Alloy Formation on Suppressing Coke

To investigate the effect of Cu on coke formation, the spent catalysts after 10h and 70 h DRM at 650 °C were characterized by PXRD, O_2-TPO, TEM, SEM, and TGA-DSC.

4.1.7.1. Powder XRD Analysis

From the X-Ray diffractograms of the spent Ni and 'medium Cu' Ni_8Cu_1-IWI catalysts (Figure 9), an additional diffraction peak was observed at $2\theta = 26.6°$ for both catalysts, along with the expected reflections. This reflection was assigned to graphitic carbon, accumulated on the surface of the spent catalyst [42]. On comparing the peak intensities, it is evident that Ni/Al_2O_3-IWI catalyst deactivated faster because of a higher degree of coking than the Ni-Cu catalyst, indicating that the bimetallic Ni_8Cu_1/Al_2O_3-IWI catalyst exhibits better coke resistance than its monometallic counterpart. No attempt was made to measure crystallite size via the Scherrer equation due to a lower signal: noise ratio of the PXRD pattern. Another important observation is that the shape of the characteristic Ni-Cu alloy peak at $2\theta = 44.4°$ remains largely intact, indicating that the Ni-Cu alloy formed is structurally stable.

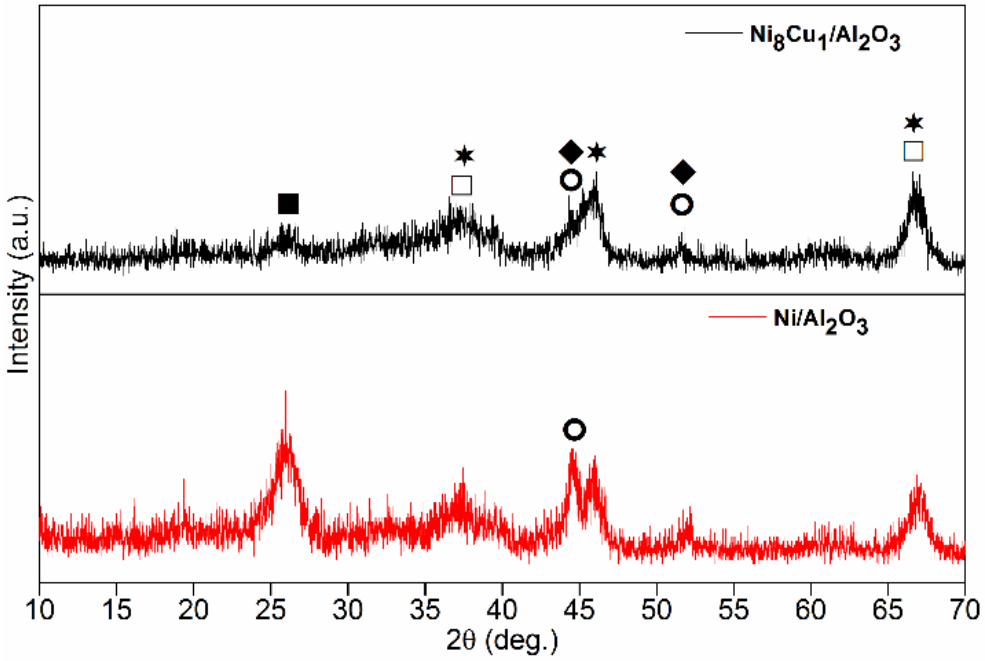

Figure 9: XRD patterns of spent (a) Ni/Al_2O_3 and (b) Ni_8Cu_1/Al_2O_3 catalysts after DRM performance at 650 °C for 10h TOS. (■-graphitic carbon, *: γ-Al_2O_3, ○: Ni0, ◆: Ni-Cu alloy, □: $NiAl_2O_4$)

4.1.7.2. O_2-TPO Analysis Over Coked-Catalysts

To understand the differences in the nature of carbon formed on the mono and bimetallic catalysts, O_2-TPO was performed over the used catalysts after 70h DRM (Figure 11). The TPO profiles of the catalysts run for 10h TOS are given in Figure 10. In Figure 11, the presence of a predominantly graphitic-type of carbon is observed on the monometallic Ni catalyst as evidenced from the intense CO_2 peak at 650 °C, produced as a result of the oxidation of deposited coke. Especially in reforming, graphitic forms of deposited carbon typically encapsulate the active metal site, thus deactivating the Ni [55]. In the bimetallic catalysts, the TPO curve peaks at a much lower 590 °C, due to the lower energy required for oxidation. This indicated that the type of carbon formed in the bimetallic catalyst is predominantly amorphous (filamentous/polymeric) and is highly reactive.

Furthermore, the amount of coke accumulated in the spent Ni_8Cu_1/Al_2O_3-IWI is notably lesser than in the spent Ni/Al_2O_3-IWI, as inferred from the areas under the TPO curves. The coking rate for the monometallic catalyst is 1.19E-03 mg C/h/g_{cat}, much higher than for the bimetallic catalyst at 4.21E-04 mg C/h/g_{cat}. This indicates that Cu plays a vital role in effectively minimizing coke formation. These results agree well with the XRD analysis of the spent catalysts.

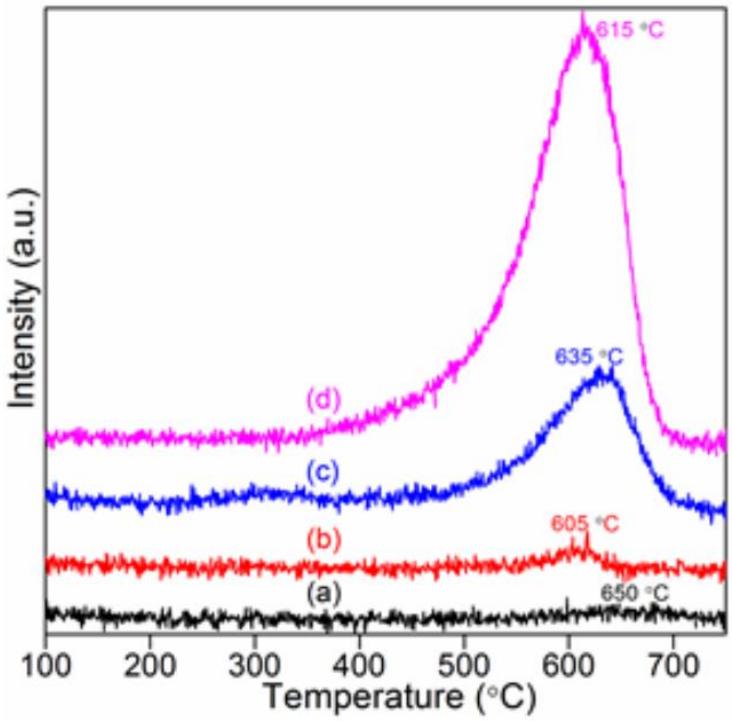

Figure 10:O_2-TPO profile of spent a) Ni_8Cu_1/Al_2O_3, b) $Ni_{10}Cu_1/Al_2O_3$, c) Ni_3Cu_1/Al_2O_3, and d) Ni/Al_2O_3 catalysts after 10h DRM at 650 °C

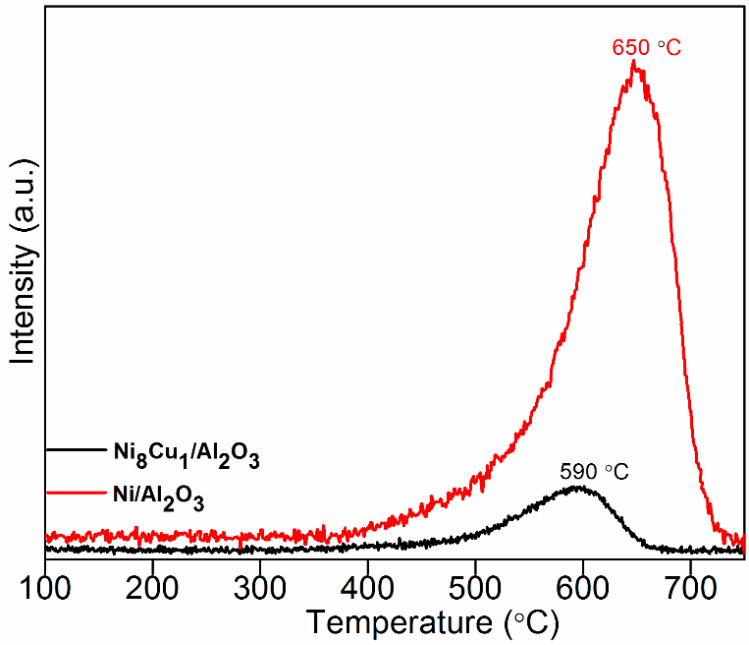

Figure 11: O_2-TPO profile of spent catalysts after DRM performance at 650 °C for 70h TOS.

4.1.7.3. TEM and SEM Analysis

To further investigate the morphology and the nature of carbon formed on the used catalysts, TEM analysis was performed on monometallic Ni/Al_2O_3-IWI and 'medium Cu' bimetallic Ni_8Cu_1/Al_2O_3-IWI catalysts after 10h DRM reaction (Figure 12 and Figure 13). Various forms of carbon are seen deposited on the surface of the Ni/Al_2O_3-IWI catalyst (Figure 12(a, b)): multi-walled carbon nanotubes, nano-onions, and other filamentous structures. Of the nanotubes formed, some of them had Ni particles at the tip or embedded within the closed-end tube, while the others lacked any apparent Ni crystallite. Carbon nanotubes keep growing from the Ni surface, resulting in the degradation of the active structure, eventually leading to the catalyst's total deactivation [56]. While CNTs do not immediately lead to catalyst deactivation, graphitic forms of carbon cause rapid deactivation by encapsulating active sites. A representative HR-TEM image in Figure 12(c) clearly shows a Ni particle entrapped in the encapsulating carbon onion. High-angle annular dark-field scanning transmission electron microscopy (HAADF-STEM) image

(Figure 12 (d)) further highlight Ni particles, identified as bright spots, trapped either within graphitic carbon nano-onions or in CNTs.

Calculating the average Ni particle size from TEM indicates that the Ni size was primarily left intact, with only a slight increase from 9 to 9.4 nm. It has been reported that the primary reason for the deactivation of a Ni/Al_2O_3-IWI catalyst is carbon deposition during DRM on the catalyst surface [55].

Scanning-transmission electron microscope high-angle annular dark-field (STEM-HAADF) images of Ni, Al, and C are shown in (Figure 12(e-g)). These images present how carbon deposition detaches Ni particles from the support either via CNT growth or via graphitic carbon encapsulation. The overlaid EDS images of Ni, Al, and C are shown in Figure 12(h).

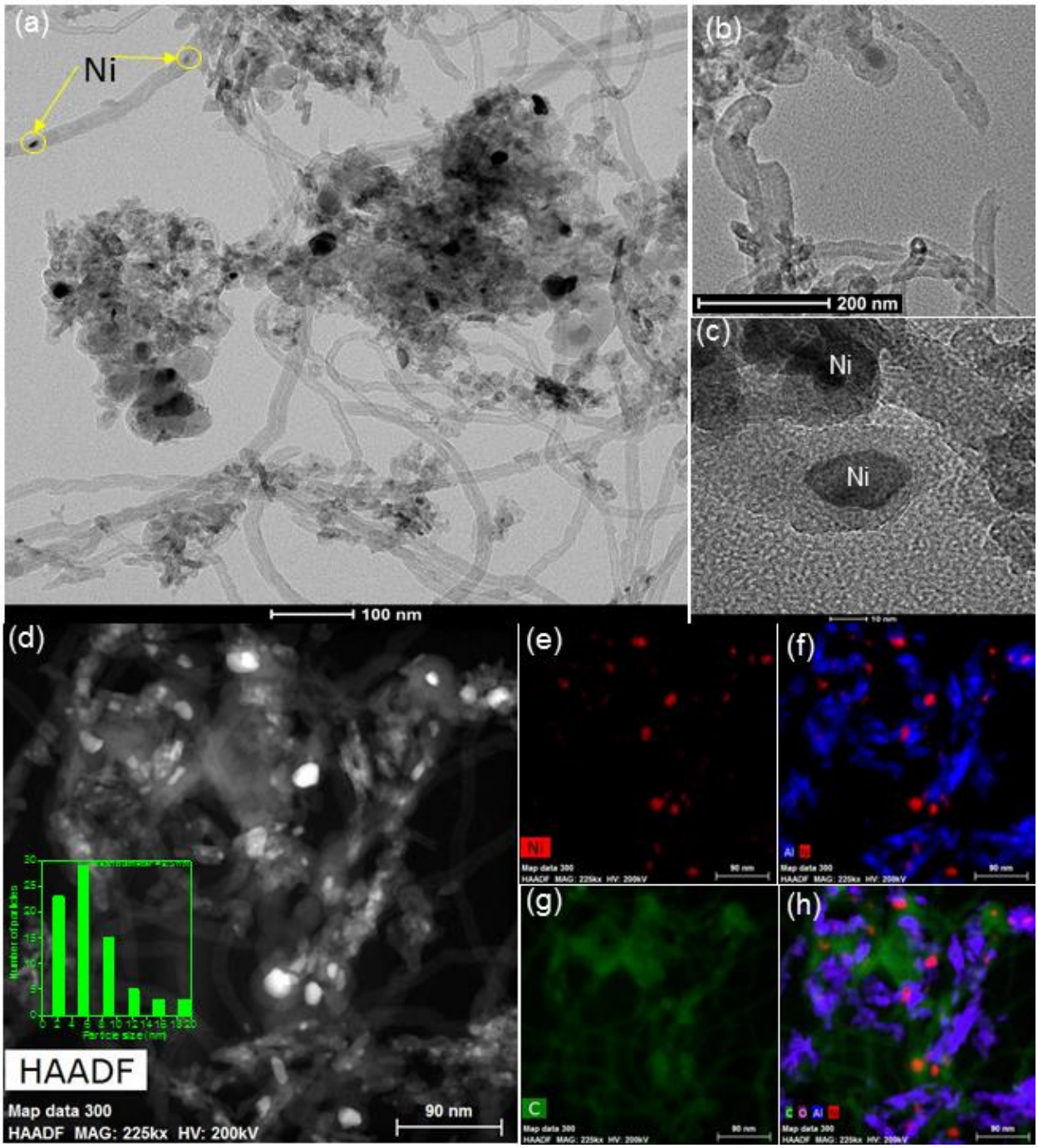

Figure 12: (a) TEM, (b-C) HRTEM, (d) High-angle annular dark-field scanning transmission electron microscopy (HAADF-STEM), and (e-h) Elemental mapping of spent Ni/Al_2O_3-IWI catalyst. (Inset: Ni metal particle size distribution).

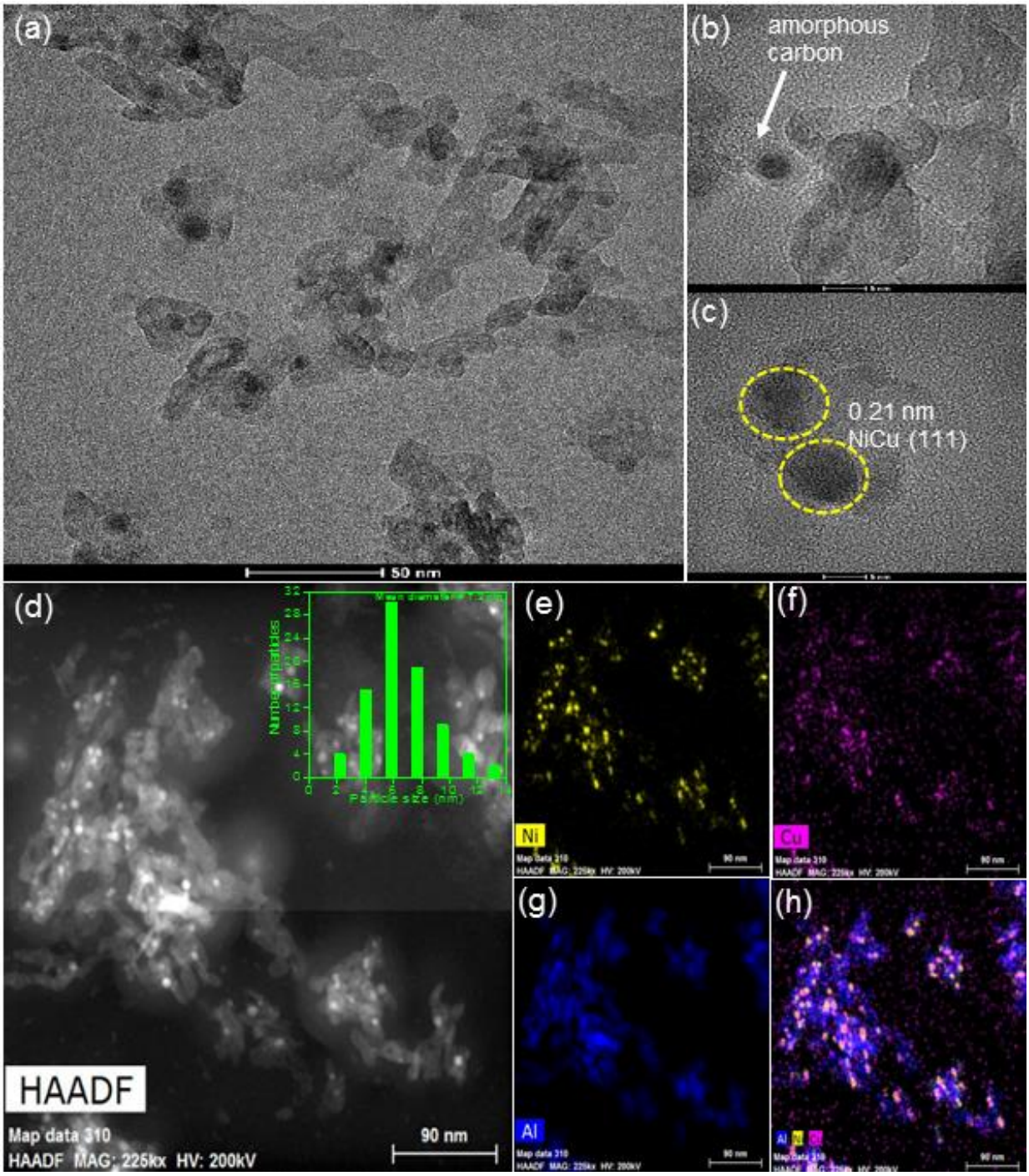

Figure 13: (a)TEM, (b-c) HRTEM, b) High-angle annular dark-field scanning transmission electron microscopy (HAADF-STEM), and (e-h) Elemental mapping of spent Ni_8Cu_1/Al_2O_3-IWI catalyst. (Inset: Ni metal particle size distribution).

Figure 13(a) shows a representative TEM image of 'medium Cu' bimetallic Ni_8Cu_1/Al_2O_3-IWI catalyst. Interestingly, except for some amorphous carbon, neither CNTs nor encapsulating graphitic carbon forms were observed on the bi-metallic catalyst even after 10h of DRM reaction. It is likely that the carbon, initially deposited on the bimetallic surface, is active and readily oxidized by CO_2 via a lower energy pathway [57]. The carbon thus formed is expected to be amorphous, minimizing the formation of structured graphitic carbon, which can deactivate the catalyst. The HR-TEM images (Figure 13(b-c)) also validate the homogeneous, alloy nature of the dispersed Ni-Cu NPs. A lattice fringe spacing of 0.21 is measured for the active particle, consistent with (111) planes of Ni-Cu alloys [27]. After 10h of DRM reaction, this inter-fringe distance remains the same (Figure 13(c)), indicating that the Ni-Cu alloy is intact and plays a critical role in suppressing the coke formation, specifically the formation of graphene-like layers that eventually lead to CNTs and encapsulating carbon nano-onions [58]. Scanning-transmission electron microscope high-angle annular dark-field (STEM-HAADF) image of the used Ni_8Cu_1/Al_2O_3-IWI (Figure 13(d)) reveals particles in the range of 2 to 14 nm (mean - 7.2 nm), indicating that the Ni particle grew from 4 to 7.2 nm after DRM reaction. These results strongly suggest particle sintering as the primary contributor to deactivation, as opposed to significant carbon deposition in the mono-metallic Ni catalyst. Scanning-transmission electron microscope high-angle annular dark-field (STEM-HAADF) image of Cu and Ni and the overlaid image (Figure 13e-h)) reveal that the Cu and Ni atoms comprising the active nanoparticles were homogeneously dispersed and supports the formation of the Ni-Cu alloy phase. These results strongly suggest that the Ni-Cu alloy nanoparticles were formed with high phase purities, which is consistent with the XRD results. The overlaid Scanning-transmission electron microscope high-angle annular dark-field (STEM-HAADF) images of Ni and Cu (Figure 13(h)) coincide well with each other, further

confirming the retention of the Ni-Cu alloyed phase even after the DRM reaction. Scanning Electron Microscopy analysis has been performed over the fresh (Figure 14) and deactivated catalysts (Figure 15). Both the supported monometallic and bimetallic fresh, calcined catalysts exhibit similar morphological features and as such were indistinguishable from each other. However, after 70h TOS activity and durability test at 650 °C, there are obvious differences in the morphologies in the used catalysts. Figure 15(a) shows the SEM images of used monometallic Ni/Al_2O_3-IWI catalyst, exhibiting a large amount of coke deposition in the form of carbon nanofibers/CNTs. The CNTs in combination with graphitic carbon (not seen in the figure) produce catalyst deactivation with time on stream via gradual encapsulation of the Ni active sites, and pore–blockage. These forms of carbon require higher temperatures to be oxidized as evidenced from O_2-TPO, implying they are more recalcitrant, and therefore cause faster deactivation. On the other hand, the SEM micrograph of the bimetallic Ni_8Cu_1/Al_2O_3-IWI catalyst (Figure 15(b)) indicates that coverage of the catalyst by carbon has occurred to a much lesser extent. On the surface is what appears to be a more amorphous type of carbon, which is more reactive and can be eliminated readily. These findings correlate well with the conclusions drawn from XRD and O_2-TPO analysis.

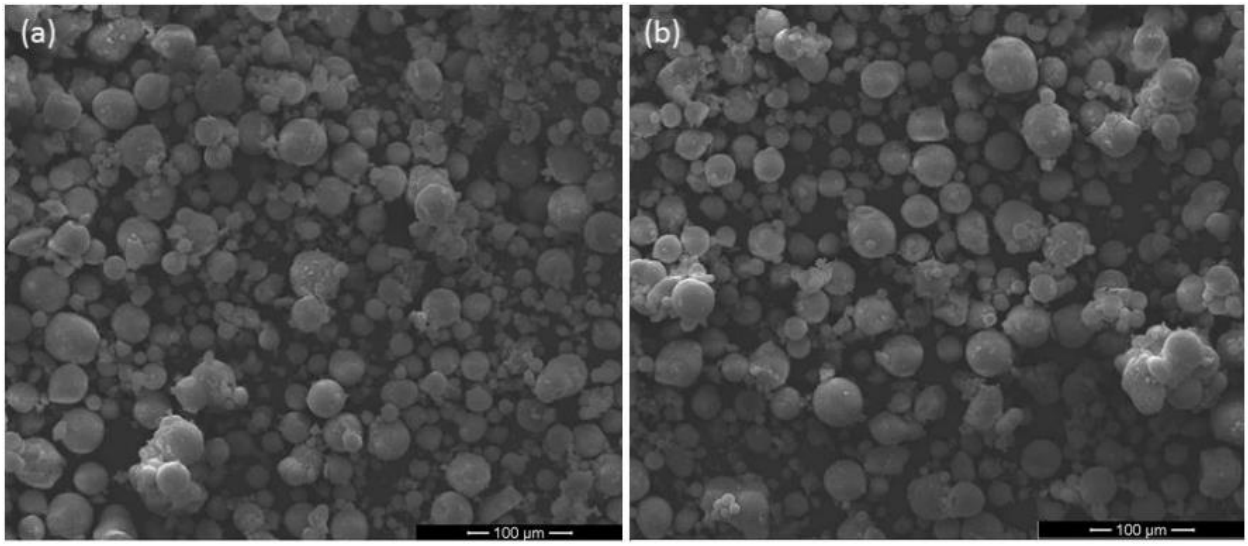

Figure 14: SEM images of fresh calcined a) Ni/Al_2O_3 and b) Ni_8Cu_1/Al_2O_3 catalysts.

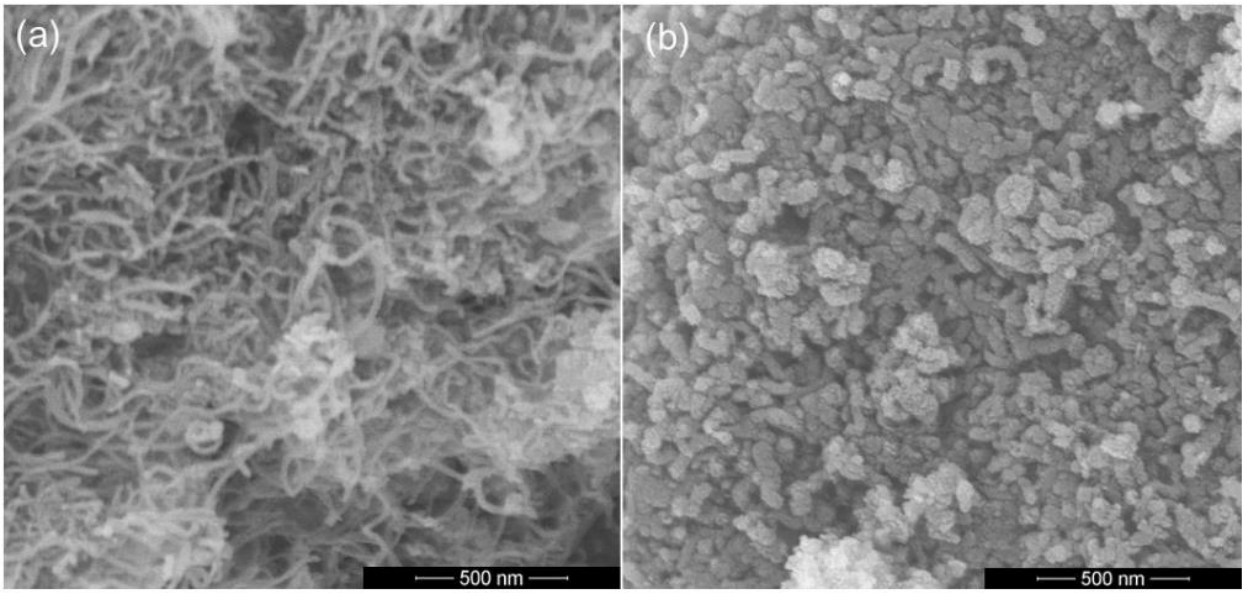

Figure 15: SEM images of spent (a) Ni/Al_2O_3 and (b) Ni_8Cu_1/Al_2O_3 catalysts after DRM performance at 650 °C for 70h TOS

4.1.7.4. TGA-DSC Analysis of Spent Catalyst

To quantify the coke formed on the used catalysts and obtain further information on the nature of carbon itself, Thermo-Gravimetric Analysis (TGA) coupled with Differential Scanning Calorimetry (DSC) was performed. Figure 16(a) displays the TG profiles of the used monometallic Ni/Al_2O_3-IWI and bimetallic Ni_8Cu_1/Al_2O_3-IWI catalysts after 10h of DRM at 650 °C. As

discussed previously, the temperature required for oxidation corresponds to the type of carbon species involved. DSC provides this information in terms of heat flow per gram sample as a function of temperature (W/g°C, see Figure 16(b)).

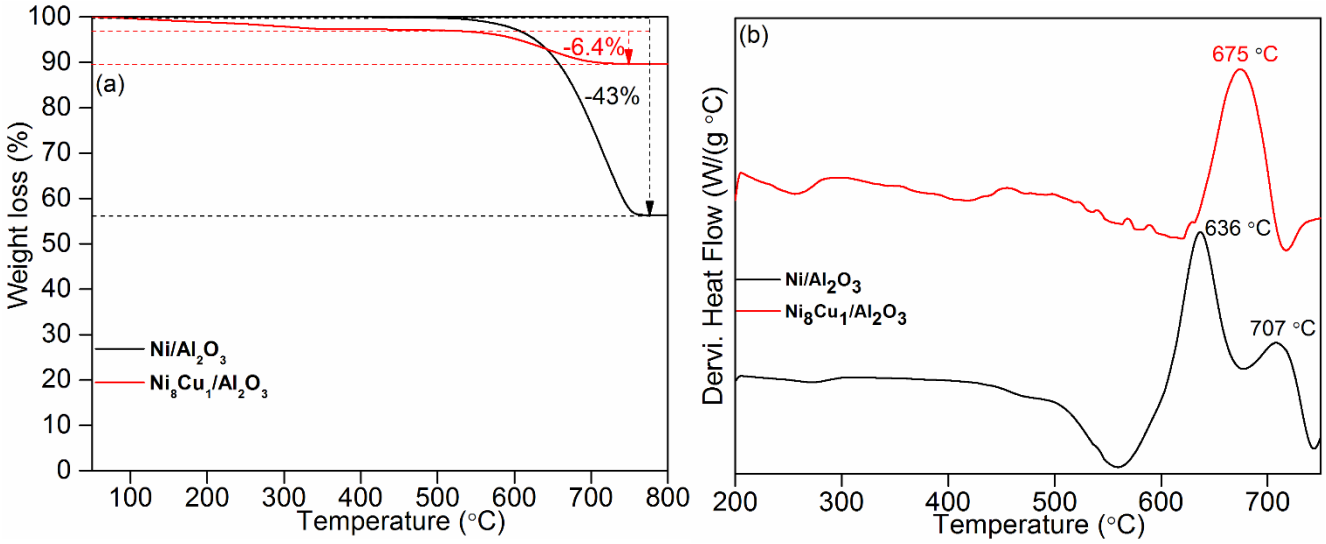

Figure 16: (a) TGA and (b) DSC profiles of spent Ni/Al_2O_3 and Ni_8Cu_1/Al_2O_3 catalysts after DRM performance at 650 °C.

Based on the literature, the carbon forms may be classified in terms of oxidation temperature as (a) highly reactive activated carbon species that oxidize at low temperatures (<350 °C); (b) the amorphous carbon and carbon nano-filaments/fibers/CNTs that oxidize between 350-550 °C; and (c) non-reactive graphitic carbon species that oxidize at higher temperatures of >650 °C [59,60]. As depicted in Figure 16(a), the monometallic Ni/Al_2O_3-IWI catalyst shows a significant weight loss (43%) in the range of 550-700 °C, probably due to oxidation of both filamentous and non-reactive graphitic carbon, which severely degrade catalyst performance. In contrast, the bimetallic Ni_8Cu_1/Al_2O_3-IWI catalysts display a much lower weight loss of 6.4%, suggesting that the quantity of filamentous and graphitic carbon formed is minimal in agreement with XRD, O_2-TPO results. It has been demonstrated that a catalyst with smaller metal particles and higher dispersion typically possesses stronger metal-support interactions, which minimizes coke deposition. These results are consistent with the SEM images shown in Figure 15.

Figure 16(b) presents the DSC profiles of the used Ni/Al_2O_3-IWI and Ni_8Cu_1/Al_2O_3-IWI catalyst after 10h of DRM reaction. Contrary to its TPO profile, the monometallic Ni/Al_2O_3-IWI displays two exotherm peaks - one at 636 °C and the other at 707 °C, indicating that at least two types of carbon species were formed. The stronger exotherm at 636 °C may be assigned to the oxidation of filamentous carbon, and the peak at the higher 706 °C might be due to oxidation of graphitic carbon [55,57,61]. This temperature range overlaps relatively well with that observed in the TGA analysis. The bimetallic Ni_8Cu_1/Al_2O_3-IWI catalyst, on the other hand, has a single exothermic peak at an intermediate temperature of 675 °C, likely corresponding to the oxidation of a combination of amorphous and filamentous carbon. These results are in good agreement with the SEM and O_2-TPO analysis.

By this point, it is quite apparent that the bimetallic Ni_8Cu_1/Al_2O_3-IWI catalyst is relatively more stable than its mono-metallic counterpart, able to impede coke deposition significantly via the addition of a small amount of Cu.

The experimental results presented are in good agreement with the results of DFT studies published by our group [1]. The ab initio DFT studies investigated the effect of Cu content on active Ni sites in terms of affinity for coke formation, energy profile for CH_4 dehydrogenation, activation barriers for C formation via the CH dissociation pathway, and C elimination by oxidation with O to form CO. The study reported that as Cu content on Ni surfaces increases, its affinity to coke formation decreases. However, at a certain point, Cu content is so high that it renders the progression of the DRM reaction thermodynamically unfavorable and impedes its long TOS stability. On the other hand, ‘medium Cu’ loading on the Ni surface showed the best trade-off as it reduces the total amount of carbon that can be deposited while allowing the reaction to proceed.

4.2. Section II: Investigation of Synthesis Technique Impact

The catalysts investigated in this section are prepared by the sol-gel and the co-precipitation techniques. The catalysts in this section are Ni/Al_2O_3-SG, Ni/Al_2O_3-CP, Ni_8Cu_1/Al_2O_3-SG, Ni_8Cu_1/Al_2O_3-CP. It is important to note that the optimized copper loading obtained from the first sub-section was used to synthesize the bimetallic SG and CP catalysts. The findings from characterizing several fresh catalyst properties using advanced techniques will be presented. The implemented techniques are H_2-TPR, XRD, Chemisorption, XPS, SEM, TEM, and EDS. Then, the results of short time on stream (TOS) DRM performance tests will be presented and analyzed for all synthesized catalysts. Next, the long TOS DRM performance results of both monometallic and bimetallic CP catalysts are discussed. Finally, the analysis of the used catalysts from these long TOS tests using XRD, XPS, TGA, DSC, SEM, TEM, and EDS are presented and discussed.

4.2.1. H_2-Temperature Programmed Reduction

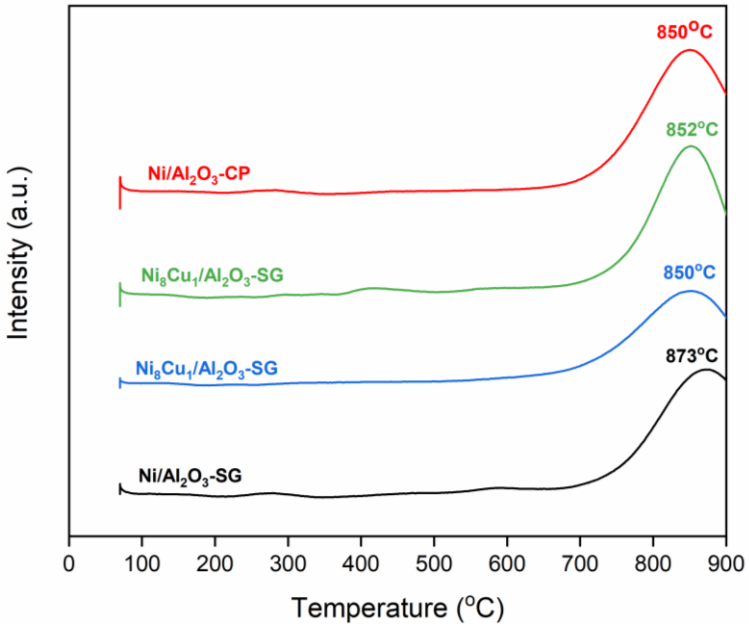

Figure 17: H_2-TPR profiles of fresh calcined catalyst samples

The H_2-TPR profiles for catalysts synthesized by sol-gel and coprecipitation are presented in Figure 17. None of the profiles exhibit peaks below 500 °C, signifying the absence of weakly

interacting bulk NiO species [62]. All profiles show a single reduction peak between 850-873 °C. Peaks at this temperature correspond to the presence of strongly interacting NiO and $NiAl_2O_4$ species [63]. Interestingly, there is an evident absence of the CuO phase in all catalyst TPR profiles. This might signify the complete incorporation of Cu^{2+} into the NiO framework via NiCu alloy formation [40,41]. The similar reduction peak observed in all profiles indicates that the metal-support and metal-metal interaction strength is nearly identical. It is important to note that the temperature for all experiments was held constant at 900 °C. This allowed the reduction peaks displayed in Figure 17 to complete. This data was not shown to maintain the clarity of the graphs.

4.2.2. XRD analysis of calcined and reduced catalyst samples

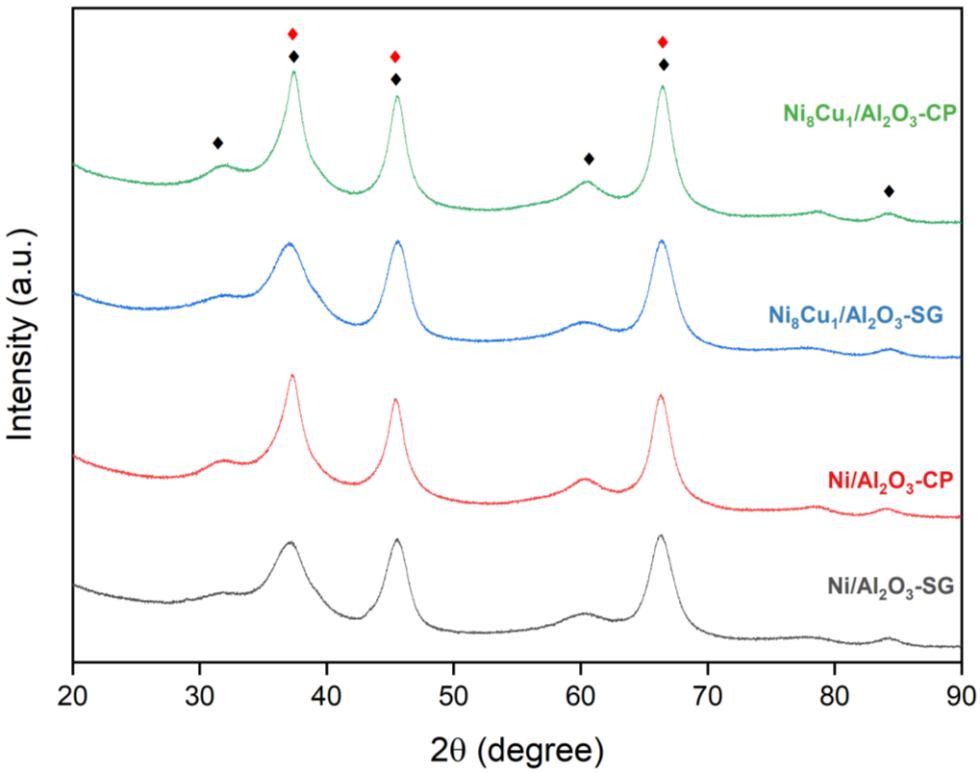

Figure 18: PXRD of Calcined SG and CP Catalysts (♦: γ-Al_2O_3, ♦: $NiAl_2O_4$)

The PXRD graphs for all calcined SG and CP catalysts are presented in Figure 18. All graphs show identical peak positions at 31.8°,37.2°,45.5°,60.2°,66.6°, and 84.3°. These peaks can

be attributed to γ-Al_2O_3 and $NiAl_2O_4$ [43,44]. Interestingly, no peaks associated with NiO can be observed in any of the synthesized catalysts. This finding agrees with H_2-TPR results, which confirms the absence of this phase [64]. This could signify that nickel is adequately dispersed on the support. CuO, Cu_2O, and other Cu-related crystalline phases were not detected. This might indicate that these phases are either amorphous or their size is smaller than the detection limit of XRD.

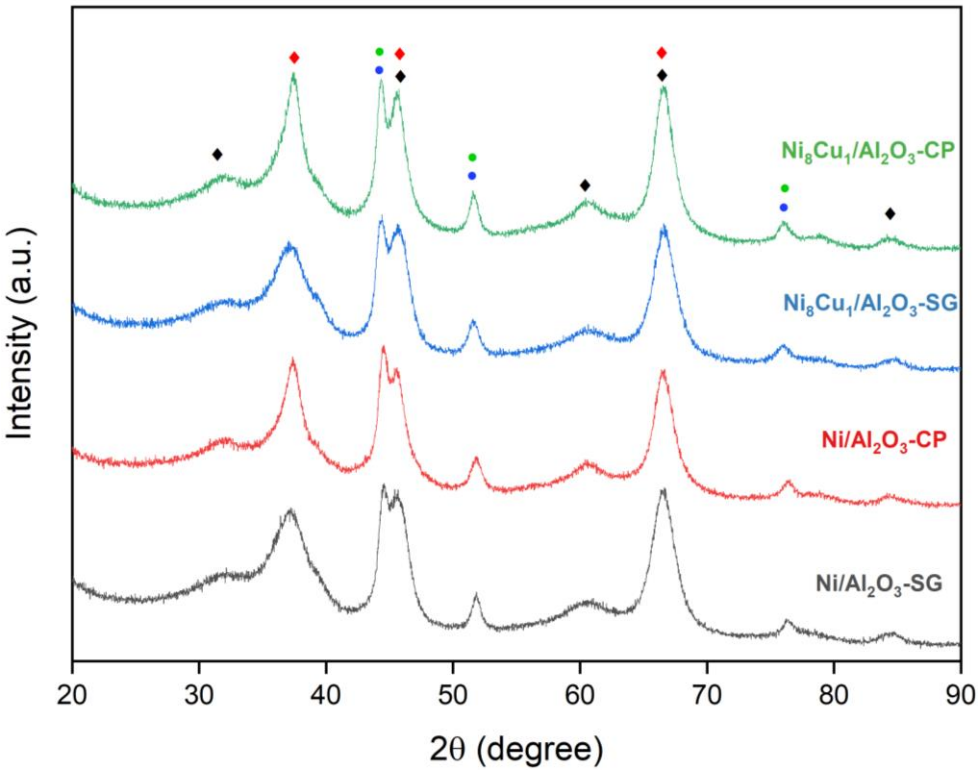

Figure 19: PXRD of Reduced SG and CP Catalysts (♦: γ-Al_2O_3, ♦: $NiAl_2O_4$, ●: Ni^0, ●: Ni-Cu alloy)

The PXRD graphs for all reduced SG and CP catalysts are presented in Figure 19. Upon reduction, there is a clear difference in the observed graphs. FCC Ni and Ni-Cu alloy peaks are visible at 44.4°, 51.7°, and 76.1°[43,44]. The intensity and sharpness of these peaks are near identical in all samples. This might indicate that the active sites in these catalysts are very similar. The γ-Al_2O_3 and $NiAl_2O_4$ peaks observed in calcined catalysts remain present after reduction. No

peaks associated with Cu^0 are observed. This could result from the detection limit of XRD or the potentially amorphous structure of the formed Cu^0.

4.2.3. H_2-Chemisorption of Reduced Catalysts

The results of H_2 chemisorption in the reduced catalysts are summarized in Table 4. The metal dispersion is calculated based on the moles of H_2 consumed to saturate the surface. The monometallic SG catalyst presented the highest metal dispersion (8.07%) and metal surface area (5.37 m^2/g Sample). In comparison, the monometallic CP catalyst showed a lower metal dispersion (4.37%) and metal surface area (2.91%). These results could indicate the monometallic SG catalyst active sites are better dispersed due to the difference in the chemistry of the used preparation techniques.

When studying the bimetallic catalysts, both show lower metal dispersion and metal surface area compared to the monometallic versions. The bimetallic SG catalyst had a metal dispersion of (3.18%) and a metal surface area of (2.11 m^2/g Sample). On the other hand, the bimetallic CP catalyst presented a slightly higher metal dispersion (3.45%) and metal surface area (2.3 m^2/g Sample).

The difference in results between monometallic and bimetallic catalysts could be caused by the weak chemisorption of hydrogen on copper. This weak chemisorption in return could yield underestimations of the metal dispersion.

Table 4: H_2 chemisorption results for reduced catalysts

	Metal Dispersion (%)	Metal Surface Area (m^2/g Sample)
$Ni/\gamma\text{-}Al_2O_3\text{-}SG$	8.07	5.37
$Ni_8Cu_1/\gamma\text{-}Al_2O_3\text{-}SG$	3.18	2.11
$Ni/\gamma\text{-}Al_2O_3\text{-}CP$	4.37	2.91
$Ni_8Cu_1/\gamma\text{-}Al_2O_3\text{-}CP$	3.45	2.30

4.2.4. X-ray photoelectron spectroscopy of reduced catalysts

XPS analysis was conducted for the catalyst samples after reduction at 650 °C. Table 5 presents the atomic percentages of elements observed in the reduced catalyst samples. The percentages were normalized after deducting background carbon originating from the tape used to place the samples into the instrument. Studying the monometallic samples, the atomic percentage of Nickel on the surface is very close. The SG sample had a 1.32 at. % of nickel on the surface, whereas the CP sample has a slightly higher value of 1.41 at. %. Based on the observed results, the preparation technique did not have an impact on surface nickel composition. Shifting the focus to the bimetallic samples, the same behavior is observed. Comparing the nickel at.% for the bimetallic samples, the values are almost identical. The SG catalyst had 1.42 at.% of nickel on its surface, practically similar to the 1.41 at.% surface nickel composition of the CP catalyst. These values are only slightly higher than those observed for the monometallic samples. As for copper, the values observed are very similar as well. The SG bimetallic catalyst had 0.37 at.% of copper on its surface, whereas the CP catalyst had a somewhat lower value of 0.29 at.% for copper. Again, the obtained results do not indicate that the preparation technique leads to drastic differences in surface composition for bimetallic catalysts.

Table 5: Atomic percentages for elements observed in XPS analysis of reduced catalysts

	Ni (Atomic %)	Cu (Atomic %)	Al (Atomic %)	O (Atomic %)
$Ni/\gamma\text{-}Al_2O_3\text{-}SG$	1.32	-	34.69	64.00
$Ni_8Cu_1/\gamma\text{-}Al_2O_3\text{-}SG$	1.42	0.37	33.95	64.25
$Ni/\gamma\text{-}Al_2O_3\text{-}CP$	1.16	-	35.62	63.22
$Ni_8Cu_1/\gamma\text{-}Al_2O_3\text{-}CP$	1.41	0.29	32.98	65.32

To study the chemical states of the elements present in the synthesized catalysts, HR-XPS was conducted. The obtained nickel spectra were deconvoluted and fitted. The graphs of the deconvoluted nickel plots are presented in Figure 20, and the observed peak positions are

summarized in Table 6. It is important to note that deconvolution was performed while keeping in mind that peak width greater than 1 eV would signify the presence of multiple elements.

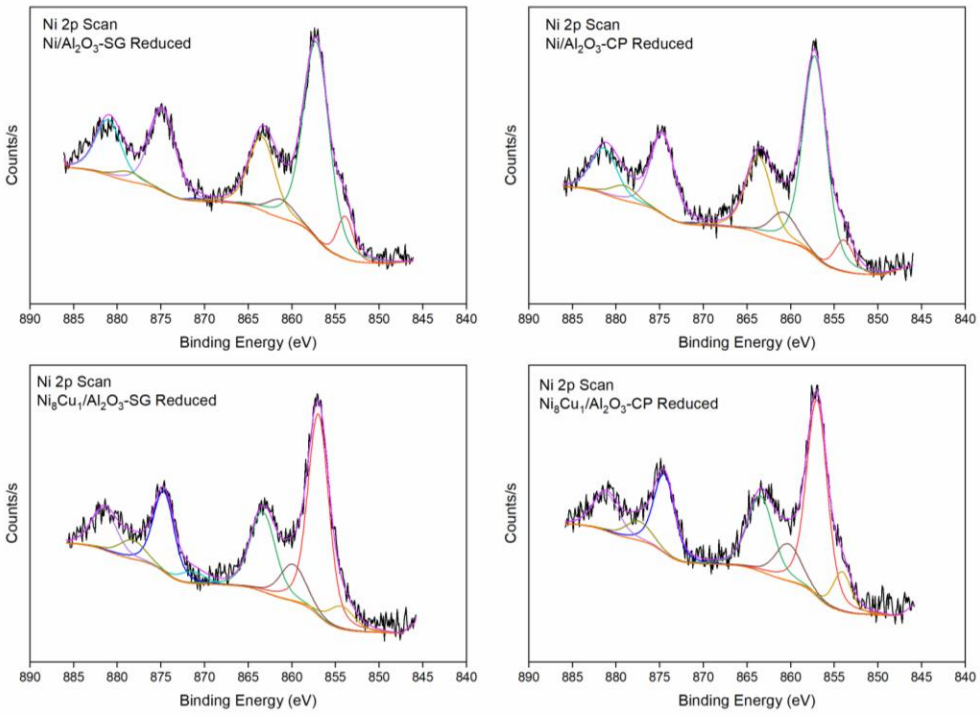

Figure 20: Deconvoluted nickel XPS spectra of reduced catalysts

Table 6: Binding energies of peaks observed in deconvoluted graphs of reduced catalyst nickel XPS spectra

Binding Energy (ev)	$Ni^0_{3/2}$	Ni $2p_{3/2}$	Satellite 1	Satellite 2	$Ni^0_{1/2}$	Ni $2p_{1/2}$	Satellite 3	Satellite 4
Ni/γ-Al_2O_3-SG	853.8	857.2	861.1	863.4	870.9	874.8	878.7	881.0
Ni_8Cu_1/γ-Al_2O_3-SG	854.3	856.9	859.2	863.3	871.4	874.6	878.2	881.5
Ni/γ-Al_2O_3-CP	853.8	857.2	860.8	863.6	870.9	874.6	879.0	881.3
Ni_8Cu_1/γ-Al_2O_3-CP	854.0	856.9	860.2	863.4	871.2	874.5	877.4	881.1

The deconvoluted graphs of Figure 20 show that the number of nickel peaks observed in all catalysts is identical. The position of the lowest peak observed in all spectra resided between 853.8 and 854.3eV. These peaks were attributed to metallic nickel Ni^0 [65,66]. The second peak present was that of Ni $2p_{3/2}$ and was identified within 856.9eV and 857.2eV. These peaks could either be attributed to $NiAl_2O_4$ or NiO [67,68]. The near-identical peak positions for these species render differentiating between them very difficult. Based on XRD and TPR results, it was established that $NiAl_2O_4$ was the main species identified in the samples. Most probably, both

species are present and $NiAl_2O_4$ is more abundant. The satellite peaks observed in the spectra are expected, whereas the Ni $2p_{1/2}$ peaks observed are the shadows of the Ni $2p_{3/2}$ peaks and do not aid the analysis. The binding energy of each of the peaks can be effected by the strength of the interaction of the metal with either the support or other metals. Furthermore, in the case of bimetallic catalysts, the quantity of copper doped in the sample can induce a shift in the binding energy values. The two monometallic catalysts were found to have identical $Ni^0_{3/2}$ and Ni $2p_{3/2}$ binding energy values at 853.8 eV and 857.2 eV, respectively. This indicates that the species responsible for these peaks have the same characteristics and interaction strengths. When studying the bimetallic catalysts, certain differences can be observed in the binding energy values. The $Ni^0_{3/2}$ binding energy values for these catalysts are higher than their monometallic variants as the (854.3 eV for the bimetallic SG catalyst and 854.0 eV for the bimetallic CP catalyst). Naghash et al.[44] studied the influence of different copper percentages and reduction temperatures on the XPS spectra of Ni-Cu/Al_2O_3 catalysts. They have found that at a certain reduction temperature, copper segregation can potentially cause an increase in the binding energy of the $Ni^0_{3/2}$ peak. Therefore, the increase in the binding energy of the $Ni^0_{3/2}$ peak for the bimetallic samples could be due to copper segregation on the catalyst surface. It could also be hypothesized that the bimetallic SG catalyst experienced a greater degree of copper segregation since it presented the highest binding energy for the $Ni^0_{3/2}$ peak.

As for the Ni $2p_{3/2}$ peaks, the corresponding binding energies for the bimetallic catalyst were identical at 856.9 eV, lower than the value observed for both monometallic catalysts. Referring back to the study conducted by Naghash et al.[44], their research has shown that lower binding energies for nickel are connected to modifications in unfilled d-band electron holes arising from the charge transfer from the copper to adjacent nickel.

To further study the chemical species present, the O1s XPS spectra obtained from the reduced catalysts were deconvoluted. The deconvoluted plots are presented in Figure 21, and the respective peak positions are summarized in Table 7.

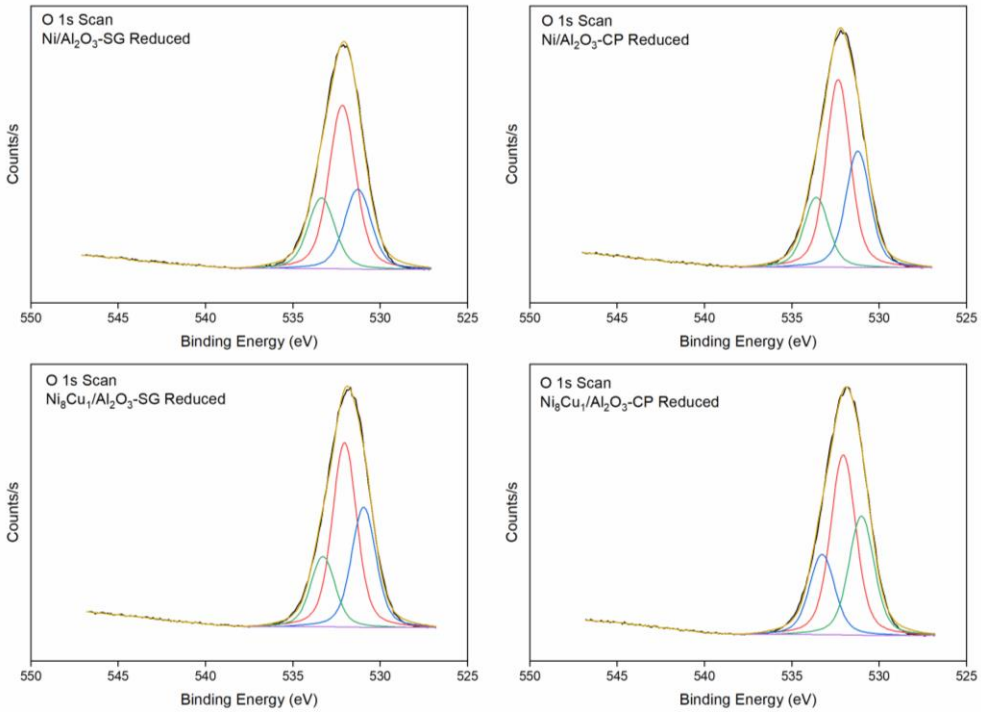

Figure 21: Deconvoluted oxygen XPS spectra of reduced catalysts

Table 7: Binding energies of peaks observed in deconvoluted graphs of reduced catalyst oxygen XPS spectra

Binding Energy (ev)	1st O1s peak	2nd O1s peak	3rd O1s peak
Ni/γ-Al_2O_3-SG	531.4	532.3	533.5
Ni_8Cu_1/γ-Al_2O_3-SG	531.0	532.1	533.1
Ni/γ-Al_2O_3-CP	531.3	532.5	533.7
Ni_8Cu_1/γ-Al_2O_3-CP	531.1	532.1	533.1

The plots observed in Figure 21 present 3 peaks, each at similar positions. The first peak observed in all plots resided between 531.0 and 531.4eV. These peaks can be assigned to $NiAl_2O_4$ [69,70]. The monometallic catalysts had very similar binding energies at this peak with a difference of 0.1 eV, which could result from minor differences in metal-support interaction strengths. The bimetallic catalyst, on the other hand, exhibited more prominent differences. The bimetallic SG catalyst presented binding energy of 531.0 eV, and a 531.1 eV binding energy for

the bimetallic CP catalyst was observed. The shift to lower binding energies for these catalysts could result from weaker metal-support interaction compared to that of the monometallic catalyst. As for the second peak observed in all graphs, it resided within a range of 532.1-532.5eV [71,72]. These peaks could be ascribed to Al_2O_3. The final peak observed in the plots was located between 533.1 and 533.7eV. This peak could not be identified as a phase expected to be present within any of the samples. The source of this peak might be a contaminant species. No peaks associated with NiO were identified. This could indicate that NiO is not present in an amount high enough to be identifiable as a separate phase. This finding is in good agreement with TPR data.

In addition, the Cu 2p XPS spectra obtained from the reduced catalysts were deconvoluted. The deconvoluted plots are presented in Figure 22, and the respective peak positions are summarized in Table 8.

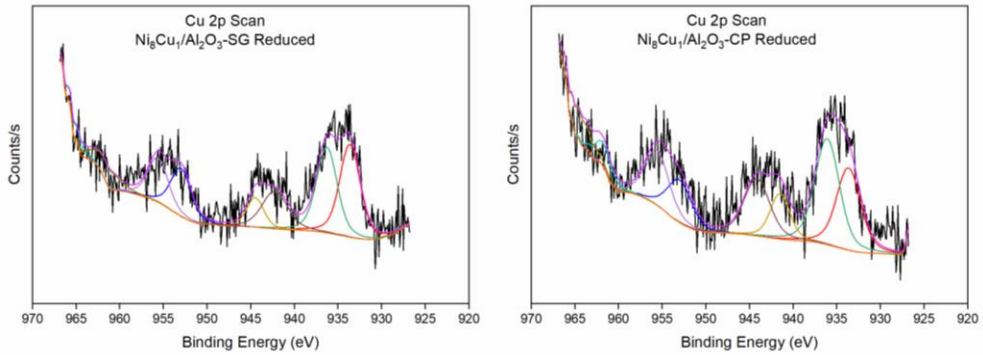

Figure 22: Deconvoluted copper XPS spectra of reduced catalysts

Table 8: Binding energies of peaks observed in deconvoluted graphs of reduced catalyst copper XPS spectra

Binding Energy (ev)	Cu $2p_{3/2}$	Cu $2p_{3/2}$	Satellite 1	Satellite 2	Cu $2p_{1/2}$	Cu $2p_{1/2}$	Satellite 3	Satellite 4
Ni_8Cu_1/γ-Al_2O_3-SG	933.6	936.3	944.4	942.2	952.9	955.6	961.5	965.2
Ni_8Cu_1/γ-Al_2O_3-CP	933.6	936.0	941.5	944.1	952.9	955.6	961.5	964.7

The deconvolution of the primary XPS spectra for the bimetallic catalysts gives rise to multiple peaks. The first main peak was split upon deconvolution into two separate peaks. The first of these peaks had an identical value for both bimetallic catalysts at 933.6 eV. This can be

ascribed to the Cu_2O phase (monovalent Cu^+) [73]. As for the second peak, it resided at 936.3 eV for the bimetallic SG catalyst and 936.0eV for the bimetallic CP catalyst. The phase attributed to this peak was CuO (Cu^{2+} state) [73]. Identifying these phases is a testament to the XPS technique's sensitivity as these phases were not identified by other methods such as XRD or TPR. The remaining satellite peaks and shadow Cu $2p_{1/2}$ peaks do not present any additional information.

4.2.5. Scanning Electron Microscopy of Reduced Catalysts

SEM analysis for the synthesized catalysts was conducted to study the samples' morphology and observe the dispersion of the active particles on the support surface. The SEM images obtained at different resolutions for the catalyst samples are presented in Figure 23 to Figure 26.

The particle morphologies observed for all catalysts seem very similar. The nickel particles are visible in all images as white particles well dispersed on the support surface. A clear distinction between the nickel particle dispersions and support morphology could not be established between the synthesized catalysts in the obtained images. One can set an initial hypothesis that the used SG and CP preparation techniques do not result in different morphologies in both monometallic and bimetallic variants of the catalysts.

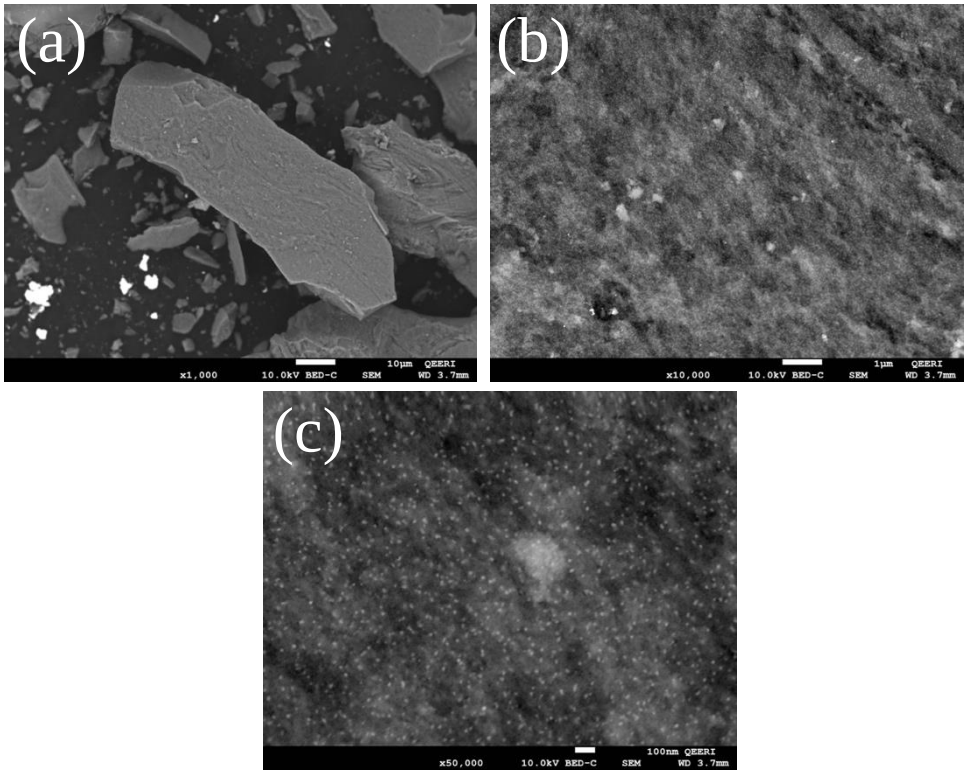

Figure 23: SEM images of reduced Ni/Al_2O_3 SG Catalyst

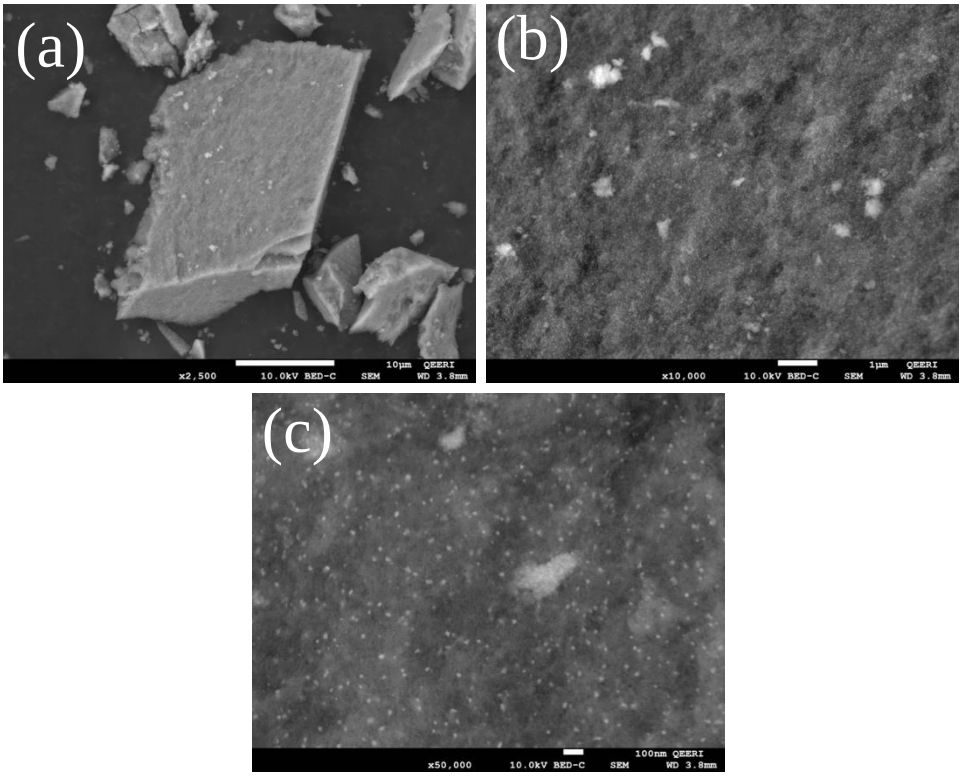

Figure 24: SEM images of reduced Ni_8Cu_1/Al_2O_3 SG Catalyst

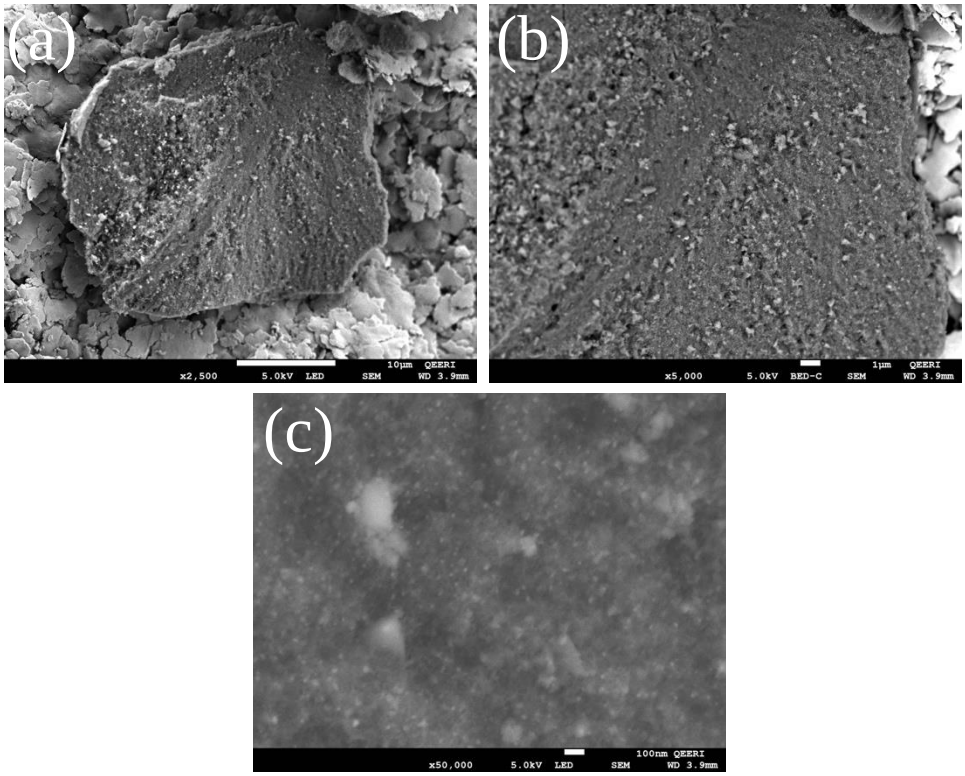

Figure 25: SEM images of reduced Ni/Al_2O_3 CP Catalyst

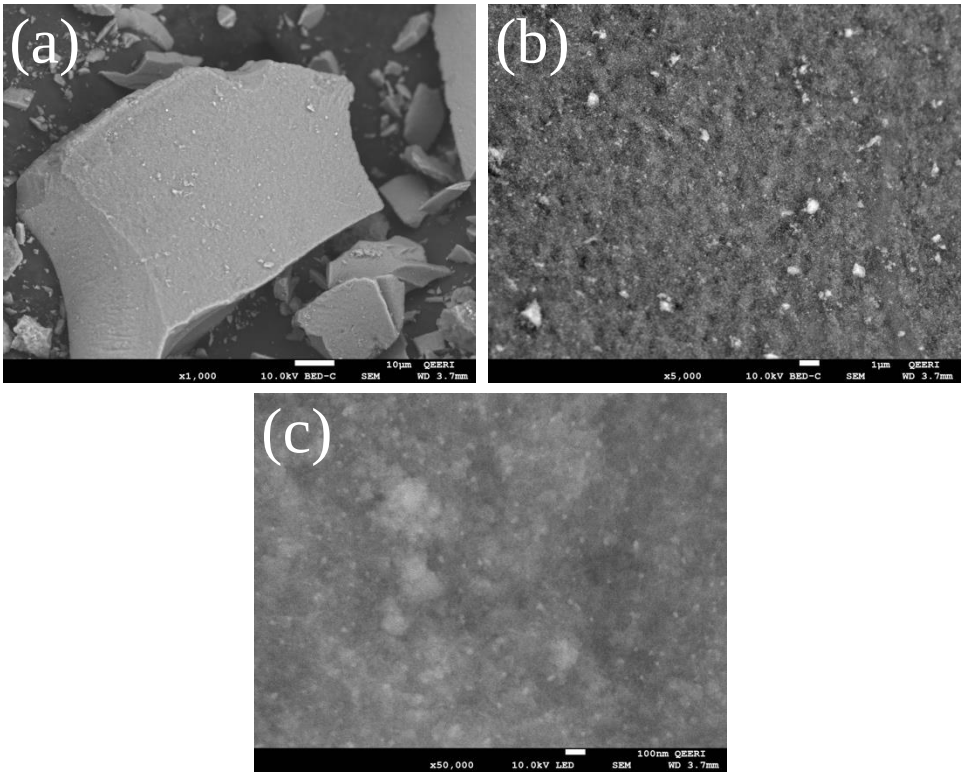

Figure 26: SEM images of reduced Ni_8Cu_1/Al_2O_3 CP Catalyst

EDS analysis was performed on large areas for each catalyst sample to perform a semi-quantitative analysis of the bulk composition. The areas used to perform the bulk EDS analysis are presented in Figure 27, and the results are summarized in Table 9. EDS analysis confirms that small particles observed on the surface are indeed Nickel and Copper. Monometallic samples present a Nickel weight percent of 14.63 wt.% for the SG variant and 15.32 wt.% for the CP catalyst. This is larger than the amount of Nickel introduced into the system (10 wt.%). The difference between the expected and the observed values could be due to the nature of the studied particles. These particles might have a more significant concentration of Nickel compared to other particles. In all cases, EDS mapping is a semi-quantitative technique. The difference between the two values is not substantial enough to be a source of concern. As for the bimetallic catalysts, the measured Nickel wt.% was determined to be 12.95 wt.% for the SG catalyst and 13.20 wt.% for the CP catalyst.

The lower percentage of Nickel measured is expected as the amount of Nickel introduced into each of these systems is lower than the monometallic variants. However, these values are higher than the expected Nickel loading for each of these systems. This can be explained in the same manner as the phenomena observed in the monometallic sample. As for the Copper loadings in the bimetallic samples, the measured copper wt.% was determined to be 1.29 wt.% for the SG catalyst and 1.26 wt.% for the CP catalyst. Compared to the respective nickel loadings in the bimetallic samples, this sets the loading of copper in the “low” to “mid” region. This result is close to the expected value.

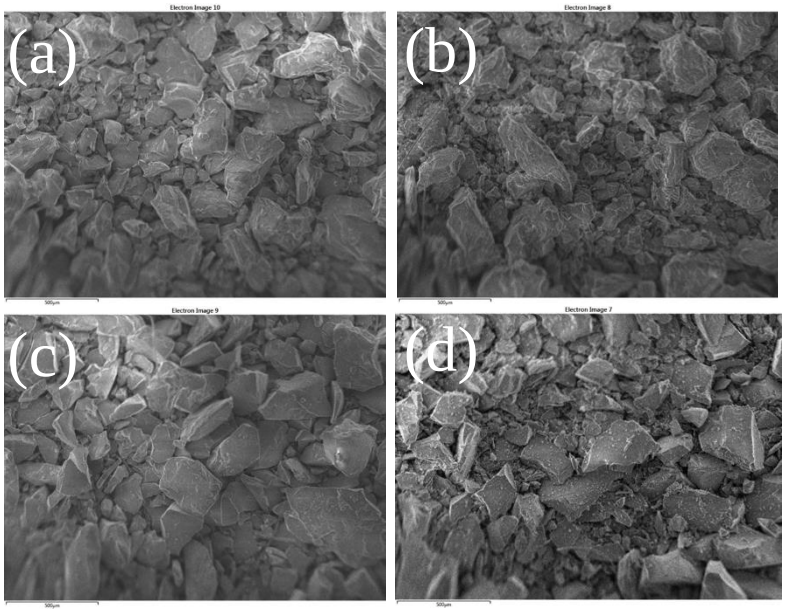

Figure 27: Areas used to perform EDS analysis for (a): Ni/Al_2O_3 SG; (b): Ni_8Cu_1/Al_2O_3 SG; (c): Ni/Al_2O_3 CP; (d): Ni_8Cu_1/Al_2O_3 CP

Table 9: Bulk EDS results for reduced catalysts

Catalyst	Ni (wt %)	Cu (wt %)	Al (wt %)	O (wt %)
$Ni/\gamma\text{-}Al_2O_3$-SG	14.63	-	40.96	44.41
$Ni_8Cu_1/\gamma\text{-}Al_2O_3$-SG	12.95	1.29	42.23	43.54
$Ni/\gamma\text{-}Al_2O_3$-CP	15.32	-	40.36	44.32
$Ni_8Cu_1/\gamma\text{-}Al_2O_3$-CP	13.20	1.26	41.70	43.85

4.2.6. Transmission Electron Microscopy of Reduced Catalysts

The TEM, HR-TEM, HAADF-STEM images, elemental maps of the reduced monometallic, and particle size statistics of reduced SG and CP catalyst are presented in Figure 28 to Figure 31. Figure 28 presents the images and statistics associated with the reduced Ni/Al_2O_3-SG catalyst. Figure 28 (a) shows a large particle with smaller and darker particles dispersed on it. To study the identity of each of these particles, EDS mapping was performed. As depicted in Figure 28 (b), the large particle is mainly aluminum and oxygen, which is the Al_2O_3 support. The smaller red particles are metallic nickel. HR-TEM was performed on different nickel particles to study their nature. Figure 28 (c) presents a single nickel particle with an inter-fringe spacing of 0.177nm

corresponding to the Ni(200) plane [48]. Figure 28 (d) shows another nickel particle with an inter-fringe spacing of 0.20 nm corresponding to the Ni(111) plane [48]. HR-TEM analysis of other nickel particles showed that most particles corresponded to the Ni(111) plane. Figure 28 (f) presents the particle size distribution analysis results. The particle sizes range from 2.43-26.95 nm, with a mean of 9.72nm and a median of 9.23 nm.

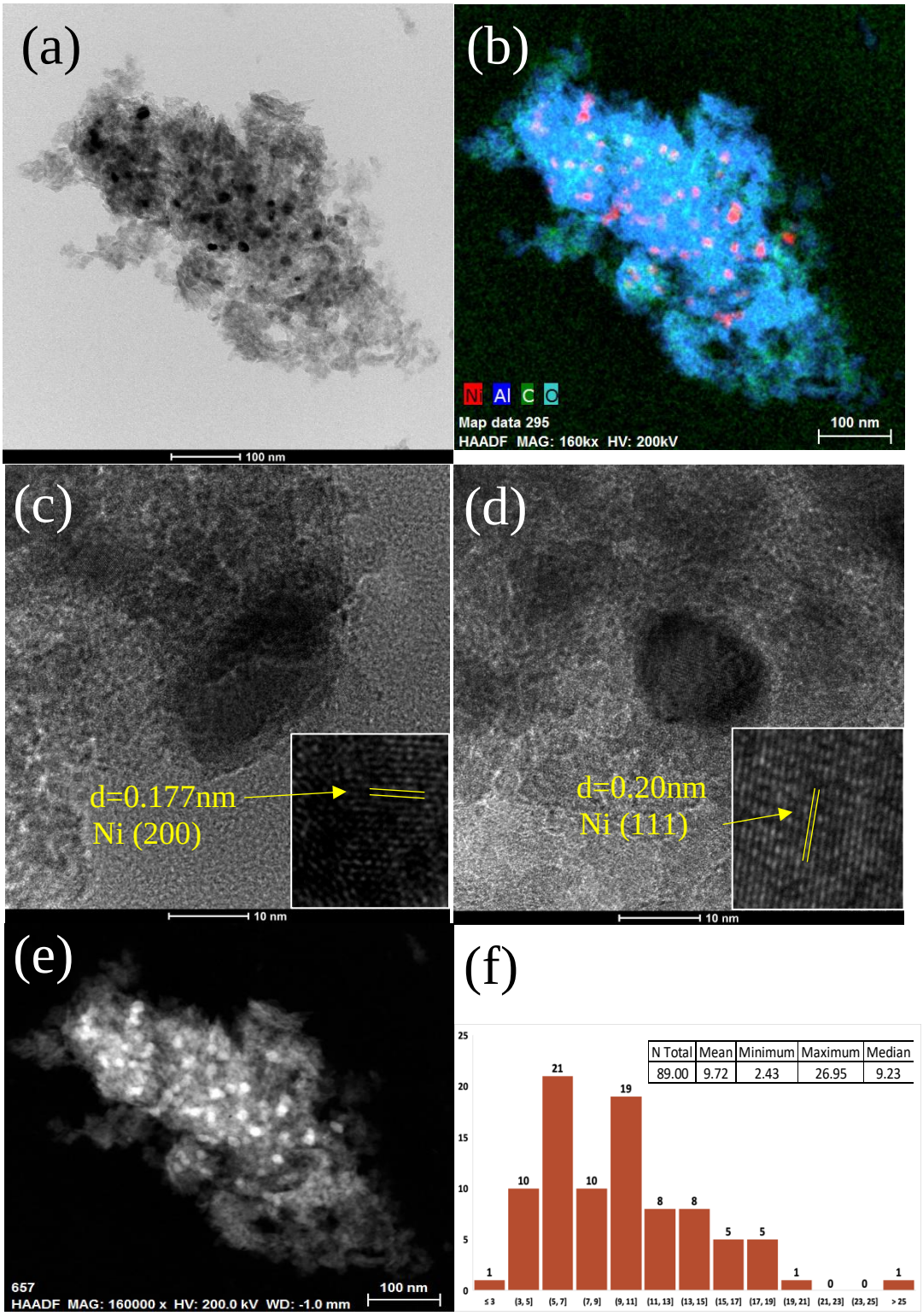

Figure 28: TEM images of reduced Ni/Al_2O_3 SG Catalyst

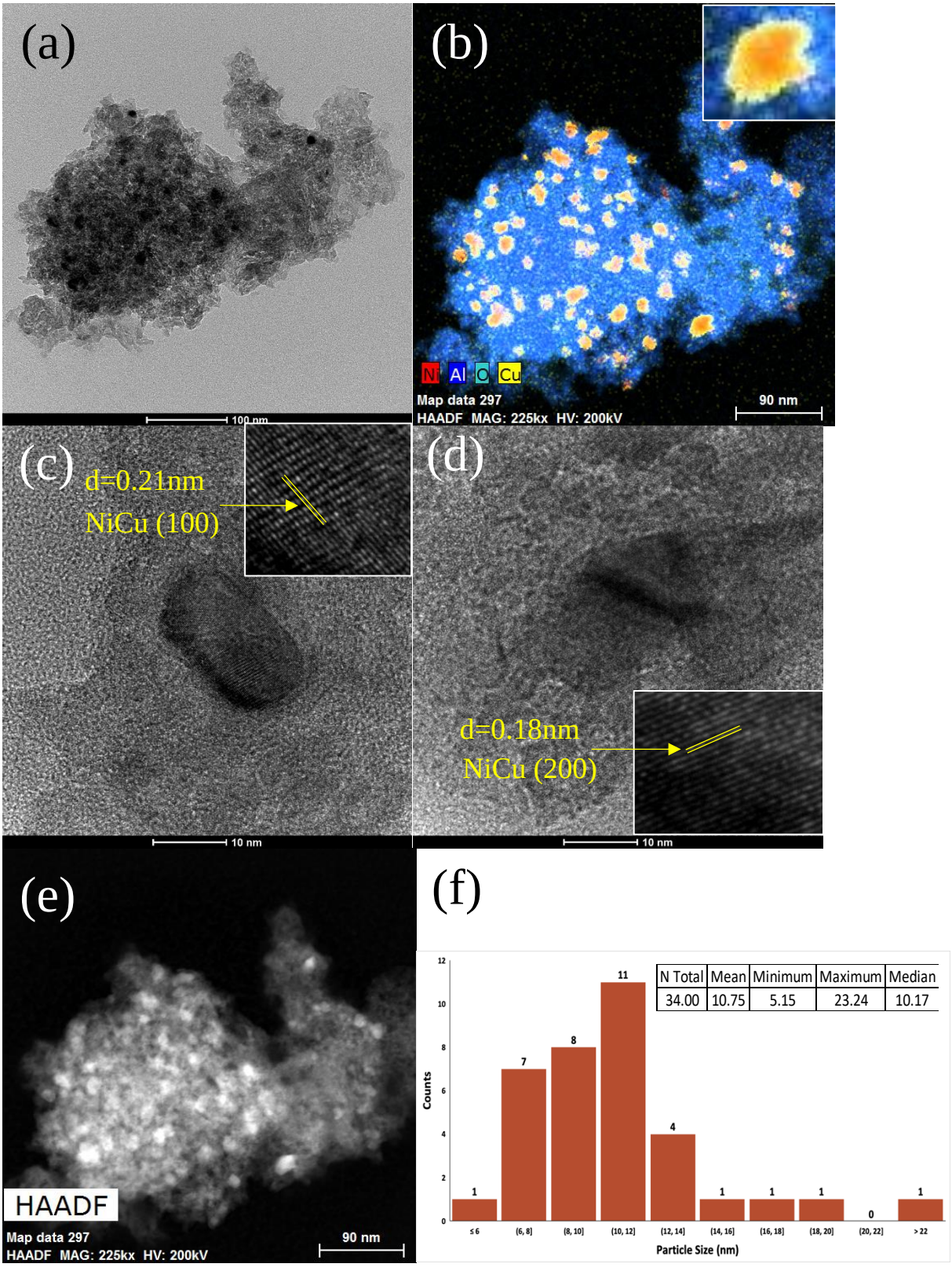

Figure 29: TEM images of reduced Ni_8Cu_1/Al_2O_3 SG Catalyst

The TEM and PSD results for the reduced Ni_8Cu_1/Al_2O_3 SG catalyst are presented in Figure 29. Figure 29(a) presents a large particle with smaller dispersed particles on its surface. EDS mapping presented in Figure 29(b) shows that the large particle is constituted of the alumina support. The smaller particles dispersed on the support's surface are both nickel and copper. It is clear that Cu encapsulated Ni active sites in a core-shell manner rather than forming an alloy.

Interestingly, there is a large concentration of copper layers on the active nickel sites. These thick layers form a local "high loading" of copper in a core-shell manner, which goes against the primary goal of inserting a "medium loading" of copper on the active sites. HR-TEM presented in Figure 29(c) shows the presence of a Ni-Cu(111) phase, which is characterized by an inter-fringe spacing of 0.21nm [27,49]. Furthermore, the HR-TEM of another particle presented in Figure 29(d) shows the presence of the Ni-Cu(200) phase with an inter-fringe spacing of 0.18nm[74]. PSD analysis results are presented in Figure 29(f). The particle sizes resided within a range of 5.15-23.24nm. The mean of the measured particle sizes was 10.75nm, whereas the median particle size was 10.17nm. Compared with the monometallic variant of this catalyst, the average particle size found in the bimetallic catalyst is slightly larger. It is worthy to note that the total number of particles observed in the PSD analysis of the bimetallic catalyst was much smaller than that of the monometallic catalyst. This makes it difficult to compare the obtain results for the two catalysts directly.

The TEM and PSD results for the reduced Ni/Al_2O_3-CP catalyst are presented in Figure 30. Figure 30(a) shows a large particle with finer particles dispersed on its surface. EDS mapping presented in Figure 30(b) reveals that the large particle is the alumina support, whereas the smaller particles on its surface are nickel. HR-TEM of two nickel particles presented in Figure 30(c) shows these particles are classified as the Ni(111) phase with an inter-fringe spacing of 0.20 nm. HR-TEM of a third particle presented in Figure 30(d) shows that this particle is the Ni(200) phase with an inter-fringe spacing of 0.177 nm. PSD analysis results for the monometallic CP catalyst are presented in Figure 30(f). Analysis shows that this catalyst's active metal particle sizes are within a range of 1.08-28.06 nm. The mean for these particles was determined to be 9.77 nm, whereas the median particle size was 9.09nm. These particle size statistics for the CP monometallic catalyst are almost identical to those found in its SG counterpart.

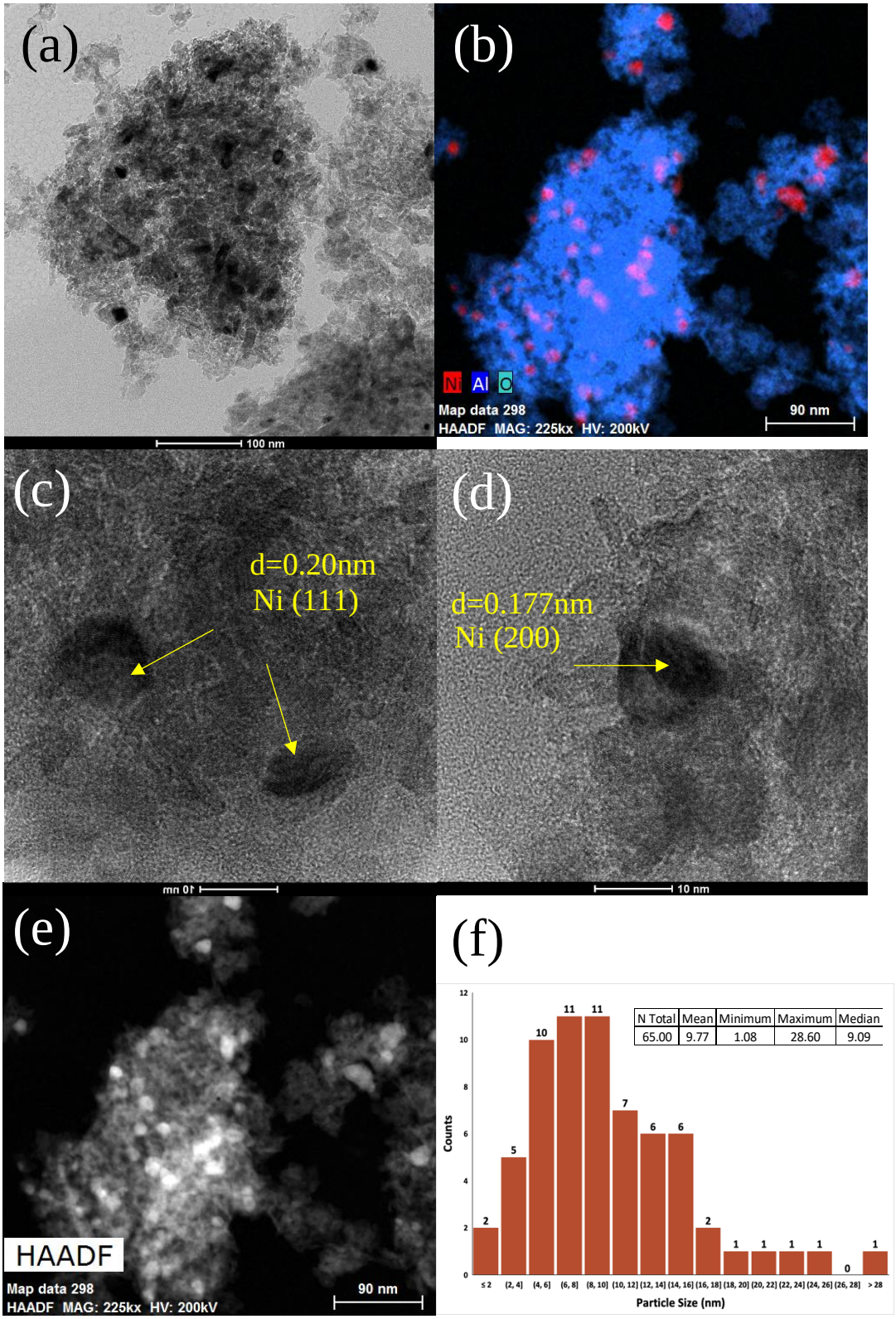

Figure 30: TEM images of reduced Ni/Al_2O_3 CP Catalyst

The TEM and PSD results for the reduced Ni_8Cu_1/Al_2O_3-CP catalyst are presented in Figure 31. Figure 31(a) shows a large particle with smaller particles dispersed on its surface. EDS mapping of the particle presented in Figure 31(b) shows that the large particle is the alumina support, whereas the smaller particles are nickel and copper. Similar to what was observed in the bimetallic SG catalyst EDS mapping of Figure 29(b), the copper particles form a thick layer on top of the active nickel sites creating a local "high loading" of copper. This is unfavorable as the goal of the preparation was to introduce copper in a "medium loading" manner. HR-TEM of a Nickel particle presented in Figure 31(c) shows a Ni-Cu (111) phase with an inter-fringe spacing of 0.21 nm. HR-TEM of two other particles presented in Figure 31(d) shows that one particle is Ni-Cu (111) as well, whereas the other particle is Ni-Cu(200) with an inter-fringe spacing of 0.18 nm. PSD analysis results of the bimetallic CP catalyst are presented in Figure 31(f). The measured particle sizes were within a range of 2.73-25.28 nm. The calculated mean of the particle sizes was 11.09 nm, whereas the median particle size was 9.99 nm. Compared to the monometallic variant of this catalyst and the SG bimetallic variant, it can be inferred that the average particle size in this catalyst is slightly larger in both cases.

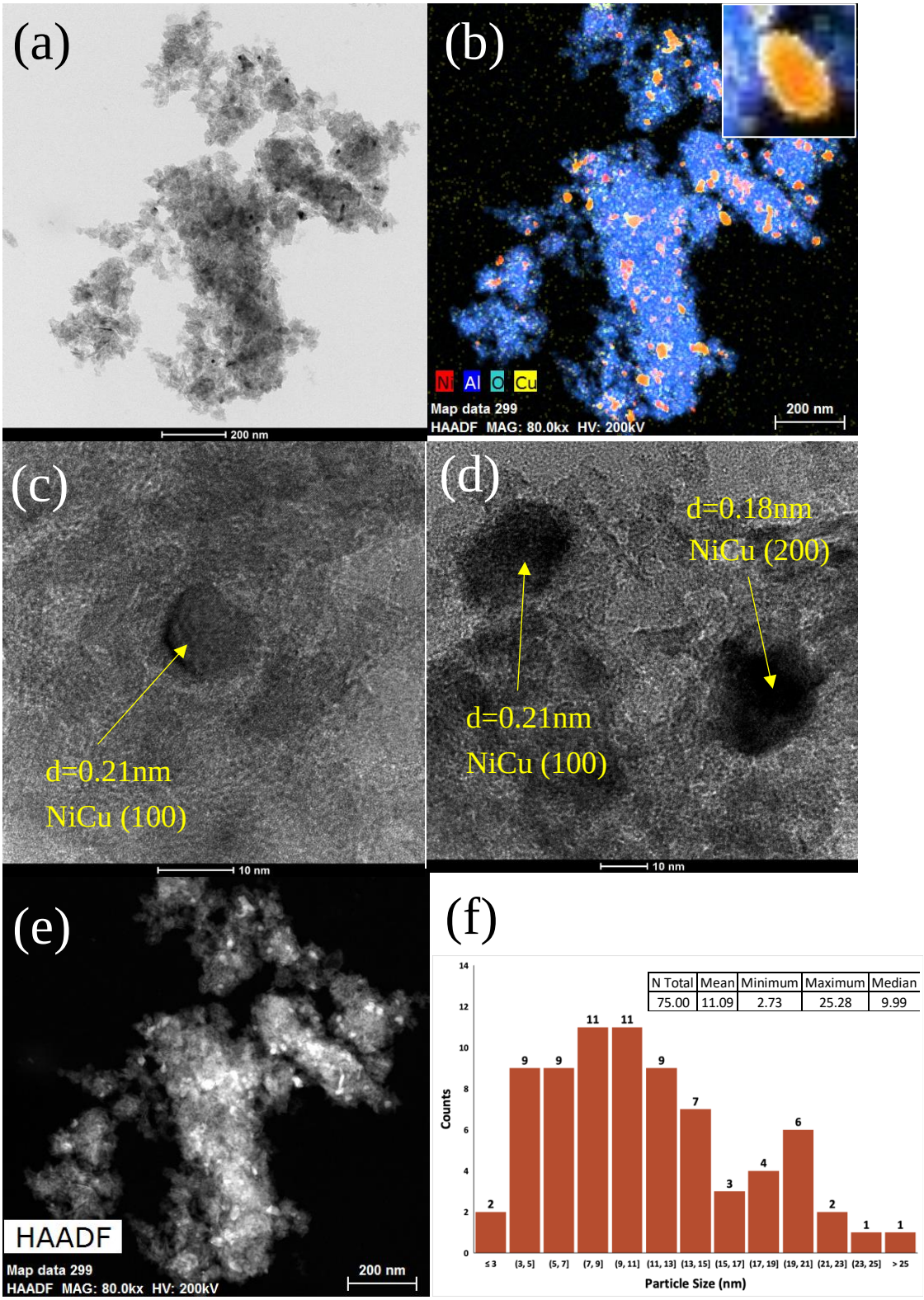

Figure 31: TEM images of reduced Ni_8Cu_1/Al_2O_3 CP Catalyst

4.2.7. Short Time on Stream Catalytic Performance Study for DRM

The short time on stream DRM test results are presented in Figure 32 to Figure 34. Observing methane and carbon dioxide consumption rates in Figure 32 and Figure 33, respectively, the monometallic catalysts clearly outperform their bimetallic counterparts. Both monometallic catalysts perform in a near-identical manner where the rates remain stable throughout the entire 20h test. When studying the rate of methane consumption, the monometallic catalysts present stable rates which hover between 0.080 and 0.085 mol/min/g_{Ni}. However, the bimetallic SG catalyst presents a lower rate of methane consumption which starts at around 0.055 mol/min/g_{Ni} and drops to approximately 0.050 mol/min/g_{Ni}. These rates are lower when compared with the rates of methane consumption calculated for both monometallic catalysts. In terms of stability, the SG bimetallic catalyst performs close to the monometallic catalysts. The poorest performance was observed when studying the bimetallic CP catalyst. The methane consumption rate for this catalyst starts at around 0.045 mol/min/g_{Ni}, then rapidly drops to approximately 0.028 mol/min/g_{Ni} in less than 2 hours. After this point, the rate slowly increases until a maximum is attained at around the 10-hour mark, where the rate was about 0.032 mol/min/g_{Ni}. The rate then slowly drops to around 0.030 mol/min/g_{Ni} at 20 hours TOS.

When focusing on the rates of CO_2 consumption in Figure 33, the trends observed are identical to those identified in Figure 32. The monometallic catalysts present a near-identical performance where the rate of CO_2 consumption for both samples is stable and hovers between 0.095 and 0.098 mol/min/g_{Ni}. The rates of CO_2 consumption presented by these catalysts are higher than the rates they presented for CH_4 consumption. This is expected, as the RWGS results in higher consumption of CO_2.

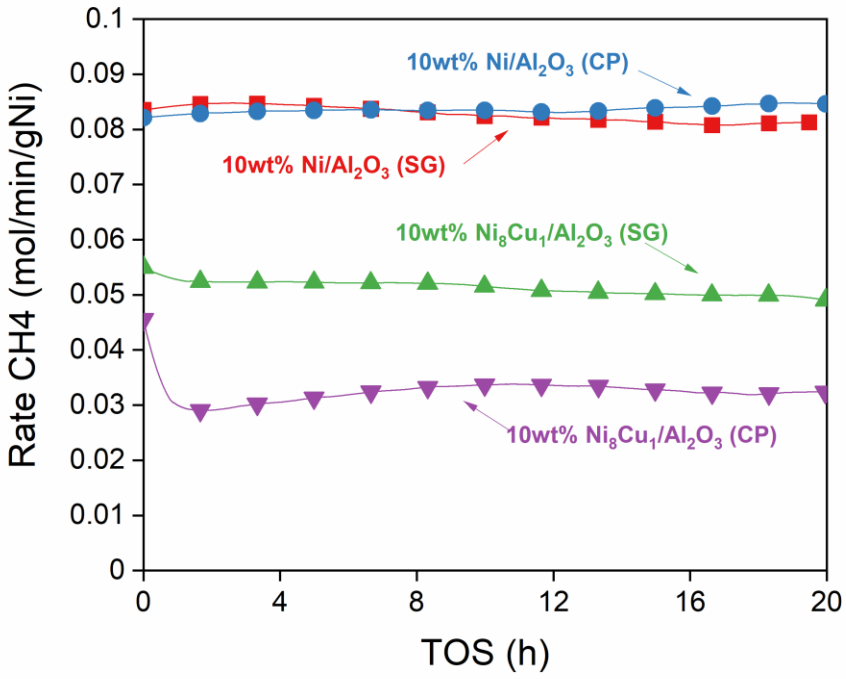

Figure 32: Methane consumption rates for short time on stream DRM studies at 650 °C and CH_4:CO_2 = 1:1

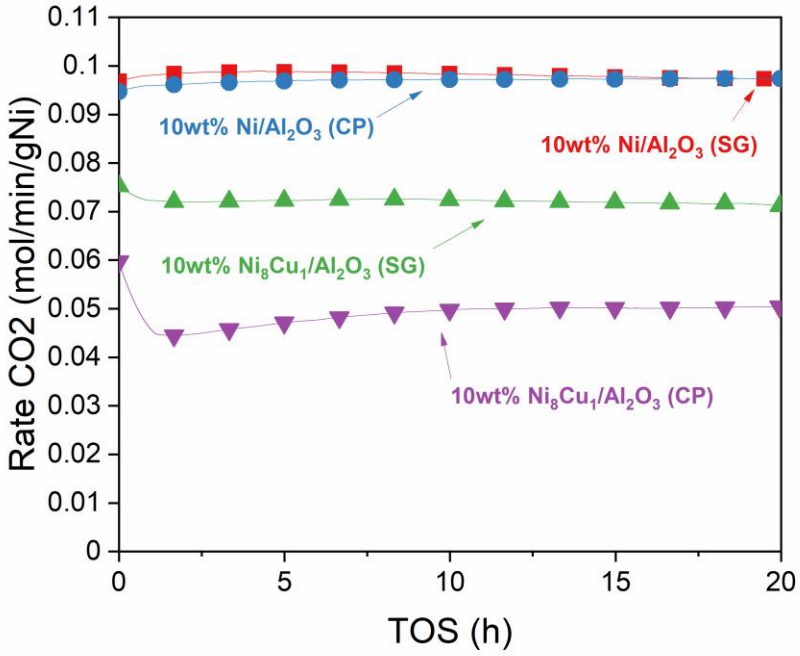

Figure 33: Carbon dioxide consumption rates for short time on stream DRM studies at 650 °C and CH_4:CO_2 = 1:1

When studying the rate of CO_2 consumption for the SG bimetallic catalyst, the rate begins at about 0.075 mol/min/g_{Ni}. The rate then drops to about 0.070 mol/min/g_{Ni} after 2 hours and remains relatively constant at this value till 20 hours TOS. These rates are lower than what was observed for both monometallic catalysts. Similar to what was observed in Figure 32, the bimetallic CP catalyst presents the lowest rates for CO_2 consumption throughout the entire 20 hours TOS test. The rate starts at about 0.060 mol/min/gNi and rapidly drops to about 0.045 mol/min/gNi in less than 2 hours. The rate then slowly increases till a maximum is attained at around 10 hours, where the rate stabilizes at a maximum value of 0.050 mol/min/gNi. The rate of CO_2 consumption for the bimetallic CP catalyst remains at this maximum value till 20 hours TOS.

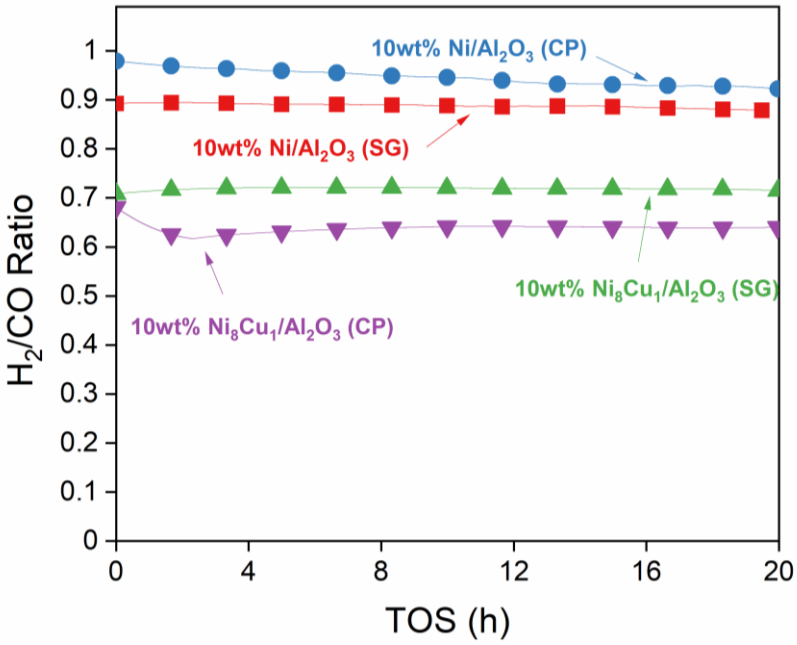

Figure 34: H_2/CO Ratio of for Short Time on Stream DRM Studies at 650 °C and CH_4:CO_2 = 1:1

Furthermore, the H_2/CO ratio throughout 20 hours TOS was studied for all catalysts, and the results are presented in Figure 34. The monometallic CP catalysts presented the highest H_2/CO ratio throughout 20 hours TOS, where the ratio began at the stoichiometric value of 1 and declined to about 0.095 at 20 hours TOS. As for the monometallic SG catalyst, the H_2/CO ratio started at a

lower value of 0.090 and remained constant at this value till 20 hours TOS. As for the bimetallic SG catalyst, the H_2/CO ratio began at a value of 0.070 and remained stable till 20 hours TOS. This value is lower than that observed for both monometallic catalysts. Once again, the poorest performance was observed when studying the bimetallic CP catalyst. The H_2/CO ratio for this catalyst started at around 0.69 and dropped to 0.62 at around the 2 hours mark. After this point, the ratio slowly increased to a slightly higher maximum value of 0.64. The CP catalyst maintained this maximum value till 20 hours TOS.

The analysis of the short TOS catalyst performance results shows very clearly that monometallic catalysts outperform bimetallic catalysts regardless of the preparation technique. The performance of the monometallic catalysts was nearly identical in terms of CH_4 and CO_2 rates of consumption. The monometallic CP catalyst presented a slightly more advantageous performance for H_2/CO ratio. In monometallic catalysts, the preparation technique did not seem to cause any significant differences in catalyst performance. This result is not surprising, as detailed characterization of these catalysts did not present any major differences in terms of particle size, morphology, chemical species present, and their states.

However, the fact that monometallic catalyst outperformed their bimetallic counterparts was not expected. The first section of this study established that nickel catalysts doped with a medium loading of copper and prepared by the incipient wetness impregnation technique outperformed their monometallic variants. At first, this result is surprising; however, the EDS mapping performed for the bimetallic catalysts (Figure 29(b) and Figure 31(b)) synthesized using the SG, and CP techniques present a clear answer. Although the amount of copper introduced in both SG and CP systems was meant to create a medium loading of copper, the EDS maps clearly show that the concentration of copper on the active nickel sites is high. This created a local high

loading of copper. As a result, the thick layers of copper formed on the active sites reduced the amount of nickel available to take part in the DRM reaction, thereby reducing the performance of both bimetallic catalysts synthesized by SG and CP.

To further study the difference in the performance of the synthesized catalysts, a series of characterization techniques were implemented on all spent catalysts. The results of these characterization techniques are presented in further sections of this study.

4.2.8. Characterization of Short Time on Stream Spend Catalysts

The spent catalysts after 20 hours TOS DRM at 650 °C were characterized by XPS and TEM. The amount of sample available was not sufficient enough to conduct other characterization techniques. The results of the techniques mentioned above will be discussed in this section.

4.2.8.1. Transmission Electron Microscopy of Short Time on Stream Spent Catalysts

The spent catalysts after short TOS DRM testing were characterized by TEM and EDS mapping. The results are presented in Figure 35 to Figure 42. The monometallic SG catalyst TEM EDS mapping and PSD results are shown in Figure 35, and the HR-TEM images are presented in Figure 36.

The images presented in Figure 35(a-c) show the formation of large particles on the support surface, most likely due to the sintering of active nickel sites. However, the majority of the particles observed were much smaller than the sintered particles. No carbon nanotubes were observed in any of the TEM images. EDS mapping of one monometallic SG catalyst particle is presented in Figure 35(d). The species highlighted in green is carbon, and its formation on the catalyst surface is expected. The carbon build-up on this particle seems to be concentrated in areas where nickel is abundant. Coking of the catalyst surface area is detrimental to its activity; however, the activity data previously presented for this catalyst showed that CH4 and CO2 consumption rates remain

relatively stable throughout 20 hours TOS. The fact that the monometallic SG catalyst maintained a stable performance, despite the clear evidence of coking, leads to the conclusion that the amount of sample loaded into the reactor was very high. The 20 hours of TOS were insufficient to push the catalyst to its limit and observe its deactivation profile.

The PSD results for the monometallic SG catalyst are presented in Figure 35(f). The mean size for the observed particle was around 10.17 nm. This value is higher than that observed in the reduced version of this catalyst which was 9.72 nm. The larger mean particle size is most likely due to the sintering of nickel sites, with particles as large as 37nm observed. However, most nickel particles maintained a particle size closer to the reduced catalyst mean particle size. This is supported by the fact that the median value of particles observed in the spent catalyst was 9.22 nm.

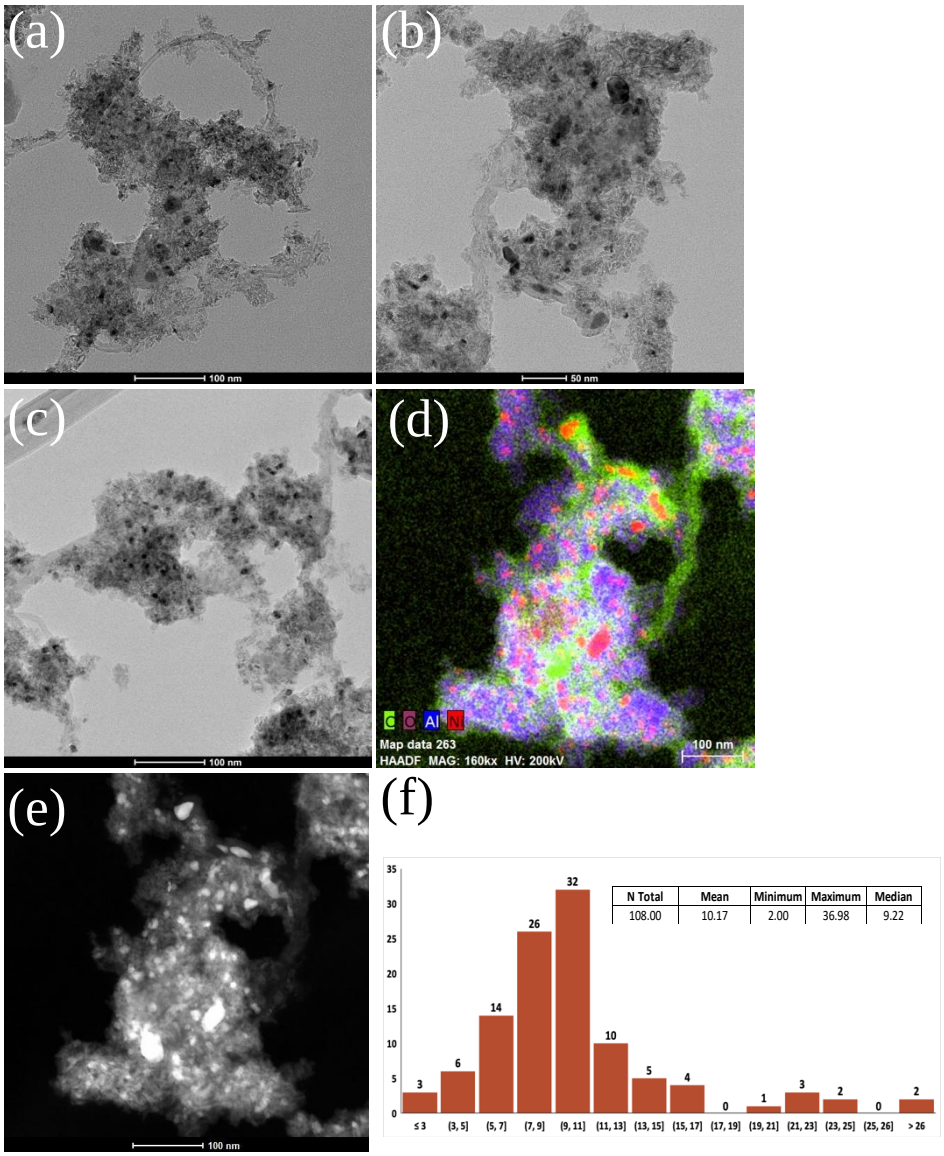

Figure 35: TEM images of spent short TOS Ni/Al_2O_3 SG Catalyst

To further study the impact of DRM TOS on the active nickel sites of the monometallic SG catalyst, HR-TEM studies were conducted, and the results are presented in Figure 36.

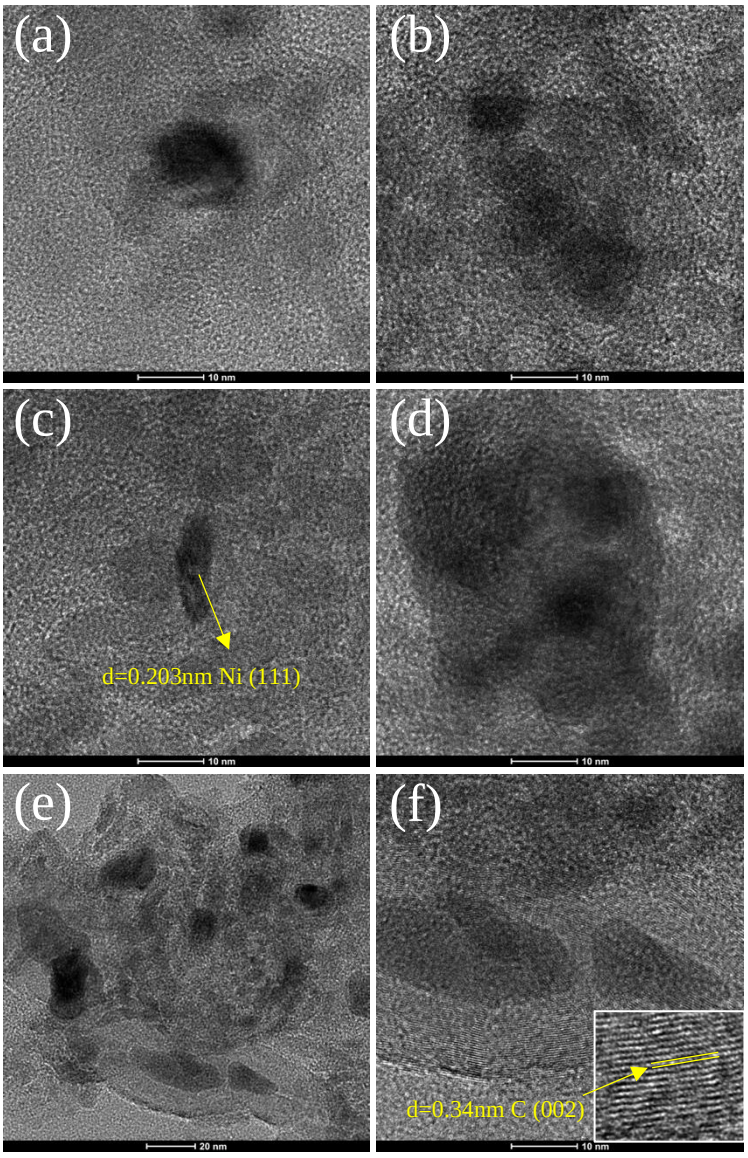

Figure 36: HR-TEM images of used short TOS Ni/Al_2O_3 SG Catalyst

Figure 36(a-f) clearly shows the formation of carbonaceous species with an amorphous structure. The formed carbon tightly wraps the nickel particles and forms an onion-like shape. The carbon fringes could be identified, and it is clear that they are not uniformly structured. This type of carbon leads to catalyst deactivation since it completely blocks the access of reactants to the nickel site [75]. This form of carbon is the easiest to remove through oxidation [76]. It seems that the majority of carbon formed on the active sites in this catalyst is amorphous. Figure 36(f) shows

the formation of arranged layers of carbon around the nickel particles. The inter-fringe spacing of these layers was determined to be 0.34nm. This corresponds to the (002) plane of graphitic carbon. The evident encapsulation of several nickel particles in layers of carbon that deactivate the catalytic activity reinforces the previously mentioned claim that the amount of catalyst loaded was too high to observe a deactivation profile within 20 hours TOS.

The bimetallic SG catalyst TEM EDS mapping and PSD results are presented in Figure 37, and the HR-TEM images are presented in Figure 38. The images presented in Figure 37(a-c) do not show any excessively large particles. EDS mapping of a catalyst particle presented in Figure 37(d) shows the formation of carbon on areas where nickel particles are concentrated. The PSD analysis results are presented in Figure 37(f). The mean particle size was 11.05nm, which is slightly larger than the 10.75nm mean particle size for the reduced variant of this catalyst. The larger mean particle size occurs due to nickel particle sintering. Although the mean particle size for the spent variant of this catalyst is larger than that observed in its spent monometallic counterpart, the largest particle size observed was around 20.1 nm. This does not necessarily mean that this variant of the catalyst has a higher resistance to sintering, as TEM is a technique highly influenced by the observed particles, which may not reflect the bulk property properly. In general, most of the particles observed in this catalyst seem to have maintained their state before 20 hours TOS. This is supported by the fact that the median particle size observed in this catalyst was found to be 10.29nm, which is only slightly higher than the median value of 10.17nm observed before DRM testing.

To further study the impact of DRM TOS on the active nickel sites of the bimetallic SG catalyst, HR TEM analysis was implemented on several nickel particles, and the images are presented in Figure 38.

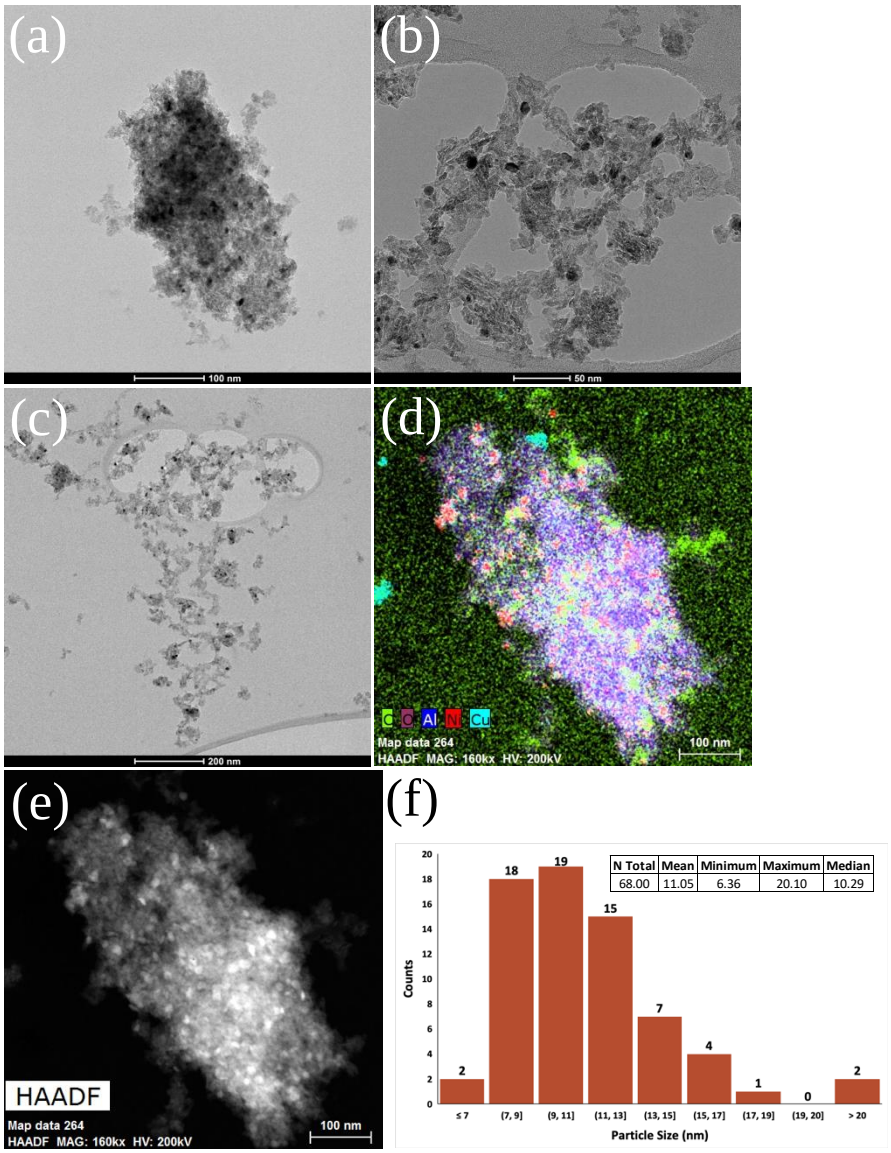

Figure 37: TEM images of used short TOS Ni_8Cu_1/Al_2O_3 SG Catalyst

Figure 38(a-f) shows that several nickel particles are entirely encapsulated with carbonaceous species in an onion shape, similar to what was observed in the monometallic spent variant of this catalyst. The nickel sites observed in this catalyst had an inter-fringe spacing of

0.203nm and 0.18nm, corresponding to NiCu(111) and NiCu(200) planes, respectively. The carbon formed on these sites seems to be primarily amorphous. A few layers of semi-arranged carbon were found near the particles. The inter-fringe spacing of these layers was determined to be 0.34nm, which matches graphitic carbon very well. It is plausible to assume that if the catalyst were exposed to a longer TOS, then the graphitic carbon layers built around the nickel site would increase. It is worthy to note that neither the monometallic SG nor the bimetallic SG used catalyst had any formation of carbon nanotubes.

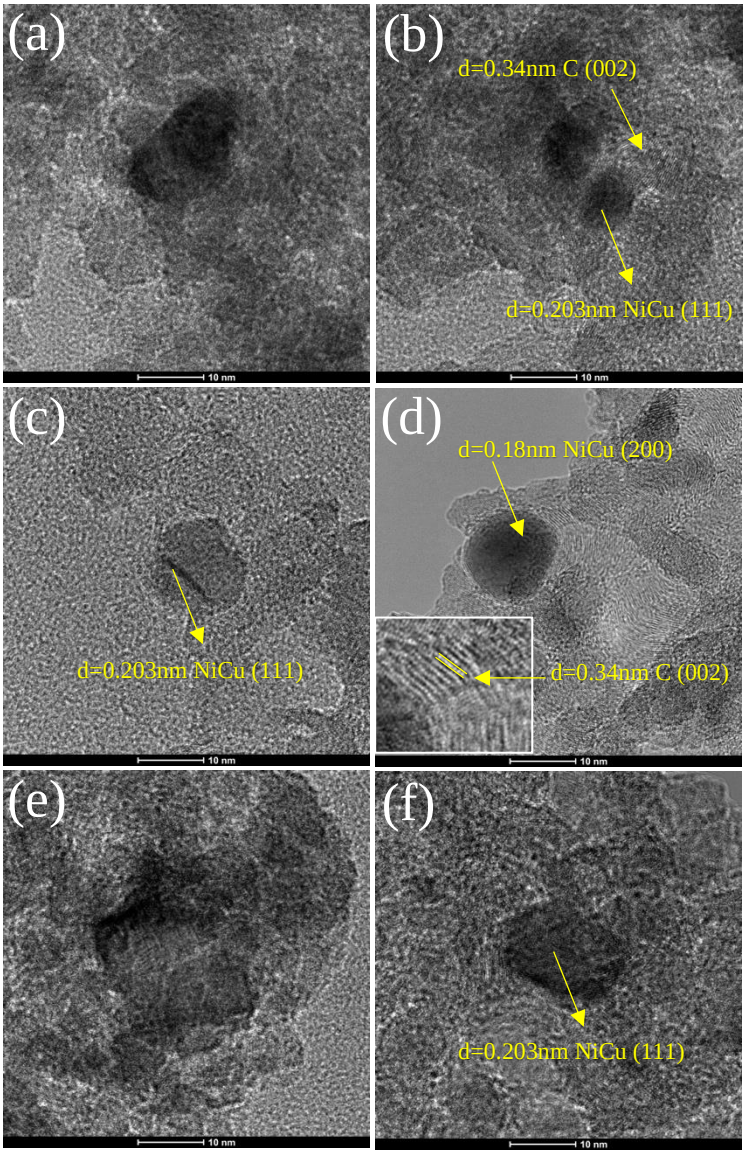

Figure 38: HR-TEM images of used short TOS Ni_8Cu_1/Al_2O_3 SG Catalyst

Moving on to the catalysts synthesized by the CP method, the TEM images, EDS mapping, and PSD results for the monometallic CP spent short TOS catalyst are presented in Figure 39. TEM images in Figure 39(a-c) show that several large nickel particles have formed, most likely due to sintering. The EDS mapping of a monometallic CP spent particle is presented in Figure 39 (d). The image clearly shows the dense formation of carbon in an area where nickel particles are present.

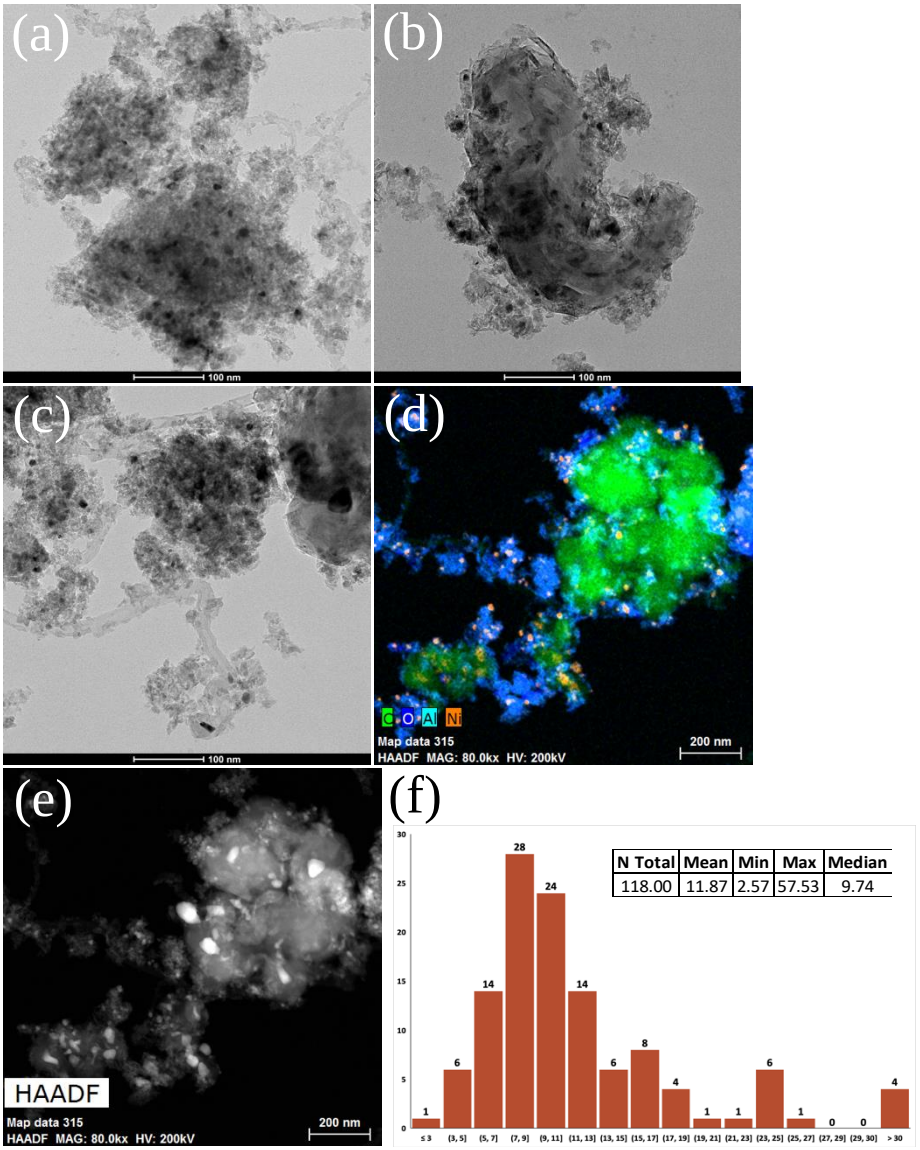

Figure 39: TEM images of used short TOS Ni/Al_2O_3 CP Catalyst

As for the PSD for this spent catalyst, the results are summarized in Figure 39(f). The calculated mean particle size was 11.87nm, which is larger than the 9.77nm reduced catalyst mean particle. The monometallic CP catalyst seems to have been impacted by sintering to a greater degree when compared with the SG monometallic catalyst. This is more evident when noticing that particles as large as 57.53nm were formed. Furthermore, the median particle size for this spent catalyst was 9.74nm, higher than the 9.09nm median particle size in the reduced variant of this catalyst.

The HR-TEM images of nickel particles in the spent monometallic CP catalyst are presented in Figure 40. Several layers of graphitic carbon were observed encapsulating the nickel particles in Figure 40(a,d,e). It is clear that the carbonaceous species formed on this catalyst are more structured. Figure 40(d) shows a nickel particle encapsulated in several graphitic carbon layers in an onion shape. These layers are stacked circularly. Figure 40(e) shows that a carbon nanotube consisting of graphitic carbon was formed. Furthermore, certain particles were encapsulated with less structured amorphous carbon Figure 40(b,f).

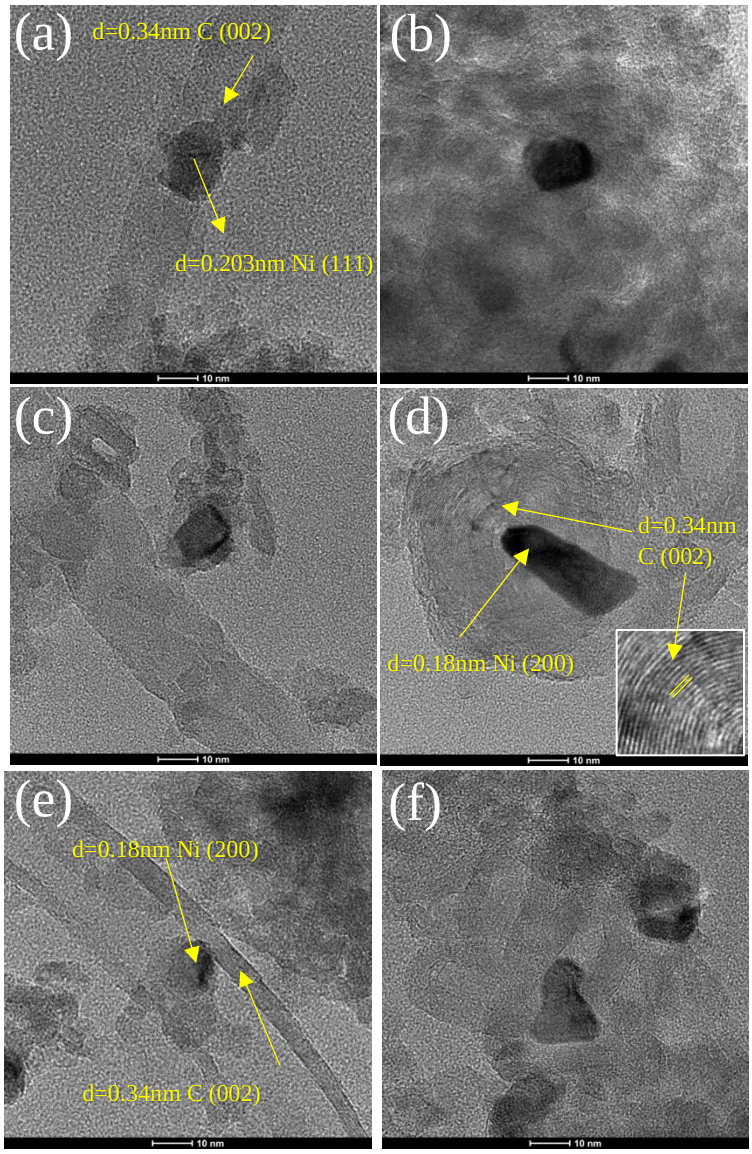

Figure 40: HR-TEM images of used short TOS Ni/Al_2O_3 CP

Finally, the bimetallic CP spent catalyst was studied. The TEM images, EDS mapping, and PSD results for this spent catalyst are presented in Figure 41.

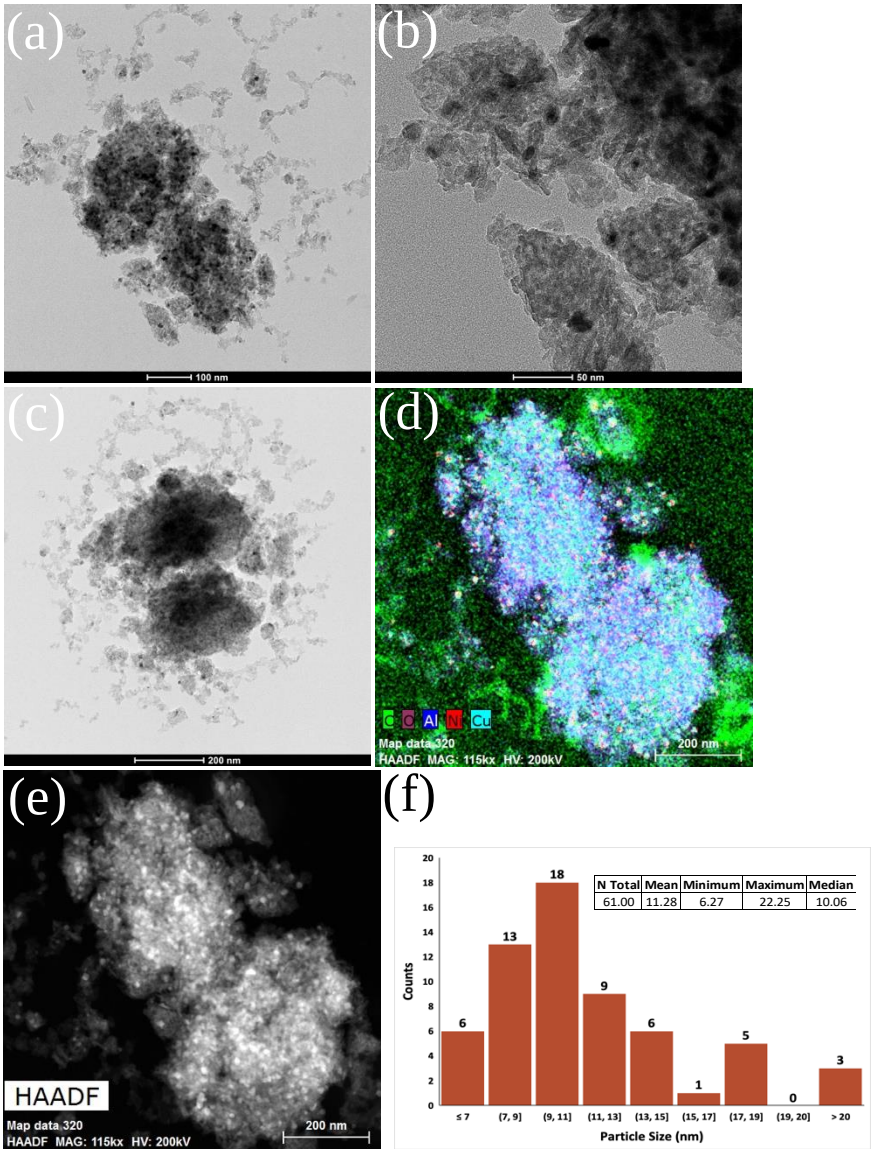

Figure 41: TEM images of used short TOS Ni_8Cu_1/Al_2O_3 CP Catalyst

The images presented in Figure 41(a-c) show that large particles of nickel similar to those formed in the monometallic CP used catalyst were not formed. EDS mapping presented in Figure 41(d) shows that carbon was formed on areas with a high nickel concentration. An interesting phenomenon observed was that the catalyst particle had a very high concentration of copper on its surface. This could result from copper segregation on the catalyst surface, which lowers the catalyst activity by blocking the access of reactants to the active nickel sites.

Furthermore, the concertation of copper on the surface of the CP bimetallic spent catalyst seems to be higher than that observed in the spent bimetallic SG catalyst. The higher concertation of inactive copper in return leads to reduced catalytic activity and explains why this catalyst exhibited the most deficient performance amongst all synthesized catalysts.

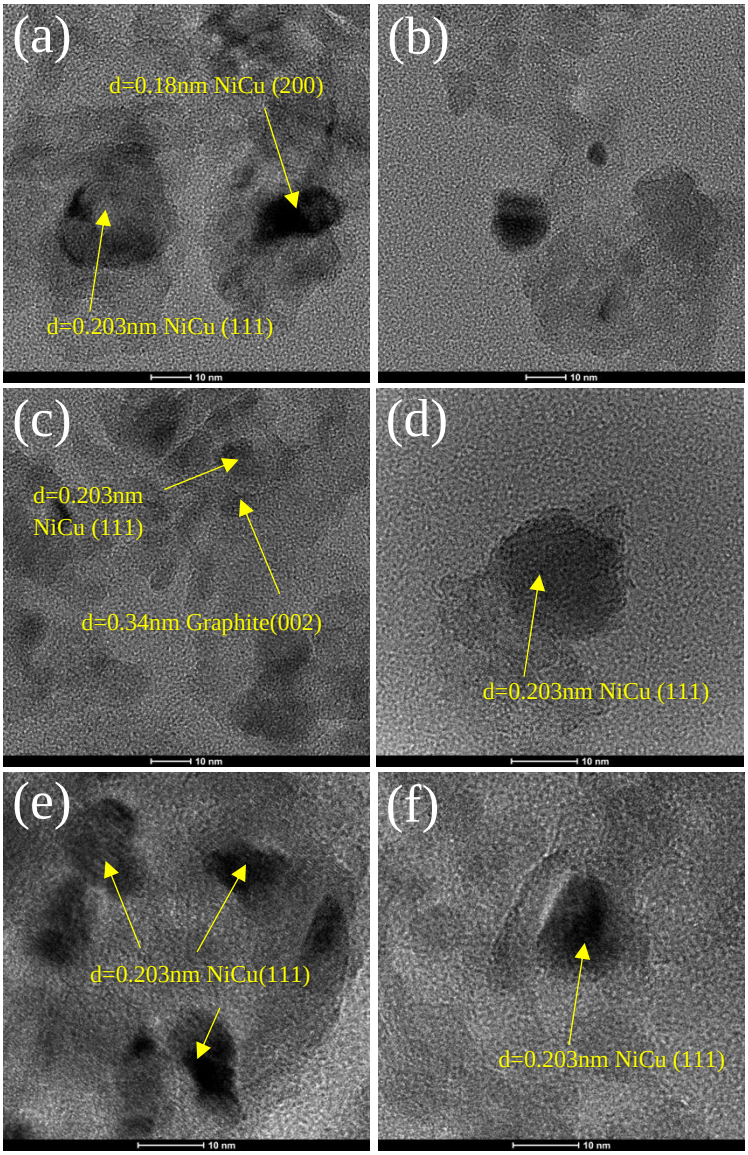

Figure 42: HR-TEM images of used short TOS Ni_8Cu_1/Al_2O_3 CP Catalyst

The HR-TEM images of spent bimetallic CP catalyst are presented in Figure 42. The HR-TEM images of nickel particles show that they are encapsulated in amorphous carbon in onion shapes. These carbonaceous layers are unstructured, and only a very small layer was found to have an inter-fringe spacing of 0.34nm corresponding to graphitic carbon in Figure 42(c). It makes sense that the carbon formed on the nickel particles lacked structure, as the concentrated layers of copper on their surface lowered the rate of consumption of CH_4 and CO_2. This, in return, reduced the rate of reactions which lead to coke formation.

From what was presented, it is clear that the amount of catalyst used was very high. The excess number of active sites available maintains the catalytic activity despite other active sites completely encapsulated with carbon. The monometallic CP catalyst presented the highest degree of sintering compared to all other catalysts, as the mean particle size increased by about 2nm compared to its reduced form. The other catalysts did experience an increase in their mean particle size due to sintering; however, the increase was not as high as the monometallic CP spent catalyst.

As for the carbon species formed on the active nickel sites, it is evident that the vast majority of catalysts were coked with amorphous carbon, which encapsulates the active nickel sites. Some particles presented the formation of graphitic carbon layers. The catalyst with the heaviest coking was the monometallic CP catalyst. Nickel sites were covered with layers of graphitic carbon and amorphous carbon, with a carbon nanotube formed. As for the bimetallic CP catalyst, the formed carbon species were the least structured. The high concentration of copper segregated on its surface decreased the access of reactants to the active site, thereby reducing the rate of coke formation.

4.2.8.2. X-ray Photoelectron Spectroscopy of Short Time on Stream Spent Catalysts

XPS analysis was conducted for the spent catalysts after 20 hours TOS DRM at 650 °C. The calculated atomic percentages of elements identified by XPS analysis of spent catalysts are summarized in Table 10.

Table 10: Atomic percentages for elements observed in XPS analysis of spent short TOS catalysts

Short TOS Spent Catalysts	Ni (Atomic %)	Cu (Atomic %)	Al (Atomic %)	O (Atomic %)	C (Atomic %)
$Ni/\gamma\text{-}Al_2O_3$-SG	0.7	-	20.74	44.2	34.36
$Ni_8Cu_1/\gamma\text{-}Al_2O_3$-SG	0.64	0.13	32.02	53.77	13.44
$Ni/\gamma\text{-}Al_2O_3$-CP	0.78	-	30.03	54.84	14.35
$Ni_8Cu_1/\gamma\text{-}Al_2O_3$-CP	0.76	0.14	31.72	54.13	13.25

It is important to note that the carbon signal is affected by the carbon tape on which the sample is fixed to perform the analysis. The atomic carbon percentages clearly show that the monometallic SG catalyst presented the highest value at 34.36 at.% compared to the other catalysts with a carbon percentage ranging from 13.44 to 14.35 at.%. The fact that the monometallic SG catalyst presented a difference of this magnitude in terms of its carbon at.% could either be due to a higher degree of coking observed in this catalyst or due to the specific portion of the sample observed. The at.% of nickel observed in all catalysts was similar and ranged between 0.64 and 0.78 at.%. These values have dropped in comparison to those observed in the reduced variants of these catalysts. This is expected, as carbon formed on the catalysts minimizes the percentage of nickel exposed on the surface. The same behavior is observed when examining the copper at.% for the bimetallic variants of the SG and CP catalysts. The values have dropped compared to their reduced form, decreasing to 0.13-0.14 at.% of copper.

To further study the used catalysts, XPS was conducted. The obtained nickel spectra were deconvoluted and fitted. The graphs of the deconvoluted nickel plots are presented in Figure 43, and the observed peak positions are summarized in Table 11.

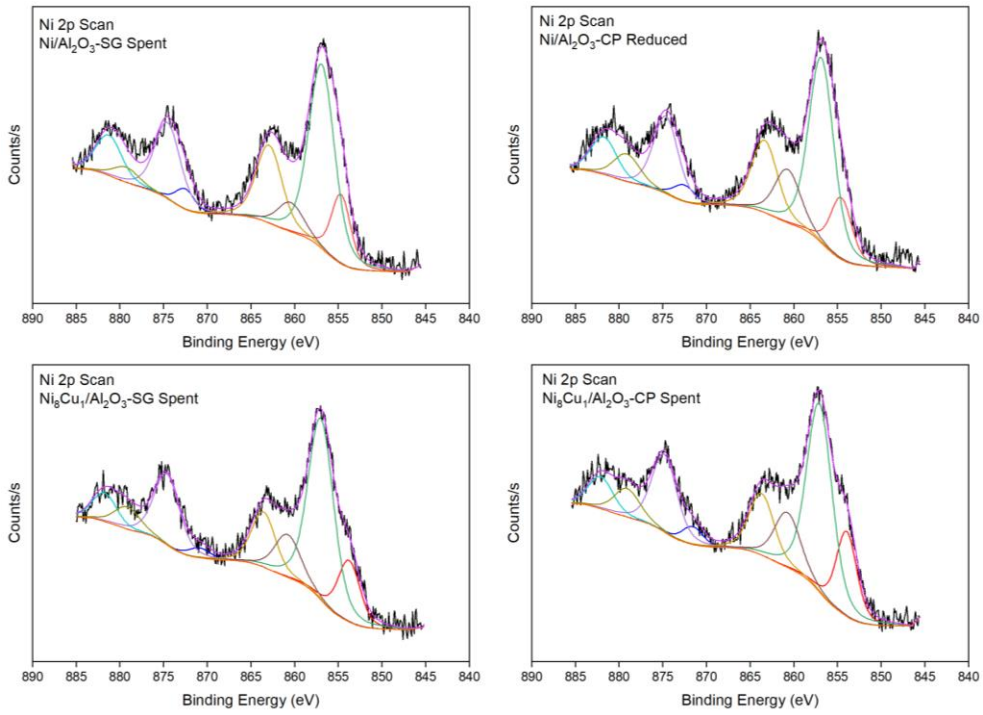

Figure 43: Deconvoluted nickel XPS spectra of spent short TOS catalysts

Table 11: Binding energies of peaks observed in deconvoluted graphs of spent short TOS catalyst nickel XPS spectra

Binding Energy (ev)	$Ni^0_{3/2}$	Ni $2p_{3/2}$	Satellite 1	Satellite 2	$Ni^0_{1/2}$	Ni $2p_{1/2}$	Satellite 3	Satellite 4
Ni/γ-Al_2O_3-SG	854.6	856.9	860.4	862.9	872.5	874.5	879.2	881.3
Ni_8Cu_1/γ-Al_2O_3-SG	853.7	856.9	860.8	863.5	870.8	874.6	879.1	881.7
Ni/γ-Al_2O_3-CP	854.7	856.9	860.5	863.1	872.3	874.5	878.5	881.3
Ni_8Cu_1/γ-Al_2O_3-CP	853.9	857.0	860.7	863.6	871.7	874.8	978.0	882.0

The expected peaks were observed in Figure 43. $Ni^0_{3/2}$ peaks were observed for all catalysts. Compared to their reduced form, the monometallic SG and CP catalysts experienced a shift in the binding energy of this peak to higher values of 854.6 eV and 854.7 eV, respectively. On the other hand, the bimetallic SG and CP catalysts experienced a shift to lower binding energies

of 853.7 eV and 853.9 eV, respectively. The higher binding energies of metallic nickel for the monometallic catalysts could indicate stronger metal-support interaction. As for the second peak observed in the nickel spectra, it was once again associated with the $NiAl_2O_4$ phase. All peaks were almost identical, with a value between 856.9-857.0 eV. The remaining satellite and shadow $Ni2p_{1/2}$ peaks were present, as expected.

Furthermore, the graphs of the deconvoluted copper plots are presented in Figure 44, and the observed peak positions are summarized in Table 12. Both catalysts experienced a shift to lower Cu $2p_{3/2}$ binding energies compared to their reduced form. The first peak for the bimetallic SG catalyst decreased to 933.0 eV(-0.6eV), while that of the bimetallic CP catalyst decreased to 933.4 eV(-0.2eV). These peaks remain within the range of the Cu_2O phase. The second peak of the Cu 2p spectra was also shifted to lower binding energies for both catalysts. The SG bimetallic catalyst had a peak of 935.4eV, whereas the CP bimetallic catalyst had a peak of 935.8eV. These peaks remain within the range of the CuO phase. The expected satellite and shadow $Cu2p_{1/2}$ peaks are present as well.

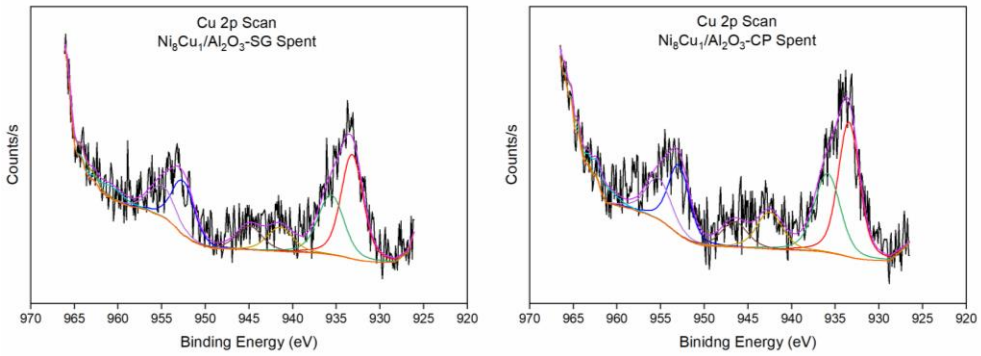

Figure 44: Deconvoluted copper XPS spectra of spent short TOS catalysts

Table 12: Binding energies of peaks observed in deconvoluted graphs of spent short TOS catalyst copper XPS spectra

Binding Energy (ev)	Cu $2p_{3/2}$	Cu $2p_{3/2}$	Satellite 1	Satellite 2	Cu $2p_{1/2}$	Cu $2p_{1/2}$	Satellite 3	Satellite 4
$Ni_8Cu_1/\gamma\text{-}Al_2O_3$-SG	933.0	935.4	941.4	944.9	952.4	954.7	960.7	964.3
$Ni_8Cu_1/\gamma\text{-}Al_2O_3$-CP	933.4	935.8	942.5	946.5	952.9	955.2	961.8	964.7

4.2.9. Long Time on Stream Catalytic Performance Study for DRM

The catalysts chosen for the long TOS DRM testing were the monometallic and bimetallic CP catalysts. Approximately 50 mg of each catalyst was loaded into the reactor to allow multiple characterization techniques to be conducted on the spent samples. The reaction was carried out at 650 °C with a feed composition of CH_4: CO_2=1:1. The reaction was allowed to progress for 70 hours TOS. The resultant reaction rates for CH_4 consumption, CO_2 consumption, and H_2/CO ratio are presented in Figure 45, Figure 46, and Figure 47, respectively.

As can be seen in Figure 45, the rate of consumption of CH_4 for the monometallic CP catalyst started at a value of about 0.0365 mol/min/g_{Ni}. In comparison, the bimetallic CP catalyst presented a lower initial rate of about 0.0275 mol/min/g_{Ni}. These initial rates are lower than what was observed in the short TOS DRM tests for these catalysts. This can be explained by the difference in the amount of catalyst loaded for each test. The mass of catalyst loaded for this test was more than double the quantity used for the short TOS tests. This could have created backchanneling in the reactor tube, where the flow of reactants does not pass through the catalyst active sites, thereby lowering the observed rates of consumption for CH_4 and CO_2. Nevertheless, the results of the long TOS tests are valuable to compare the performance of both variants of the CP catalyst when exposed to extended TOS in DRM.

As time progresses, the consumption rate of CH_4 displayed by the monometallic CP catalyst starts to decline until it reaches a value of approximately 0.0305mol/min/gNi slowly. This means that within 70 hours, the monometallic CP catalyst underwent a 16.43% reduction in its rate of consumption of CH_4. As for the bimetallic CP catalyst, its rate of consumption of CH_4 declines at a steeper rate, where it reaches almost 0.0146mol/min/gNi within 70 hours TOS. Thus, the

bimetallic CP catalyst experienced a 46.9% reduction in its rate of consumption of CH_4. Compared to the monometallic CP catalyst, this is almost three times the loss in the rate of CH_4 consumption.

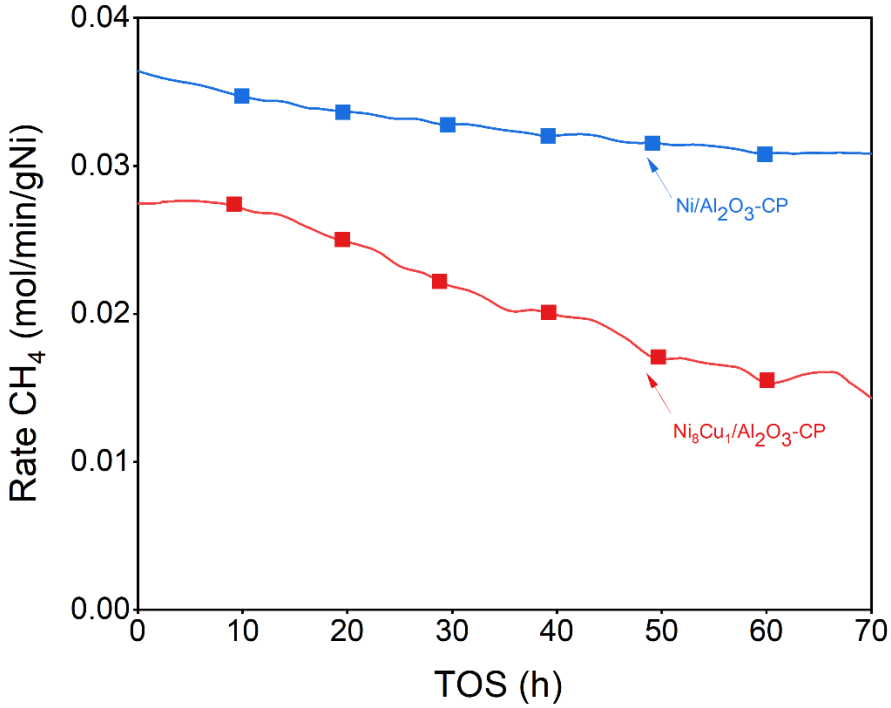

Figure 45: Methane consumption rates for long-time on-stream DRM studies at 650 °C and CH_4: CO_2 = 1:1

The rates of consumption of CO_2 for both CP catalysts are summarized in Figure 46. The monometallic catalyst presents an initial rate of CO_2 consumption of about 0.0427mol/min/g_{Ni}. On the other hand, the bimetallic catalyst shows a lower initial rate of consumption of CO_2 of about 0.0361mol/min/g_{Ni}. The monometallic catalyst's rate maintains a somewhat stable profile, slightly declining until it reaches about 0.0393mol/min/g_{Ni}. This corresponds to a 7.96% drop in its rate. Focusing on the bimetallic catalyst, it is clear that it experiences a greater decrease in its rate where the value slightly increases, then more rapidly drops to about 0.0233mol/min/g_{Ni}. This corresponds to a drop of approximately 35.45%. The drop exhibited by the metallic catalyst is more than four times that observed in the monometallic catalyst.

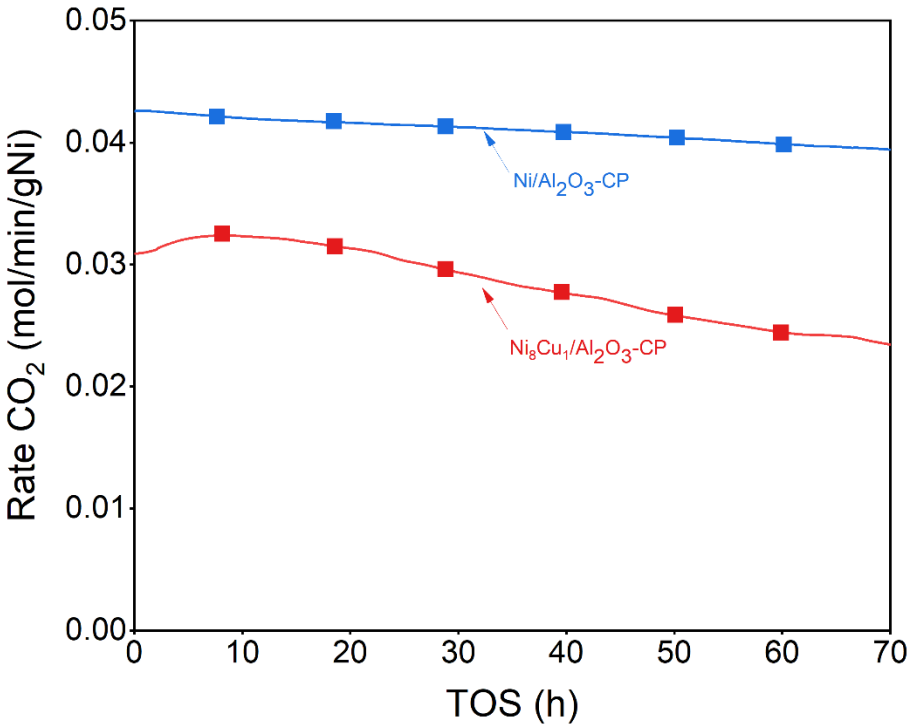

Figure 46: Carbon dioxide consumption rates for long-time on-stream DRM studies at 650 °C and CH_4: CO_2 = 1:1

The H_2/CO ratios throughout 70 hours TOS exhibited by both catalysts are presented in Figure 47. Both catalysts show a somewhat stable ratio. The monometallic catalyst shows an initial ratio of 0.0813. The ratio fluctuates slightly around this value and maintains it till the end of 70 hours. As for the bimetallic catalyst, its initial ratio was 0.0680. Similar to the monometallic catalyst, the ratio fluctuates slightly around this value until the end of 70 hours TOS.

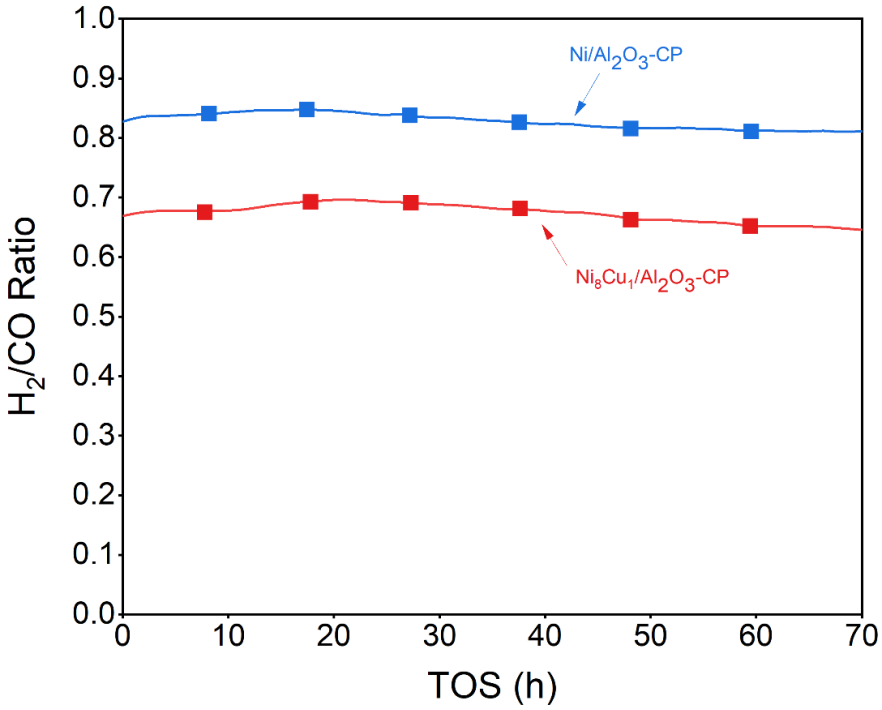

Figure 47: H_2/CO ratio for long time on stream DRM studies at 650 °C and CH_4: CO_2 = 1:1

From the presented activity data, it is clear that the monometallic catalyst outperforms its bimetallic counterpart. As seen in the short TOS tests, the monometallic catalyst offers higher rates for both CH_4 and CO_2 consumption, as well as H_2/CO ratio. However, the long TOS tests showed that the monometallic catalyst presents an advantage in stability as well. This result is interesting and requires further characterization to identify the source of the drop in activity.

4.2.10. Characterization of used long-time-on-stream catalysts

4.2.10.1. X-ray diffraction of used long-time-on-stream catalysts

The XRD results of both spent CP catalysts are presented in Figure 48. In addition to the expected peaks, an extra peak at around $2\theta = 26.6°$ was observed in both used catalysts. This peak corresponds to graphitic carbon [42]. Furthermore, the intensity of this peak in both graphs is somewhat similar, indicating that both catalysts experienced a similar extent of coking. The peak at 44.4°, which corresponds to both metallic nickel and Ni-Cu alloy, is more intense and sharp when compared with the peak observed in the reduced forms of these catalysts. This is indicative of sintering effects as particles grow and become more crystalline. In addition, this signifies that the Ni-Cu alloy structure is not stable in this catalyst. The particle sizes calculated using Scherrer's equation are not presented as the results are erroneous and could be due to the dependence of this equation on the selected particle shape reflected in the K factor. The increase in signal intensity could also be due to copper segregation on the surface of the catalyst.

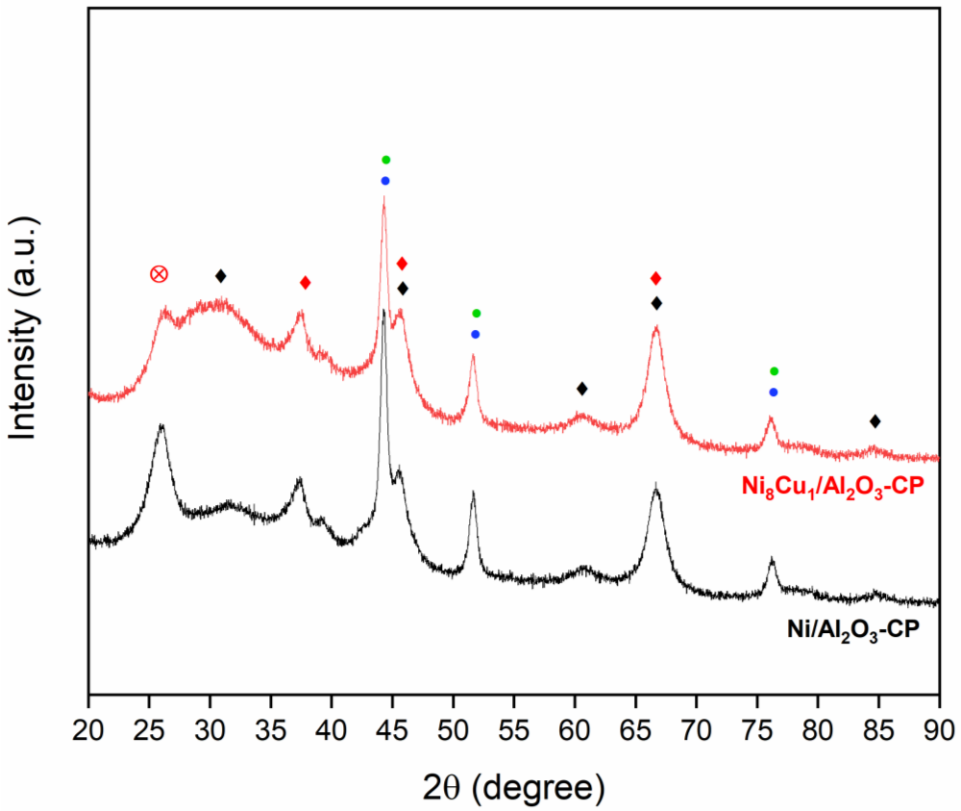

Figure 48: PXRD patterns of used long TOS CP catalysts (♦: γ-Al_2O_3, ♦: $NiAl_2O_4$, •: Ni^0, •: Ni-Cu alloy, (×): Graphitic C)

4.2.10.2. Scanning electron microscopy of used long time on stream catalysts

The SEM images of the spent long TOS monometallic CP catalyst are presented in Figure 49. It is clear that the catalyst has been heavily coked. Carbon nanotubes have formed and densely wrapped the catalyst particles. This is an interesting observation, as the short TOS tests did not show that the monometallic CP catalyst showed a heavy formation of carbon nanotubes. The longer time on stream allowed for coking to occur and the carbon layers to build up. This heavy formation of carbon is probably responsible for the drop in this catalyst's activity, a phenomenon that was not observed in the short TOS tests.

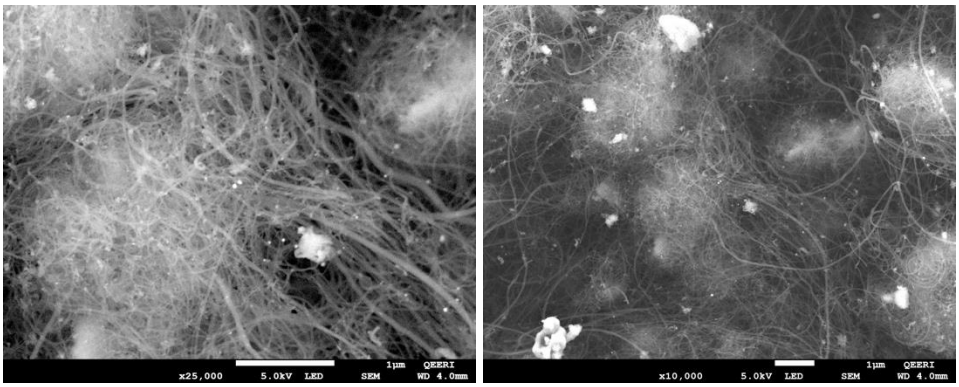

Figure 49: SEM images of used long TOS Ni/Al_2O_3 CP Catalyst

The SEM images of the spent bimetallic long TOS catalyst are presented in Figure 50. The images show that carbon nanotubes have formed. However, compared to the monometallic catalyst, they are far less dense. There are fewer tubes, and their diameter is much smaller when compared with those formed in the monometallic catalyst. The presence of copper in high amounts on the active sites is suspected to have lowered the formation of carbon. The lower reaction rates presented by the bimetallic catalyst decrease the amount of carbon-forming reactions. The fact that the monometallic CP catalyst displayed a higher reaction rate, although it was more heavily coked, indicates that the primary reason for the deactivation of this catalyst might be copper segregation on the surface. The more copper segregation occurs, the less active sites are accessible to reactants. This ends up decreasing the reaction rate and lowers the activity of the catalyst. A more detailed study of the spent catalyst using TEM was employed to investigate the catalyst particles and confirm the theory as mentioned earlier.

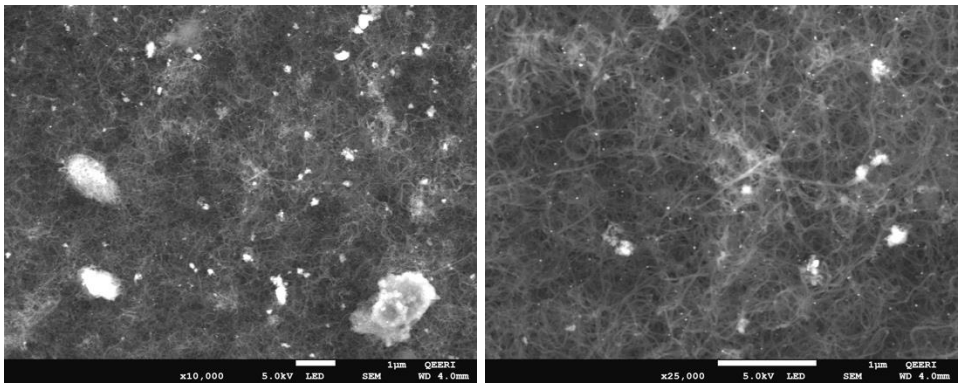

Figure 50: SEM images of used long TOS Ni_8Cu_1/Al_2O_3 CP catalyst

4.2.10.3. Transmission electron microscopy of used long time on stream catalysts

The TEM images, EDS mapping, and the PSD results of the monometallic CP long TOS spent catalyst are presented in Figure 51. Figure 51(a-c) clearly shows nanotubes that have formed around the catalyst particles. Catalyst particles which are embedded within these tubes are also visible. The EDS mapping of a catalyst particle is shown in Figure 51(d). The formed nanotubes were found to be made up of carbon, as expected. The PSD results are presented in Figure 51(f). As can be seen, the mean particle size was 11.56 nm, which is slightly larger than the value observed in the short TOS spent monometallic CP catalyst. Furthermore, the median particle size was 10.03 nm, which is larger than the value observed in the short TOS spent catalyst.

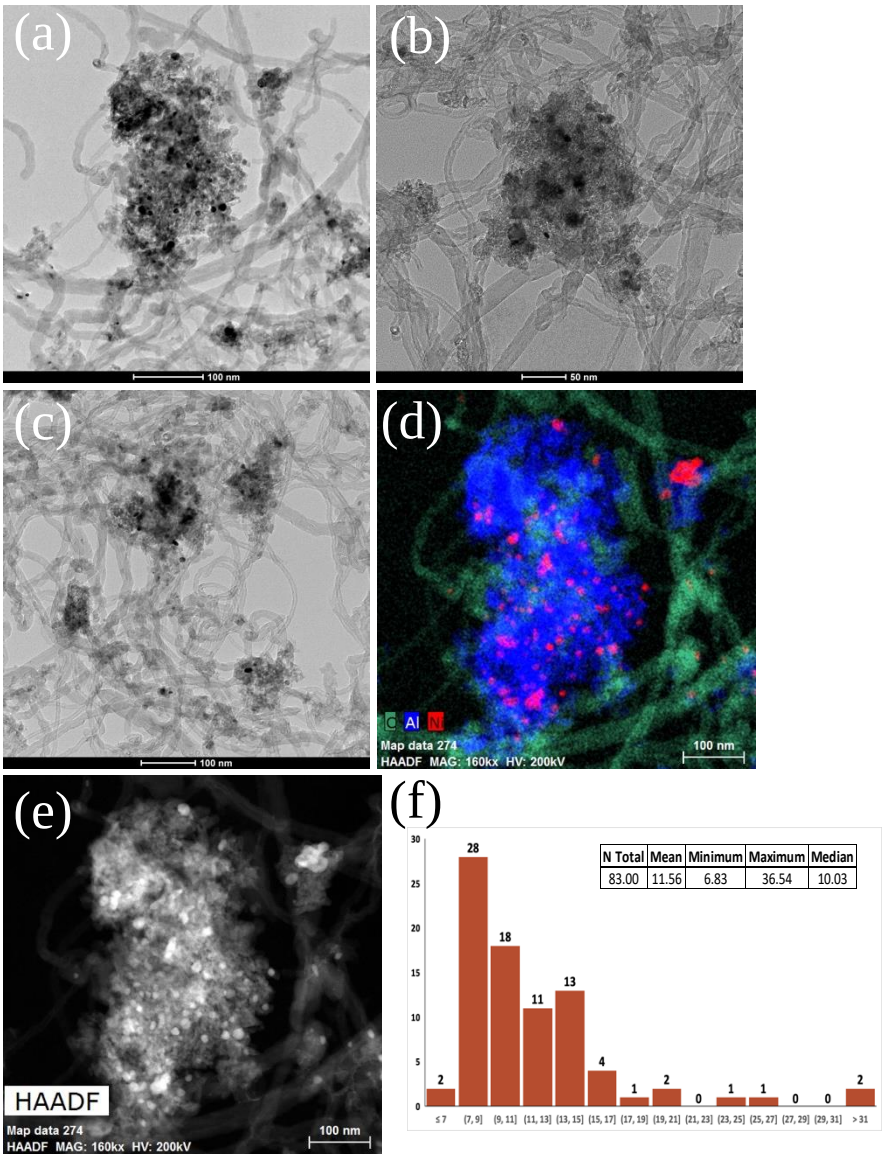

Figure 51: TEM images of used long TOS Ni/Al_2O_3 CP Catalyst

To further study the spent monometallic catalyst, HR-TEM was conducted on specific nickel particles, the results of which are presented in Figure 52. Several nickel particles have been completely encapsulated in layers of graphitic carbon forming onion shapes. The layers of graphitic carbon form on top of each other and take the shape of the encapsulated particle, as shown in Figure 52(d). Amorphous layers of carbon can also be observed forming around the

active nickel sites. The formed layers of carbon are primarily responsible for the loss of activity of this catalyst as access to active sites is blocked. As seen in the SEM images of this spent catalyst, carbon nanotubes have grown significantly and have wrapped the catalyst particles. The HR-TEM images have shown that graphitic carbon layers are more structured, allowing for carbon to grow underneath the nickel particles and form the observed nanotubes. This explains the loss of catalytic activity in the long TOS tests, as opposed to the more stable performance of this catalyst in short TOS DRM, where layers of carbon formed were not as structured.

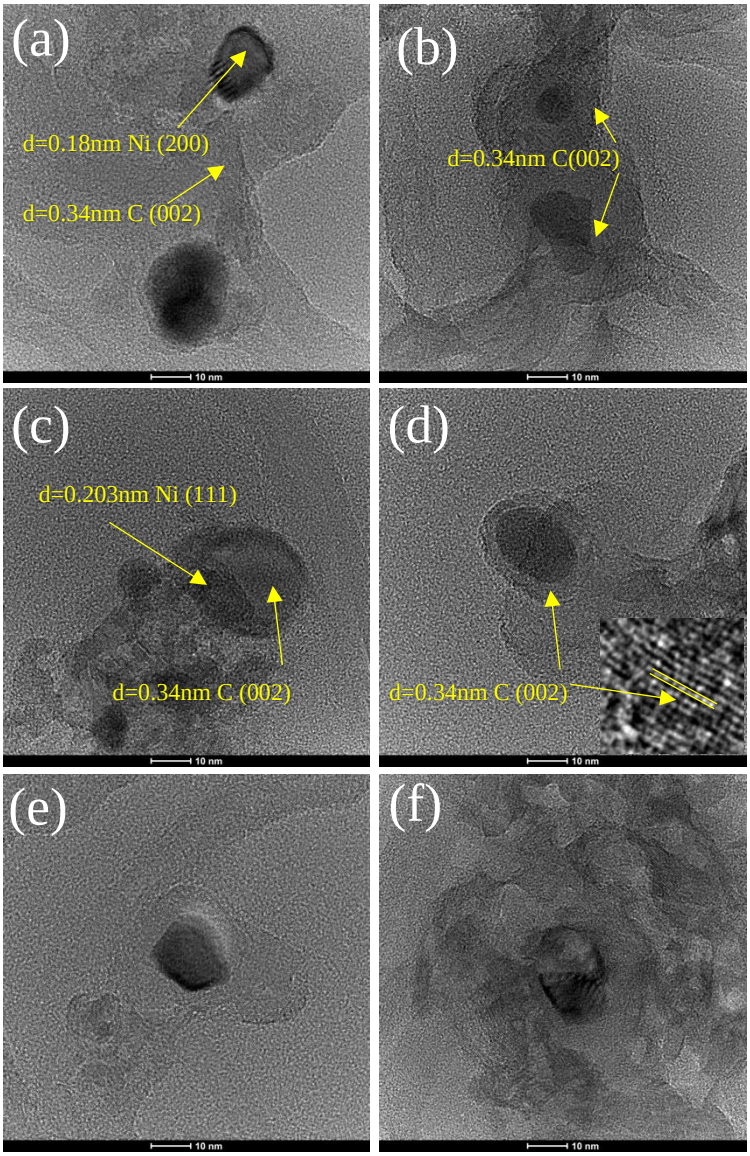

Figure 52: HR-TEM images of used long TOS Ni/Al_2O_3 CP Catalyst

Moving on to the bimetallic long TOS spent catalyst, the TEM images, EDS mapping, and PSD results are presented in Figure 53. The images presented in Figure 53(a-c) show the formation of nanotubes around the catalyst particles. Dense areas of active sites can be observed in Figure 53(a), potentially due to sintering effects. The EDS mapping presented in Figure 53(d) shows that the nanotubes formed are made of carbon, as expected. It can be seen that copper

surrounds the active nickel sites and encapsulates them. This creates a locally high concentration of inactive copper and blocks the access of reactants to the nickel sites. This, in return, lowers the observed rates of consumption of reactants, and activity continues to drop with increasing copper segregation and carbon formation. This explains why the bimetallic catalyst exhibited lower rates and lower stability when compared with the monometallic catalyst. The PSD results are summarized in Figure 53(f) to study the effect of sintering on the bimetallic catalyst. It was found that the mean particle size in the bimetallic spent catalyst was 13.38 nm, which means the average particle size grew by more than 2 nm with respect to its reduced variant. This leads to the conclusion that the bimetallic catalyst is more prone to sintering than the monometallic catalyst since it experienced greater particle growth. This conclusion is supported further when examining the median particle size, which stood at 12.22 nm. This is the highest mean particle size observed thus far. In addition, particles as large as 56.75 nm were observed.

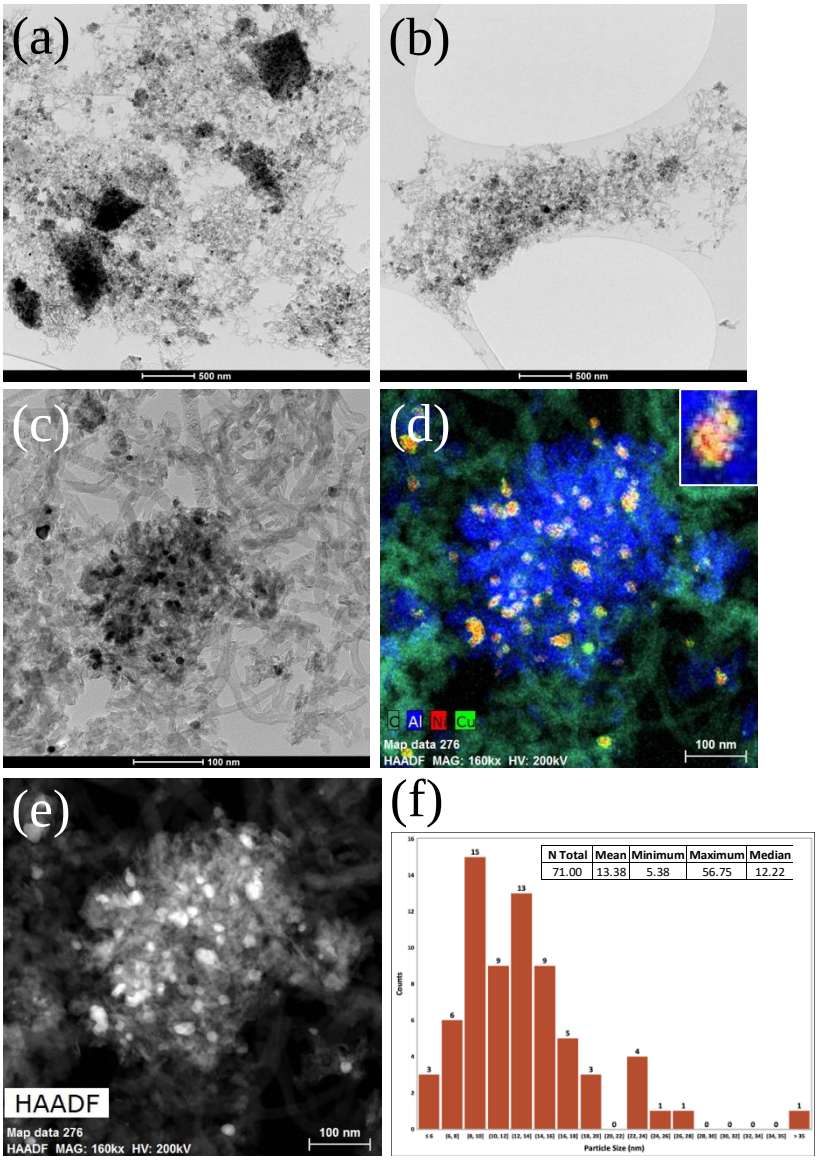

Figure 53: TEM images of used long TOS Ni_8Cu_1/Al_2O_3 CP catalyst

To further study the spent bimetallic catalyst, HR-TEM was conducted, and the results are summarized in Figure 54. Similar to what was observed in the monometallic catalyst, layers of both amorphous and graphitic carbon wrapped the active nickel sites, thereby blocking the access of reactants. Different manners of carbon encapsulation were observed, as onion-shaped carbon particles were formed, as well as nanotube structures. Figure 54(b) shows a fishbone-like carbon

structure with a nickel particle at its top. This results in forming carbon nanotubes that stem from underneath the nickel particle and grow until the nanotube structure is formed. This shows that the introduction of copper in these catalysts did not result in the desired coking resistance. The main reason behind this phenomenon is the locally high concentration of copper on the surface.

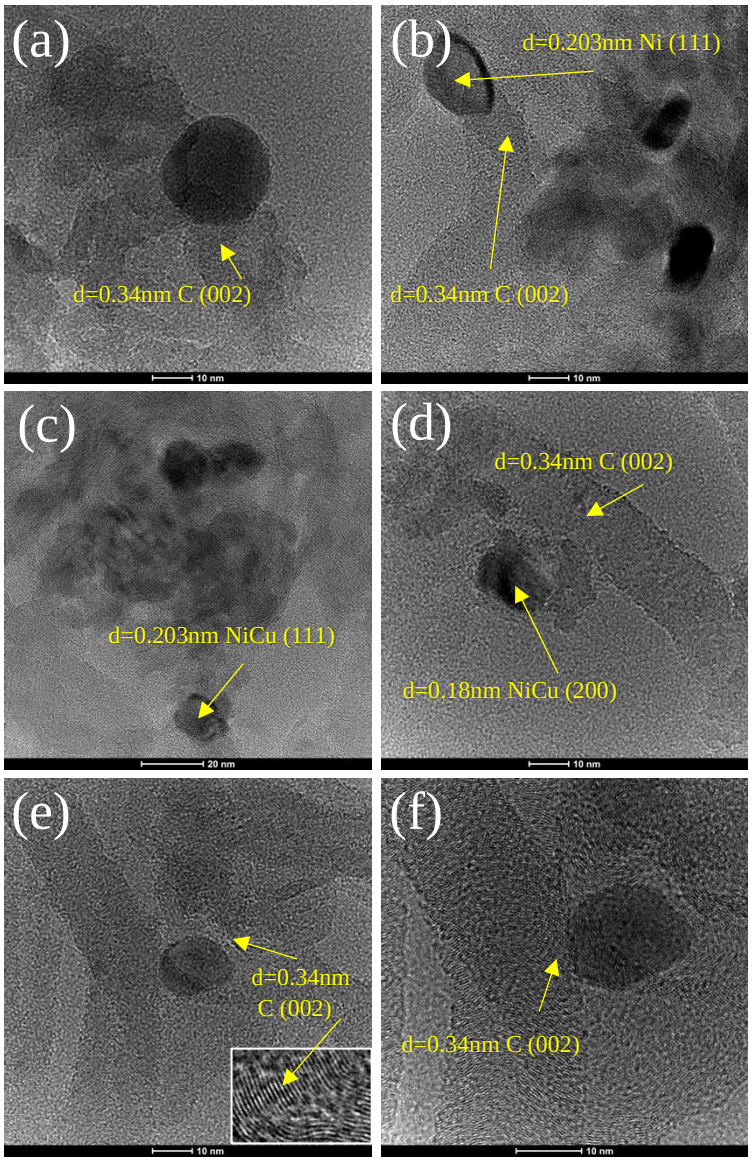

Figure 54: HR-TEM images of used long TOS Ni_8Cu_1/Al_2O_3 CP Catalyst

4.2.10.4. Thermogravimetric Analysis and Differential Scanning Calorimetry of Used Long Time on Stream Catalysts

The thermogravimetric curves of the used catalysts are shown in Figure ***55***. The curve clearly shows that the monometallic catalyst experienced a higher weight drop (29.74%) than the bimetallic catalyst (20.56%). The majority of the weight drop occurs in the region where carbon oxidizes. This indicates that the amount of carbon formed in the monometallic catalyst is higher than that formed in the bimetallic catalyst. This data supports the spent catalyst's SEM results, which showed that the monometallic catalyst had a denser formation of carbon nanotubes. Furthermore, this supports the aforementioned hypothesis that the higher drop in catalytic activity observed in the bimetallic catalyst was due to copper segregation on the catalyst surface rather than coke formation.

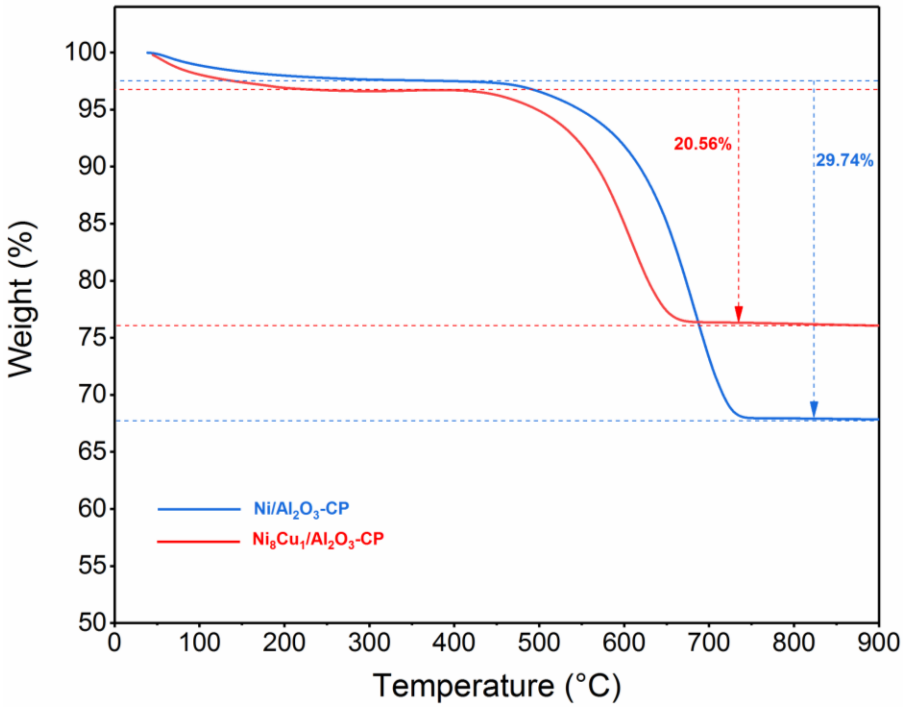

Figure 55: Thermogravimetric graphs of used long TOS CP catalysts

Furthermore, the DSC signals upon heating for each of the spent CP catalysts are presented in Figure ***56***. As can be seen, both signals have a similar trend where two main peaks are

observed, indicating that at least two types of carbon are present. The monometallic CP spent catalyst presented peaks at 451°C and 596°C. On the other hand, the bimetallic CP spent catalyst presented two peaks shifted to lower temperatures of 421°C and 547°C. The first peak in each DSC signal agrees well with encapsulating carbon which wraps the active sites [57]. The stronger second peak exotherm at each peak corresponds to an intermediate position between encapsulating and whisker/graphitic carbon [57]. The fact that the peaks in the bimetallic CP spent catalyst are shifted to lower temperatures could signify that the carbon species formed have lower interaction strengths. These species are more readily removed by oxidation, indicating that the monometallic CP spent catalyst had more severe coke formation.

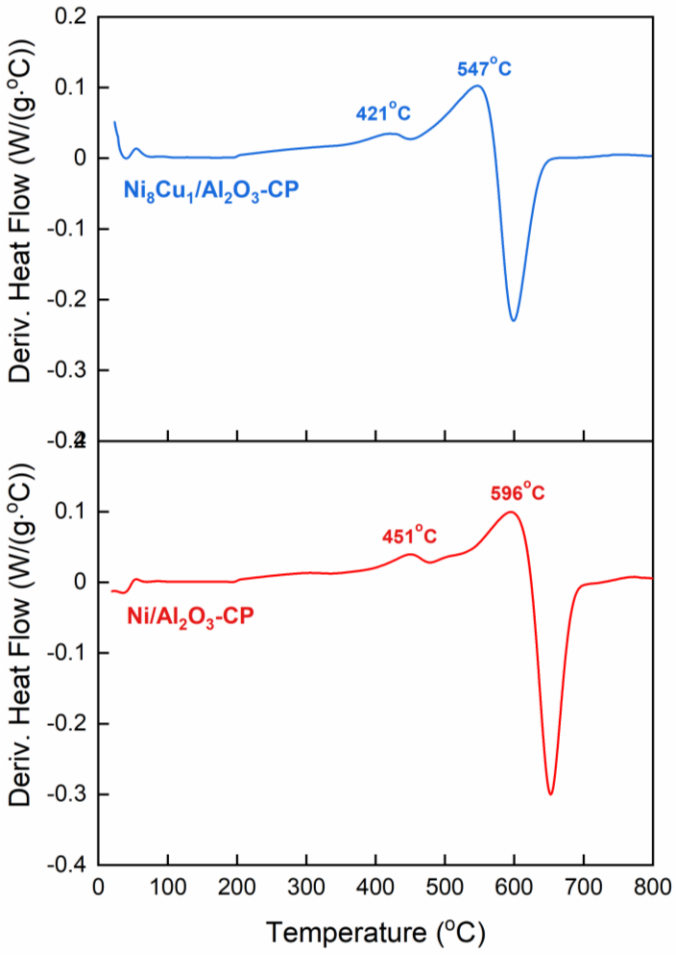

Figure 56: Differential scanning calorimetry graphs of used long TOS CP catalysts

5. CONCLUSIONS AND FUTURE WORK

5.1. Conclusions

In this thesis, we have studied and optimized the impact of Cu promoter on the Ni-Cu/Al_2O_3 prepared by IWI. Furthermore, we have investigated the impact of the synthesis technique on catalyst performance using the SG and CP techniques. First, concerning the Ni-Cu/Al_2O_3 systems prepared by the incipient wetness impregnation method, the amount of Cu introduced into the system dramatically impacts the catalytic performance. The addition of an appropriate amount of Cu into the Ni-Cu bimetallic catalyst affords significantly improved the rates of reactant conversion and stability by more than 50% compared to their monometallic Ni/Al_2O_3 counterpart. Additionally, the 'medium' Cu bimetallic catalyst yields a stable H_2/CO ratio even when the activity begins to decline, while the ratio decreased rapidly for the monometallic catalyst. Catalyst characterization by TPR reveals that Cu increases the reducibility of Ni. At the same time, XRD and TEM validate the formation of smaller bi-metallic crystallites and the formation of a Ni-Cu alloy. CO chemisorption indicates lower dispersion for the bimetallic catalysts, attributed to Cu's inhibitory effect on CO adsorption. TEM results, on the other hand, show a greater dispersion for the bimetallic catalyst. XRD, TPO, SEM, and TGA-DSC analysis of used catalysts confirm that the monometallic Ni deactivated rapidly primarily due to a large amount of graphitic carbon formation. In contrast, the 'medium' Cu-loaded Ni_8Cu_1 catalyst produced a more amorphous or 'active' form of carbon, with minimal graphitic carbon formation. The experimental analysis presented indicates that the percentage of Cu present is critical for 'optimal' performance for DRM. The Cu content must be high enough to allow alloying with Ni but not elevated to a point where excess Cu segregates and forms independent clusters on the

catalyst's surface. These findings are in good agreement with DFT investigations conducted by our group [1].

Second, the outcome of this work confirmed the importance of the synthesis technique on the catalytic performance for nickel-based systems in DRM. the second section of this study compared monometallic Ni/Al_2O_3 systems to the Ni_8Cu_1/Al_2O_3 systems using two different preparation techniques for these catalysts: sol-gel and co-precipitation. The 'medium' loading of copper was chosen to replicate the best performing bimetallic catalyst synthesized by the incipient wetness impregnation (IWI) technique. Contrary to what was expected, the bimetallic catalysts synthesized by sol-gel and co-precipitation were outperformed by their monometallic counterparts in terms of rates of reactant consumption and stability. The monometallic catalysts presented higher and more stable rates of consumption of reactants and H2/CO ratio than the bimetallic catalysts. TEM and EDS mapping of spent short TOS catalysts showed that the active nickel sites in the bimetallic catalysts were covered with a high concentration of copper. This high concentration of copper on the active sites resulted in blocked access of reactants to the nickel particles as confirmed by EDS mapping results, thereby lowering the consumption rates and the resulting H_2/CO ratio. The superior performance of the monometallic CP catalyst was further presented through long TOS DRM tests. The bimetallic catalyst presented lower rates and significantly lower stability when compared to its monometallic counterpart. TEM and SEM analysis of used catalysts showed that both catalysts experienced the formation of amorphous, graphitic carbon, and carbon nanotubes. However, TGA-DSC analysis showed that the monometallic catalyst had a higher amount of carbon formation. EDS mapping confirmed that the high concentration of encapsulating Cu was present on active nickel sites. This ultimately led to

the conclusion that copper segregation on the catalyst surface was the sole reason behind the loss of catalyst stability.

The incipient wetness impregnation technique yielded a bimetallic catalyst that outperformed sol-gel and co-precipitation variants using the exact amounts for nickel and copper in the synthesis procedure. The key performance indicators where the IWI catalyst excelled were rates of reactant consumption, stability in long TOS DRM tests, and coke resistance. The reason behind the superior performance of the IWI bimetallic catalyst was the different chemistry involved in each of these methods. The IWI technique yielded better dispersion of Cu as observed by EDS analysis. On the other hand, SG and CP techniques deposited the same Cu loading in high concentrations on the active nickel sites. This novel work presents a significant contribution to the available literature. There is an evident scarcity of work investigating the impact of preparation technique on bimetallic catalyst system performance. No other study highlights the impact of synthesis technique on the performance of Ni-Cu/Al_2O_3 systems in DRM.

This study also opens the way for future work to be conducted. The sol-gel and coprecipitation techniques are extremely versatile methods that can be tailored according to the design needs of the preparer. The presented results do not necessarily suggest that the incipient wetness impregnation method is better than the sol-gel and coprecipitation techniques for preparing bimetallic catalysts. The use of different solvents and varying promotor amounts could result in very different catalytic performances depending on the nature of the synthesized catalyst. Indeed, catalyst preparation is a fascinating field that combines scientific reasoning and the artistry of the preparer.

5.2. Future work

Although the SG and CP techniques encapsulated active Ni sites with high concentrations of Cu, it does not necessarily mean that these techniques are unfavorable for synthesizing bimetallic catalysts. In fact, these techniques are extremely versatile, and their products can significantly vary when using different solvents. Therefore, additional research can be conducted to study the effect of solvent on catalysts produced using these synthesis techniques.

Furthermore, the deposition of the promoter in high concentrations on active sites in these techniques could be advantageous. Our initial hypothesis is that SG and CP selectively deposit the promoter on active sites. Therefore, it is plausible to assume that using a lower promoter loading in these techniques can result in the same deposition observed in IWI catalysts. To investigate this hypothesis and extend the study, the following campaigns are suggested.

- Repeat the experimental activities of the second campaign of this study with a lower promoter loading.
- Investigate the impact of solvent on the sol-gel and co-precipitation catalysts.
- Optimize the total metal loading in bimetallic Ni-Cu/Al_2O_3-IWI catalysts.

REFERENCES

[1] A. Chatla, M.M. Ghouri, O.W. El Hassan, N. Mohamed, A. V Prakash, N.O. Elbashir, An experimental and first principles DFT investigation on the effect of Cu addition to Ni/Al2O3 catalyst for the dry reforming of methane, Appl. Catal. A Gen. 602 (2020) 117699. https://doi.org/https://doi.org/10.1016/j.apcata.2020.117699.

[2] S. Afzal, D. Sengupta, A. Sarkar, M. El-Halwagi, and, N. Elbashir, Optimization Approach to the Reduction of CO2 Emissions for Syngas Production Involving Dry Reforming, ACS Sustain. Chem. Eng. 6 (2018) 7532–7544. https://doi.org/10.1021/acssuschemeng.8b00235.

[3] M.S. Challiwala, H.A. Choudhury, D. Wang, M.M. El-Halwagi, E. Weitz, N.O. Elbashir, A novel CO2 utilization technology for the synergistic co-production of multi-walled carbon nanotubes and syngas, Sci. Rep. 11 (2021) 1417. https://doi.org/10.1038/s41598-021-80986-2.

[4] D. Pakhare, J. Spivey, A review of dry (CO2) reforming of methane over noble metal catalysts, Chem. Soc. Rev. 43 (2014) 7813–7837. https://doi.org/10.1039/C3CS60395D.

[5] K. Tomishige, D. Li, M. Tamura, Y. Nakagawa, Nickel–iron alloy catalysts for reforming of hydrocarbons: preparation, structure, and catalytic properties, Catal. Sci. Technol. 7 (2017) 3952–3979. https://doi.org/10.1039/C7CY01300K.

[6] I.P. Silverwood, N.G. Hamilton, C.J. Laycock, J.Z. Staniforth, R.M. Ormerod, C.D. Frost, S.F. Parker, D. Lennon, Quantification of surface species present on a nickel/alumina methane reforming catalyst, Phys. Chem. Chem. Phys. 12 (2010) 3102–3107. https://doi.org/10.1039/B919977B.

[7] S. Arora, R. Prasad, An overview on dry reforming of methane: strategies to reduce carbonaceous deactivation of catalysts, RSC Adv. 6 (2016) 108668–108688. https://doi.org/10.1039/C6RA20450C.

[8] Frequently Asked Questions (FAQs) - U.S. Energy Information Administration (EIA), (n.d.). https://www.eia.gov/tools/faqs/faq.php?id=52&t=8 (accessed April 19, 2021).

[9] N.O. Elbashir, M.M. El-Halwagi, I.G. Economou, K.R. Hall, Natural Gas Processing from Midstream to Downstream, Wiley, 2018. https://doi.org/10.1002/9781119269618.

[10] TECHNICAL SUPPORT DOCUMENT FOR HYDROGEN PRODUCTION: PROPOSED RULE FOR MANDATORY REPORTING OF GREENHOUSE GASES, 2008. http://www1.eere.energy.gov/hydrogenandfuelcells/pdfs/30535i.pdf, (accessed April 19, 2021).

[11] J.R. Rostrup-Nielsen, CATALYTIC STEAM REFORMING., Catal. Sci. Technol. 5 (1984) 1–117. https://doi.org/10.1007/978-3-642-93247-2_1.

[12] D. Harshini, Y. Kwon, J. Han, S.P. Yoon, S.W. Nam, T.-H. Lim, Suppression of carbon formation in steam reforming of methane by addition of Co into Ni/ZrO2 catalysts, Korean J. Chem. Eng. 27 (2010) 480–486. https://doi.org/10.1007/s11814-010-0095-9.

[13] A.M. Gadalla, B. Bower, The role of catalyst support on the activity of nickel for reforming methane with CO2, Chem. Eng. Sci. 43 (1988) 3049–3062. https://doi.org/10.1016/0009-2509(88)80058-7.

[14] A.H. Elbadawi, L. Ge, Z. Li, S. Liu, S. Wang, Z. Zhu, Catalytic partial oxidation of methane to syngas: review of perovskite catalysts and membrane reactors, Catal. Rev. - Sci. Eng. 63 (2021) 1–67. https://doi.org/10.1080/01614940.2020.1743420.

[15] J. Lang, Experimentelle Beiträge zur Kenntnis der Vorgänge bei der Wasser- und Heizgasbereitung, Zeitschrift Für Phys. Chemie. 2U (1888) 161–183. https://doi.org/doi:10.1515/zpch-1888-0226.

[16] F. Fisher, H. Tropsch, Conversion of methane into hydrogen and carbon monoxide, Brennst.-Chem. 9 (1928). https://www.osti.gov/biblio/5059290.

[17] M.M.B. Noureldin, N.O. Elbashir, M.M. El-Halwagi, Optimization and selection of reforming approaches for syngas generation from natural/shale gas, Ind. Eng. Chem. Res. 53 (2014) 1841–1855. https://doi.org/10.1021/ie402382w.

[18] Y. Pan, X. Shen, L. Yao, A. Bentalib, Z. Peng, Active Sites in Heterogeneous Catalytic Reaction on Metal and Metal Oxide: Theory and Practice, Catalysts. 8 (2018) 478. https://doi.org/10.3390/catal8100478.

[19] H.Y. Wang, E. Ruckenstein, Carbon dioxide reforming of methane to synthesis gas over supported rhodium catalysts: The effect of support, Appl. Catal. A Gen. 204 (2000) 143–152. https://doi.org/10.1016/S0926-860X(00)00547-0.

[20] A.I. Tsyganok, M. Inaba, T. Tsunoda, S. Hamakawa, K. Suzuki, T. Hayakawa, Dry reforming of methane over supported noble metals: A novel approach to preparing catalysts, Catal. Commun. 4 (2003) 493–498. https://doi.org/10.1016/S1566-7367(03)00130-4.

[21] M. García-Diéguez, I.S. Pieta, M.C. Herrera, M.A. Larrubia, I. Malpartida, L.J. Alemany, Transient study of

the dry reforming of methane over Pt supported on different γ-Al2O3, Catal. Today. 149 (2010) 380–387. https://doi.org/10.1016/j.cattod.2009.07.099.
[22] S. Dekkar, S. Tezkratt, D. Sellam, K. Ikkour, K. Parkhomenko, A. Martinez-Martin, A.C. Roger, Dry Reforming of Methane over Ni–Al2O3 and Ni–SiO2 Catalysts: Role of Preparation Methods, Catal. Letters. 150 (2020) 2180–2199. https://doi.org/10.1007/s10562-020-03120-3.
[23] Z. Hao, Q. Zhu, Z. Jiang, B. Hou, H. Li, Characterization of aerogel Ni/Al2O3 catalysts and investigation on their stability for CH4-CO2 reforming in a fluidized bed, Fuel Process. Technol. 90 (2009) 113–121. https://doi.org/10.1016/j.fuproc.2008.08.004.
[24] Z. Li, K. Sibudjing, Facile Synthesis of Multi-Ni-Core@Ni Phyllosilicate@CeO $_2$ Shell Hollow Spheres with High Oxygen Vacancy Concentration for Dry Reforming of CH $_4$, ChemCatChem. 10 (2018) 2994–3001. https://doi.org/10.1002/cctc.201800335.
[25] S. Corthals, J. Van Nederkassel, J. Geboers, H. De Winne, J. Van Noyen, B. Moens, B. Sels, P. Jacobs, Influence of composition of MgAl2O4 supported NiCeO2ZrO2 catalysts on coke formation and catalyst stability for dry reforming of methane, Catal. Today. 138 (2008) 28–32. https://doi.org/10.1016/j.cattod.2008.04.038.
[26] N. Rahemi, M. Haghighi, A.A. Babaluo, S. Allahyari, M.F. Jafari, Syngas production from reforming of greenhouse gases CH4/CO 2 over Ni-Cu/Al2O3 nanocatalyst: Impregnated vs. plasma-treated catalyst, Energy Convers. Manag. 84 (2014) 50–59. https://doi.org/10.1016/j.enconman.2014.04.016.
[27] T. Wu, Q. Zhang, W. Cai, P. Zhang, X. Song, Z. Sun, L. Gao, Phyllosilicate evolved hierarchical Ni- and Cu-Ni/SiO2 nanocomposites for methane dry reforming catalysis, Appl. Catal. A Gen. 503 (2015) 94–102. https://doi.org/10.1016/j.apcata.2015.07.012.
[28] K. Sutthiumporn, T. Maneerung, Y. Kathiraser, S. Kawi, CO2 dry-reforming of methane over La0.8Sr 0.2Ni0.8M0.2O3 perovskite (M = Bi, Co, Cr, Cu, Fe): Roles of lattice oxygen on C-H activation and carbon suppression, Int. J. Hydrogen Energy. 37 (2012) 11195–11207. https://doi.org/10.1016/j.ijhydene.2012.04.059.
[29] J. Regalbuto, ed., Catalyst Preparation Science and Engineering, 1st ed., CRC Press, 2006. https://doi.org/10.1201/9781420006506.
[30] J.R.H. Ross, Catalyst Preparation, in: Heterog. Catal., Elsevier, 2012: pp. 65–96. https://doi.org/10.1016/b978-0-444-53363-0.10004-0.
[31] C. Perego, P. Villa, Catalyst preparation methods, Catal. Today. 34 (1997) 281–305. https://doi.org/10.1016/S0920-5861(96)00055-7.
[32] S. Sakka, History of the sol-gel chemistry and technology, in: Handb. Sol-Gel Sci. Technol. Process. Charact. Appl., Springer International Publishing, 2018: pp. 3–29. https://doi.org/10.1007/978-3-319-32101-1_87.
[33] U. Schubert, Chemistry and Fundamentals of the Sol-Gel Process, in: Sol-Gel Handb., Wiley-VCH Verlag GmbH & Co. KGaA, Weinheim, Germany, 2015: pp. 1–28. https://doi.org/10.1002/9783527670819.ch01.
[34] A.E. Danks, S.R. Hall, Z. Schnepp, The evolution of 'sol–gel' chemistry as a technique for materials synthesis, Mater. Horiz. 3 (2016) 91–112. https://doi.org/10.1039/C5MH00260E.
[35] S. Esposito, "Traditional" Sol-Gel Chemistry as a Powerful Tool for the Preparation of Supported Metal and Metal Oxide Catalysts., Mater. (Basel, Switzerland). 12 (2019). https://doi.org/10.3390/ma12040668.
[36] P. Munnik, P.E. de Jongh, K.P. de Jong, Recent Developments in the Synthesis of Supported Catalysts, Chem. Rev. 115 (2015) 6687–6718. https://doi.org/10.1021/cr500486u.
[37] B. Ingham, M.F. Toney, 1 - X-ray diffraction for characterizing metallic films, in: K. Barmak, K.B.T.-M.F. for E. Coffey Optical and Magnetic Applications (Eds.), Woodhead Publishing, 2014: pp. 3–38. https://doi.org/https://doi.org/10.1533/9780857096296.1.3.
[38] M. Khzouz, E.I. Gkanas, S. Du, J. Wood, Catalytic performance of Ni-Cu/Al2O3 for effective syngas production by methanol steam reforming, Fuel. 232 (2018) 672–683. https://doi.org/10.1016/j.fuel.2018.06.025.
[39] A. Cross, J.T. Miller, V. Danghyan, A.S. Mukasyan, E.E. Wolf, Highly active and stable Ni-Cu supported catalysts prepared by combustion synthesis for hydrogen production from ethanol, Appl. Catal. A Gen. 572 (2019) 124–133. https://doi.org/https://doi.org/10.1016/j.apcata.2018.12.027.
[40] D. Li, M. Lu, K. Aragaki, M. Koike, Y. Nakagawa, K. Tomishige, Characterization and catalytic performance of hydrotalcite-derived Ni-Cu alloy nanoparticles catalysts for steam reforming of 1-methylnaphthalene, Appl. Catal. B Environ. 192 (2016) 171–181. https://doi.org/10.1016/j.apcatb.2016.03.052.
[41] A. Yin, C. Wen, X. Guo, W.-L. Dai, K. Fan, Influence of Ni species on the structural evolution of Cu/SiO2 catalyst for the chemoselective hydrogenation of dimethyl oxalate, J. Catal. 280 (2011) 77–88. https://doi.org/https://doi.org/10.1016/j.jcat.2011.03.006.

[42] N. Bayat, M. Rezaei, F. Meshkani, Methane dissociation to COx-free hydrogen and carbon nanofiber over Ni-Cu/Al2O3 catalysts, Fuel. 195 (2017) 88–96. https://doi.org/https://doi.org/10.1016/j.fuel.2017.01.039.
[43] B.C. Miranda, R.J. Chimentão, J. Szanyi, A.H. Braga, J.B.O. Santos, F. Gispert-Guirado, J. Llorca, F. Medina, Influence of copper on nickel-based catalysts in the conversion of glycerol, Appl. Catal. B Environ. 166–167 (2015) 166–180. https://doi.org/https://doi.org/10.1016/j.apcatb.2014.11.019.
[44] A.R. Naghash, T.H. Etsell, S. Xu, XRD and XPS Study of Cu−Ni Interactions on Reduced Copper−Nickel−Aluminum Oxide Solid Solution Catalysts, Chem. Mater. 18 (2006) 2480–2488. https://doi.org/10.1021/cm051910o.
[45] I.C. Freitas, R.L. Manfro, M.M.V.M. Souza, Hydrogenolysis of glycerol to propylene glycol in continuous system without hydrogen addition over Cu-Ni catalysts, Appl. Catal. B Environ. 220 (2018) 31–41. https://doi.org/https://doi.org/10.1016/j.apcatb.2017.08.030.
[46] I. Gandarias, J. Requies, P.L. Arias, U. Armbruster, A. Martin, Liquid-phase glycerol hydrogenolysis by formic acid over Ni–Cu/Al2O3 catalysts, J. Catal. 290 (2012) 79–89. https://doi.org/https://doi.org/10.1016/j.jcat.2012.03.004.
[47] D. Li, J. Chen, Y. Li, Evidence of composition deviation of metal particles of a Ni–Cu/Al2O3 catalyst during methane decomposition to COx-free hydrogen, Int. J. Hydrogen Energy. 34 (2009) 299–307. https://doi.org/https://doi.org/10.1016/j.ijhydene.2008.09.106.
[48] N. Wang, W. Qian, W. Chu, F. Wei, Crystal-plane effect of nanoscale CeO2 on the catalytic performance of Ni/CeO2 catalysts for methane dry reforming, Catal. Sci. Technol. 6 (2016) 3594–3605. https://doi.org/10.1039/c5cy01790d.
[49] H. Yen, Y. Seo, S. Kaliaguine, F. Kleitz, Role of Metal–Support Interactions, Particle Size, and Metal–Metal Synergy in CuNi Nanocatalysts for H2 Generation, ACS Catal. 5 (2015) 5505–5511. https://doi.org/10.1021/acscatal.5b00869.
[50] L. De Rogatis, T. Montini, B. Lorenzut, P. Fornasiero, NixCuy/Al2O3 based catalysts for hydrogen production, Energy Environ. Sci. 1 (2008) 501–509. https://doi.org/10.1039/b805426f.
[51] H.S. Bengaard, J.K. Nørskov, J. Sehested, B.S. Clausen, L.P. Nielsen, A.M. Molenbroek, J.R. Rostrup-Nielsen, Steam Reforming and Graphite Formation on Ni Catalysts, J. Catal. 209 (2002) 365–384. https://doi.org/https://doi.org/10.1006/jcat.2002.3579.
[52] J.-H. Lee, E.-G. Lee, O.-S. Joo, K.-D. Jung, Stabilization of Ni/Al2O3 catalyst by Cu addition for CO2 reforming of methane, Appl. Catal. A Gen. 269 (2004) 1–6. https://doi.org/https://doi.org/10.1016/j.apcata.2004.01.035.
[53] H.-W. Chen, C.-Y. Wang, C.-H. Yu, L.-T. Tseng, P.-H. Liao, Carbon dioxide reforming of methane reaction catalyzed by stable nickel copper catalysts, Catal. Today. 97 (2004) 173–180. https://doi.org/https://doi.org/10.1016/j.cattod.2004.03.067.
[54] K. Song, M. Lu, S. Xu, C. Chen, Y. Zhan, D. Li, C. Au, L. Jiang, K. Tomishige, Effect of alloy composition on catalytic performance and coke-resistance property of Ni-Cu/Mg(Al)O catalysts for dry reforming of methane, Appl. Catal. B Environ. 239 (2018) 324–333. https://doi.org/https://doi.org/10.1016/j.apcatb.2018.08.023.
[55] Q. Huang, X. Fang, Q. Cheng, Q. Li, X. Xu, L. Xu, W. Liu, Z. Gao, W. Zhou, X. Wang, Synthesis of a Highly Active and Stable Nickel-Embedded Alumina Catalyst for Methane Dry Reforming: On the Confinement Effects of Alumina Shells for Nickel Nanoparticles, ChemCatChem. 9 (2017) 3563–3571. https://doi.org/10.1002/cctc.201700490.
[56] L. Zhou, L. Li, N. Wei, J. Li, J.-M. Basset, Effect of $NiAl_2O_4$ Formation on Ni/Al_2O_3 Stability during Dry Reforming of Methane, ChemCatChem. 7 (2015) 2508–2516. https://doi.org/10.1002/cctc.201500379.
[57] C. Wang, N. Sun, N. Zhao, W. Wei, J. Zhang, T. Zhao, Y. Sun, C. Sun, H. Liu, C.E. Snape, The Properties of Individual Carbon Residuals and Their Influence on The Deactivation of Ni-CaO-ZrO_2 Catalysts in CH_4 Dry Reforming, ChemCatChem. 6 (2014) 640–648. https://doi.org/10.1002/cctc.201300754.
[58] V. Georgakilas, J.A. Perman, J. Tucek, R. Zboril, Broad Family of Carbon Nanoallotropes: Classification, Chemistry, and Applications of Fullerenes, Carbon Dots, Nanotubes, Graphene, Nanodiamonds, and Combined Superstructures, Chem. Rev. 115 (2015) 4744–4822. https://doi.org/10.1021/cr500304f.
[59] Y. Cao, P. Maitarad, M. Gao, T. Taketsugu, H. Li, T. Yan, L. Shi, D. Zhang, Defect-induced efficient dry reforming of methane over two-dimensional Ni/h-boron nitride nanosheet catalysts, Appl. Catal. B Environ. 238 (2018) 51–60. https://doi.org/https://doi.org/10.1016/j.apcatb.2018.07.001.
[60] S.M.M. Nataj, S.M. Alavi, G. Mazloom, Modeling and optimization of methane dry reforming over Ni–Cu/Al2O3 catalyst using Box–Behnken design, J. Energy Chem. 27 (2018) 1475–1488. https://doi.org/https://doi.org/10.1016/j.jechem.2017.10.002.

[61] Q. Zhang, M. Wang, T. Zhang, Y. Wang, X. Tang, P. Ning, A stable Ni/SBA-15 catalyst prepared by the ammonia evaporation method for dry reforming of methane, RSC Adv. 5 (2015) 94016–94024. https://doi.org/10.1039/c5ra18845h.

[62] L. Karam, S. Casale, H. El Zakhem, N. El Hassan, Tuning the properties of nickel nanoparticles inside SBA-15 mesopores for enhanced stability in methane reforming, J. CO2 Util. 17 (2017) 119–124. https://doi.org/https://doi.org/10.1016/j.jcou.2016.12.002.

[63] Y. Zhan, J. Han, Z. Bao, B. Cao, Y. Li, J. Street, F. Yu, Biogas reforming of carbon dioxide to syngas production over Ni-Mg-Al catalysts, Mol. Catal. 436 (2017) 248–258. https://doi.org/https://doi.org/10.1016/j.mcat.2017.04.032.

[64] J.L. Rogers, M.C. Mangarella, A.D. D'Amico, J.R. Gallagher, M.R. Dutzer, E. Stavitski, J.T. Miller, C. Sievers, Differences in the Nature of Active Sites for Methane Dry Reforming and Methane Steam Reforming over Nickel Aluminate Catalysts, ACS Catal. 6 (2016) 5873–5886. https://doi.org/10.1021/acscatal.6b01133.

[65] S.P. Roe, J.O. Hill, J. Liesegang, An x-ray photoelectron spectroscopic study of some nickel(II) tetraaza macrocyclic complexes, Transit. Met. Chem. 10 (1985) 100–106. https://doi.org/10.1007/BF00618459.

[66] N.W. Cheung, P.J. Grunthaner, F.J. Grunthaner, J.W. Mayer, B.M. Ullrich, METAL-SEMICONDUCTOR INTERFACIAL REACTION: Ni/Si SYSTEM., in: J. Vac. Sci. Technol., American Vacuum SocietyAVS, 1980: pp. 917–923. https://doi.org/10.1116/1.570994.

[67] S.O. Grim, L.J. Matienzo, W.E. Swartz, X-Ray Photoelectron Spectroscopy of Some Nickel Dithiolate Complexes, J. Am. Chem. Soc. 94 (1972) 5116–5117. https://doi.org/10.1021/ja00769a073.

[68] S. Kasztelan, J. Grimblot, J.P. Bonnelle, E. Payen, H. Toulhoat, Y. Jacquin, Preparation of Co-Mo-γAl2O3 and Ni-Mo-γAl2O3 catalysts by ph regulation of molybdenum solution. characterization of supported species and hydrogenation activities, Appl. Catal. 7 (1983) 91–112. https://doi.org/10.1016/0166-9834(83)80241-3.

[69] P. Lorenz, J. Finster, G. Wendt, J. V. Salyn, E.K. Žumadilov, V.I. Nefedov, Esca investigations of some NiO/SiO2 and NiO-Al2 O3 /SiO2 catalysts, J. Electron Spectros. Relat. Phenomena. 16 (1979) 267–276. https://doi.org/10.1016/0368-2048(79)80023-7.

[70] L. Salvati, L.E. Makovsky, J.M. Stencel, F.R. Brown, D.M. Hercules, Surface spectroscopic study of tungsten-alumina catalysts using X-ray photoelectron, ion scattering, and Raman spectroscopies, J. Phys. Chem. 85 (1981) 3700–3707. https://doi.org/10.1021/j150624a035.

[71] A.M. Venezia, R. Bertoncello, G. Deganello, X-ray photoelectron spectroscopy investigation of pumice-supported nickel catalysts, Surf. Interface Anal. 23 (1995) 239–247. https://doi.org/10.1002/sia.740230408.

[72] A.F. Carley, M.W. Roberts, X-RAY PHOTOELECTRON SPECTROSCOPIC STUDY OF THE INTERACTION OF OXYGEN AND NITRIC OXIDE WITH ALUMINIUM., Proc R Soc London Ser A. 363 (1978) 403–424. https://doi.org/10.1098/rspa.1978.0175.

[73] A. Serrà, E. Gómez, J. Michler, L. Philippe, Facile cost-effective fabrication of Cu@Cu2O@CuO–microalgae photocatalyst with enhanced visible light degradation of tetracycline, Chem. Eng. J. 413 (2021) 127477. https://doi.org/https://doi.org/10.1016/j.cej.2020.127477.

[74] N. Rajasekaran, S. Mohan, Structure, microstructure and corrosion properties of brush-plated Cu–Ni alloy, J. Appl. Electrochem. 39 (2009) 1911. https://doi.org/10.1007/s10800-009-9899-x.

[75] K. Jabbour, P. Massiani, A. Davidson, S. Casale, N. El Hassan, Ordered mesoporous "one-pot" synthesized Ni-Mg(Ca)-Al2O3 as effective and remarkably stable catalysts for combined steam and dry reforming of methane (CSDRM), Appl. Catal. B Environ. 201 (2017) 527–542. https://doi.org/10.1016/j.apcatb.2016.08.009.

[76] W. Liang, H. Yan, C. Chen, D. Lin, K. Tan, X. Feng, Y. Liu, X. Chen, C. Yang, H. Shan, Revealing the effect of nickel particle size on carbon formation type in the methane decomposition reaction, Catalysts. 10 (2020) 1–20. https://doi.org/10.3390/catal10080890.